SCANNING TUNNELING MICROSCOPY INVESTIGATION OF ATOMICALLY PRECISE GRAPHENE NANORIBBONS

BY

ADRIAN RADOCEA

DISSERTATION

Submitted in partial fulfillment of the requirements
for the degree of Doctor of Philosophy in Materials Science and Engineering
in the Graduate College of the
University of Illinois at Urbana-Champaign, 2017

Urbana, Illinois

Doctoral Committee:

Professor Joseph W. Lyding, Chair
Professor Greg Girolami
Professor Moonsub Shim
Assistant Professor Pinshane Huang
Assistant Professor Andre Schleife

ABSTRACT

This dissertation demonstrates the dry contact transfer of atomically precise graphene nanoribbons onto H:Si(100) under ultra-high vacuum, detailed electronic characterization, and electron-mediated polymerization of graphene nanoribbon precursors into polyanthrylene.

Detailed scanning tunneling microscopy (STM) and scanning tunneling spectroscopy (STS) measurements provided high-resolution imaging and reveal a 2.76 eV bandgap for chevron graphene nanoribbons. It was also discovered that tunneling to the substrate influenced STS measurements. STM and STS studies of two additional GNR geometries, the extended chevron GNR (eGNR) and the hybrid GNR (hGNR) elucidate how structural modification alters the bandgap of GNRs. The increased lateral extension of the eGNR was found to result in a bandgap of 2.66 eV. The hGNR bandgap was found to be 1.8 eV, in agreement with computational modeling.

The hypothesis that positional control over graphene nanoribbon synthesis could be achieved by tip-induced polymerization was explored. While the thermal self-assembly of 10,10-dibromo-9,9-bianthracene (DBBA) into N=7 armchair GNRs was previously demonstrated, the electron-mediated formation of polyanthrylene (GNR intermediate) formation was not previously shown. The STM experiments suggest that when the DBBA is thermally annealed to form a close-packed zigzag structure, an STM tip can be used to drive a de-bromination reaction which is followed by polyanthrylene formation, demonstrating a key step towards positional control over GNR synthesis.

To my parents, for their love and support.

ACKNOWLEDGMENTS

I am extremely grateful for the opportunity to conduct research in the Lyding group. Professor Lyding has provided an immense amount of guidance, diligently training me in the ways of UHV-STM and fostering my development as an individual researcher. His mentoring style teaches his students how to think critically and solve difficult technical challenges on their own however he is always willing to help, and is often seen solving problems around the lab. He also provides his students with incredible professional development opportunities. Prof. Lyding relentlessly promotes his students and their work during his frequent talks. I am especially thankful for the opportunities to attend conferences and funding review meetings across the world. I thank my committee members, Professor Greg Girolami, Professor Moonsub Shim, Assistant Professor Pinshange Huang, and Assistant Professor Andre Schleife for setting aside time out of their busy schedules to serve on my committee. Your thoughtful comments and engaging questions have had a positive impact on my dissertation. I have been fortunate to receive generous support from the National Science Foundation (NSF) through a Graduate Research Fellowship (GRFP), a Hamer Fellowship from the Department of Materials Science and Engineering, and funding from the National Science Foundation (NSF) and the Office of Naval Research (ONR) (grant #N00014-13-1-0300).

My colleagues in the Lyding group have been an extremely valuable resource, constantly providing guidance, research ideas, and creating a very welcoming environment for pursuing challenging research ideas. Dr. Scott Schmucker, Dr. Pamela Martin, Dr. Kevin He, and Dr. Justin Koepke taught me a great deal from operating and baking out a UHV-STM to sample prep, tip etching, and

data analysis. Frequent discussions with Yaofeng Chen have always been enjoyable. Ximeng Liu has been a pleasure to work with. We often worked together on emergency pump repairs, and more recently collaborated on a graphene nanoribbon paper. Dr. Jae Won Do and Dr. Josh Wood have provided tremendous insight into evaluating research directions and carving out a path into the unknown. I have also greatly enjoyed my time both inside and outside the lab with Sartaj Grewal, Torin Kilpatrick, and Siddhanth Munukutla. Sundar Rajarajan, Aniruddh Rangarajan, Junyi Qui, Shengyuang Zhong, and many others also contributed to the productive environment. My colleagues in the Gruebele group - Dr. Lea Nienhaus, Dr. Duc Ngyuen, and Huy Nguyen have been another source of support and stimulating research discussions. To the newest members of the Lyding Group, Kaitlyn Parsons and Faraz Aratsu, I am glad to have worked with you and I look forward to seeing the great work that you will do. I would also like to thank Lyding group alumni Dr. Jinju Lee, and Basil Aruin at TipTek (co-founded by Prof. Lyding) for providing sharpened STM probes that have improved the quality of the STM imaging and STS data.

Much of the work in this thesis addresses interdisciplinary challenges. I have been fortunate to collaborate with many others to tackle some of the difficult challenges facing atomically precise materials. Dr. Peter Sempsrott, and Prof. Girolami synthesized some of the molecules used in my early exploration of bromoaromatic compounds and provided technical insights towards understanding the behavior of DBBA on Au(111). I would like to thank Prof. Aluru and Tao Sun for carrying out computational modeling to better understand the properties of graphene nanoribbons. My frequent discussions with Tao sparked many of the insights on the path towards understanding GNRs. I would also like to thank Prof. Alex Sinitskii at the University of Nebraska and his students Dr. Timothy Vo, Mohammad Mehdi, and Mikhail Shekhirev have graciously shared many of their solution-synthesized graphene nanoribbons for dry contact transfer experiments.

I would like to thank Kelly Young and Mary Jo Anastasia for all their assistance with ordering lab supplies, booking rooms, an organizing travel. Scott Robinson

and Cate Wallace have provided first-class training and support in the operation of the transmission electron microscope and the scanning electron microscope which I frequently used to examine STM probes. Scott A. McDonald and the rest of the staff in the ECE machine shop also played a significant role and helped to provide numerous parts that were required for the modification and repair of the UHV-STM system used to collect most of the STM data.

To my friends and family - having you along for the journey helped immensely. Thank you for the help navigating the steep learning curve of grad school. My twin brother Alex helped with the code I used to read CITS data from STM files (he wrote 95% of it). Kaity Ripple has been a constant source of support always ready to hear my lab stories, and even more ready to lead the charge when it was time to celebrate.

TABLE OF CONTENTS

CHAPTER 1 INTRODUCTION 1
1.1 Background 1
1.2 Scanning Tunneling Microscopy 2
1.3 Graphene Nanoribbons 3
1.4 Graphene Nanoribbon Synthesis 4
1.5 Chemical and Structural Modification of Graphene Nanoribbons . 5
1.6 Placing Graphene Nanoribbons onto Nonmetallic Surfaces 7
1.7 Graphene Nanoribbon Alignment and Positioning 9
1.8 Details on Thermal Self-assembly of Atomically Precise Graphene Nanoribbons 10
1.9 Thesis Statement and Dissertation Structure 12
1.10 Figures 14
1.11 References 15

CHAPTER 2 SOLUTION-SYNTHESIZED CHEVRON GRAPHENE NANORIBBONS EXFOLIATED ONTO H:SI(100) 24
2.1 Introduction 24
2.2 Imaging of Chevron Graphene Nanoribbons on H:Si(100) 26
2.3 Electronic Characterization of Chevron GNRs on H:Si(100) 27
2.4 Junctions Formed by Overlapping Chevron Graphene Nanoribbons 32
2.5 Depassivating H:Si(100) underneath a GNR 33
2.6 Conclusion 34
2.7 Methods 35
2.8 Figures 38
2.9 References 52

CHAPTER 3 EXTENDED CHEVRON AND POROUS GNRS ON H:SI(100) 58
3.1 Motivation and Theoretical Comparisons 58
3.2 Extended Chevron GNRs 60
3.3 Scanning Tunneling Spectroscopy of Extended Chevron GNR . . . 61
3.4 Porous Graphene Nanoribbons 63
3.5 Scanning Tunneling Spectroscopy of Porous GNRs 64
3.6 Figures 67
3.7 References 75

CHAPTER 4 TIP-INDUCED POLYMERIZATION OF POLYANTHRYLENE 78
4.1 Background and Motivation 78
4.2 Experimental Setup 81
4.3 Monolayers of DBBA 81
4.4 Tip-induced polymerization of DBBA 84
4.5 Structure of polyanthrylene islands on Au(111) 87
4.6 Discussion 89
4.7 Conclusion 90
4.8 Figures 91
4.9 References 103

CHAPTER 5 SUMMARY AND FUTURE WORK 108
5.1 Summary 108
5.2 Future Work 110
5.3 References 111

CHAPTER 1

INTRODUCTION

1.1 Background

The International Technology Roadmap for Semiconductors highlights the uncertainty for the sub-7 nm node and beyond because of challenges that arise as transistor components are scaled down to just a few nanometers in length. Intel has already announced that it will no longer use silicon and is exploring alternative materials.[3] Ideal materials are chemically stable, allow for fast switching, minimize leakage current, and can be manufactured with very high uniformity at size scales relevant for the end of the roadmap.[52] 2D materials are poised to overcome scaling limits. For example, the predicted 5 nm gate length limit[25] for conventional materials has been exceeded through the demonstration of a 1 nm effective gate length MoS_2 transistor.[23] Carbon materials such as graphene, carbon nanotubes, and graphene nanoribbons (GNRs) may play an important role due to their small sizes and remarkable properties. GNRs are atomically thin, less than a few nanometers wide, and are of the right size scale to operate at the end of the roadmap. GNRs are particularly promising because they are predicted to achieve charge carrier mobility on the order of 10^3 - 10^5 cm^2/Vs while maintaining bandgaps of 0.3-1.0 eV, allowing them to potentially exceed the performance of current materials.[17] In contrast to most materials, graphene nanoribbons can be synthesized with atomic precision pushing towards the ultimate limits of nanofabrication and electronic devices.

1.2 Scanning Tunneling Microscopy

Scanning tunneling microscopy is uniquely suitable for studying graphene nanoribbons due to its ability to achieve atomic resolution imaging and high spatial resolution electronic measurements. In constant current mode, an atomically sharp metal wire is scanned over a surface, and the tip-sample separation is adjusted to maintain a constant tunneling current. The height adjustments are recorded to produce a topographic image of the surface.[15]

The scanning tunneling microscope can be used to measure the electronic properties of surfaces. When a positive bias is applied to the sample and the tip is grounded, electrons from the filled states of the tip will flow into the empty states of the sample. For negative bias, electrons leave the filled states of the sample and enter the empty states of the tip. The tunneling current, I, is proportional to the overlap between empty and filled states as shown in equation 1.1 below where V is the sample bias E_{F} is the Fermi level, ρ_{S} is the density of states of the sample, ρ_{T} is the density of states of the STM tip, and M is the tunneling matrix that describes the overlap between the wavefunctions of the tip and the sample.[15]

$$I \propto \int_0^{eV} \rho_S(E_F - eV + \epsilon)\rho_T(E_F + \epsilon)|M(\epsilon)|d\epsilon \tag{1.1}$$

$$\frac{dI}{dV} \approx \rho_S(E_F + eV)\rho_T(E_F) \tag{1.2}$$

The tunneling conductance dI/dV can be numerically calculated or measured with a lock-in amplifier. Under the assumption that the tip density of states and the transmission probability remains constant, the tunneling conductance dI/dV is directly proportional to the local density of states of the substrate.

1.3 Graphene Nanoribbons

Theoretically, graphene nanoribbons are expected to have bandgaps inversely proportional to their widths. Qualitatively, this can be understood as removing large scattering vectors in real space which is equivalent to removing the k points close to the Dirac point as shown in Figure 1.1. The electronic structure of graphene nanoribbons also has a strong chirality dependence analogous to the electronic structure of carbon nanotubes.[36, 38] Analytical tight binding models[11, 55] predict that straight armchair graphene nanoribbons of the family $N = 3m + 2$ where N denotes the number of carbon atoms that define the width of the GNR and m is an integer are metallic. Armchair GNRs of the family $N = 3m$ and $N = 3m + 1$ are predicted to be semiconductors. First principles modeling of graphene nanoribbons makes further refinements to the predicted behavior of graphene nanoribbons. Due to a small change in the bond lengths at the edges of GNRs, a small bandgap opens up in armchair GNRs of the family $N = 3m + 2$.[66]

Tight-binding calculations predict that zigzag graphene nanoribbons are semiconducting and magnetic.[66, 67] Recent progress in the fabrication of atomically precise zigzag GNRs has experimentally confirmed their semiconducting behavior.[51, 62, 80] In contrast to carbon nanotubes which have a continuous boundary condition along the lateral direction, graphene nanoribbons have edges that lead to a unique band structure. While a single zigzag edge along part of a graphene sheet has a highly-localized edge state at the Fermi level, for zigzag nanoribbons electron-electron interactions lead to magnetic ordering and energy splitting between the edge states.[66] If no magnetic ordering took place, the two graphene nanoribbon edges would have edge states of equal energy at the Fermi level.[28, 55] Because the density of states at the edge is very high, even a small energetic gain from the alignment of the spins leads to magnetic ordering.[28, 66, 67] Since the opposite edges have atoms that belong to two different sublattices, the two bands split in energy, opening a bandgap in zigzag graphene nanoribbons. Armchair graphene nanoribbons do not have a doubly degenerate localized edge state

near the Fermi level and are not magnetic. The electronic properties of graphene nanoribbons vary strongly with nanoribbon width and chirality and thus, atomic precision is necessary to reach the full potential of graphene nanostructures.

1.4 Graphene Nanoribbon Synthesis

A variety of approaches towards fabricating graphene nanoribbons have emerged, which can be divided into top-down and bottom-up approaches. The top-down methods consist of conventional semiconductor fabrication techniques such as lithographic patterning of a polymer resist followed by chemical etching of an underlying sheet of graphene.[30] Top-down lithography and chemical etching can indeed produce narrow semiconducting nanoribbons. However, the width and band gap vary largely along the GNR length.[46] Poor control over width and chirality is also an issue for graphene nanoribbons grown on narrow strips of copper or nickel.[16, 39] STM-induced etching of graphene nanoribbons provides some control over the crystallographic orientation but edge roughness remains on the order of several atoms.[51, 57, 69] Even with advanced e-beam lithography that uses block copolymer photoresists to achieve sub-10 nm resolution, control over the electronic properties of the nanoribbons is not achieved.[35] The bottom-up approach towards graphene nanoribbon synthesis has included ultracentrifugation of nanoribbons from chemically exfoliated graphite,[45] bottom-up unzipping of carbon nanotubes,[37, 44, 79] and the formation of narrow nanoribbons in-between SiC facets during the formation of free-standing graphene on SiC(1000).[83] While many of these techniques overcome limitations in top-down lithography, there is a lack of atomic-scale control. In 2010 Cai et al. demonstrated the bottom-up self-assembly of atomically precise graphene nanoribbons from halogenated aromatic precursors.[14] At the time there had already been extensive research on the formation of aromatic networks on noble metal surfaces[27, 29, 53, 71] with major efforts focused on strategies towards controlling the ordering of covalent organic networks. Achieving long-range order in two-dimensional networks is dif-

ficult however some early success included the formation of formation of porous phenylene networks.[6] Nanoribbons are made atomically precise using molecular building blocks that link up to form one-dimensional chains. The synthesis was first demonstrated with the molecule 10,10-9'9- dibromo-bianthryl (DBBA) that forms N=7 armchair graphene nanoribbons (7A GNRs) and 6,11-dibromo-1,2,3,4-tetraphenyltriphenylene which forms chevron graphene nanoribbons.[14] The synthesis of 7A GNRs from DBBA is shown in Figure 1.2. The molecules are deposited onto a gold surface and heated at 200 °C to allow C-Br bonds to cleave. The radical species covalently link to form polyanthrylene chains. A second thermal annealing step at 400 °C leads to cyclodehydrogenation, where additional C-C bonds are made and inner H atoms are removed to form hydrogen-terminated graphene nanoribbons.[8]

1.5 Chemical and Structural Modification of Graphene Nanoribbons

Following the synthesis of the N=7 armchair GNR, several groups have experimentally determined that the bandgap of a GNR could be tuned by changing its width. So far N=5,[42] N=7,[14] N=9,[68] N= 13,[20] N=14,[33]and N=15 AGNRs[1] have all been made on noble metal substrates. Interestingly the N=5 armchair GNRs show the predicted metallic behavior expected for the 3p+2 armchair family of GNRs.[42] More recently zigzag edged graphene nanoribbons have been synthesized.[62] Only the N=9 ZGNR has been demonstrated so far, because of the difficulty in finding a precursor that can polymerize along the zigzag direction. It should also be noted that 7A GNRs of finite length have zigzag edges at their ends, which show significant energy splitting indicating the formation of spin-polarized edge states.[80] The electronic properties of the graphene nanoribbons can be further tuned by changing the doping of graphene nanoribbons. Nitrogen,[75, 76] boron,[21, 40] and sulfur[58] have been incorporated into the structure of graphene nanoribbons by substituting the dopant species of interest with carbon atoms in the halogenated aromatic

precursors. Increasing the amount of nitrogen in a graphene nanoribbon makes the material increasingly n-type.[12] In silicon, boron provides acceptor states that increase the hole concentration to create a p-type material. However, B-doped 7-AGNRs that feature two boron atoms per precursor molecule have dopant concentrations as high as 10^{14} cm^{-2}, leading to a mid-gap impurity band that sits above the Fermi level with a density of states comparable to the conduction and valence bands of the pristine 7A GNR.[21] In graphene nanoribbons, dopant atoms can drastically modify the electronic band structure of the graphene nanoribbon.

While the bandgap, and to some extent doping level of graphene nanoribbons[12] can be tuned, the ability to tune the effective mass of a graphene nanoribbon is also desired. The general expectation is that as the width of the graphene nanoribbon increases, the intrinsic behavior of graphene is recovered and the effective mass decreases at the expense of a decreasing bandgap. Decreasing the effective mass while maintaining a large bandgap may be desirable for electronic devices. Changing the geometry of the graphene nanoribbon has been the primary avenue for this pursuit. Examples of geometry modification include combining precursors to make graphene nanoribbon heterojunctions,[19] adding fluoranthene subunits[62] or engineering defects such as 4 or 8 membered rings into graphene nanoribbons.[49] While analytical models capture to first order the behavior of armchair and zigzag graphene nanoribbons, first principle modeling using density functional theory has been able to classify the properties of large classes of chiral nanoribbons that consist of a mixture of armchair and zigzag edges.[60] Following this work, the cove-type graphene nanoribbon has been identified to have a low effective mass while maintaining a high bandgap, making it attractive for GNR transistor applications.[48]

Chevron graphene nanoribbons have 2.8 eV bandgaps, flat bands and a high effective mass.[18, 81] If the structure of a chevron graphene nanoribbon can be modified, perhaps its electronic properties can be enhanced. This thesis will show the electronic characterization of extended chevron graphene nanoribbons to show how increasing the width of the ribbon at only a few sites gently perturbs

the electronic structure. Additionally, hybrid GNRs, which can be visualized as a chevron nanoribbon with additional carbon atoms linking the elbow sites are studied, showing how the electronic structure of chevron nanoribbons can be greatly altered. These new graphene nanoribbons have not been previously characterized. Building a knowledge base of geometry modification is one of the major steps towards better understanding how to tune the properties of GNRs. The graphene nanoribbons mentioned above are shown in Figure 1.3.

1.6 Placing Graphene Nanoribbons onto Nonmetallic Surfaces

While a large variety of graphene nanoribbons have been synthesized, spectroscopic measurements have been limited by interactions between graphene nanoribbons and surface states.[58, 62] For zigzag graphene nanoribbons on Au(111) the edge states are not measurable with scanning tunneling spectroscopy unless the GNR is placed on top of an insulating NaCl layer.[62, 80] Another method for decoupling graphene nanoribbons from the metal substrate is to form a gold silicide underneath the nanoribbons.[22] There are cases where scanning tunneling spectroscopy readily identified peaks in the density of states of a graphene nanoribbon,[19] however, substrate screening modifies the bandgap of the graphene nanoribbons by several tenths of an eV due to strong excitonic effects in confined systems.[41, 56, 70] Graphene nanoribbons on a monolayer of NaCl still show a significant bandgap change demonstrating the importance of placing graphene nanoribbons onto a nonmetallic substrate to recover their intrinsic properties.[41] Transferring nanoribbons onto a substrate such as H:Si(100) facilitates spectroscopic characterization, but may also pave the way towards prototyping GNR transistors. There has been an active effort in demonstrating bottom-up self-assembly of graphene nanoribbon precursors directly on non-metallic substrates. So far the formation of polyanthryelene on Ti(100)[84] and the dimerization of GNR precursors on H:Ge(100) has been shown, but the substrates could not catalyze

a cyclodehydrogenation reaction and nanoribbons were not formed.[59] Narrow armchair nanoribbons can be grown directly onto semiconducting Ge(100) and Ge(111) substrates from methane gas but without atomic level control over GNR width, resulting in bandgap variability.[34] There is a significant need to cleanly transfer nanoribbons onto a semiconducting or insulating surface. Wet transfers methods that involve etching of gold on mica growth substrates leave residue and contamination that degrade device performance.[5] The Lyding group has previously developed an ultra-high vacuum dry contact transfer (DCT) technique that places carbon nanotubes[2] and graphene nanoflakes[61] onto atomically clean semiconducting substrates under ultra-high vacuum. The dry contact transfer process has been used for detailed electronic characterization of graphene nanoribbon edges,[61] providing critical experimental evidence on the role of edge structure. This thesis extends the dry contact transfer process to atomically precise graphene nanoribbons.

A fiberglass applicator is coated in graphene nanoribbon powder, degassed under UHV for 8-16 hours to remove solvent molecules, and then the applicator is pressed against a surface to exfoliate individual nanoribbons onto the sample surface. The graphene nanoribbon powders are made in gram scale quantities via solution synthesis by the Sinitskii group at the University of Nebraska-Lincoln.[74, 73] Hydrogen terminated GNRs with no surface-ligands are made using solution synthesis, paving the way towards scalable manufacturing of graphene nanoribbon devices. Major challenges such as positioning, alignment, and electronic characterization remain. Dry contact transfer can cleanly place nanoribbons onto device-relevant substrates and also provides a venue for obtaining detailed electronic characterization of solution-synthesized nanoribbons, which was not previously possible due to problems with solvent residue.[73] The chevron graphene nanoribbon was chosen because it had already been well-characterized and studied, and could be compared to chevron graphene nanoribbons formed via on-surface polymerization.[77]

1.7 Graphene Nanoribbon Alignment and Positioning

A major barrier to the study and use of graphene nanoribbon devices is a lack of control over the positioning and alignment of graphene nanoribbons. Bottom-up synthesis typically results in random nanoribbon orientation and position. Ultimately atomic-scale control over nanoribbon position may be needed since transport through graphene nanoribbons is sensitive to the atomic details of the contact.[43, 72] Using the substrate as a template for constraining the orientation of the graphene nanoribbons offers some degree of control. So far, aligned graphene nanoribbons have been grown parallel to the step edges of miscut single crystals of gold, such as Au(788).[47] On Ge(100) semiconducting armchair graphene nanoribbons (lacking atomic precision) grow primarily along <110> directions.[34] Another promising avenue is attempting to locally drive the chemical synthesis of GNRs using an electron beam from an STM tip. While the STM is primarily used for imaging, the STM probe can also be used to interact with the surface. Tunneling electrons have been used to drive the Ullmann coupling of iodobenzene molecules,[32] and tunneling electrons can be used to dehalogenate DBBA[31] and dehydrogenate polyanthrylene,[10, 50] two of the key reactions for nanoribbon formation. STM imaging of DBBA deposited onto Cu(111) at a sample bias of at +3.5V and a tunneling current of 1 nA leads to debromination as indicated by the appearance of round protrusions and a decrease in height. The debromination reaction typically occurs at 200 °C on Au(111). For polyanthrylene annealed to 327 °C, below the typical 400 °C for dehydrogenation, partial graphene formation takes place. Placing the tip over an area to be dehydrogenated, and increasing the sample bias until a current change is detected leads to complete dehydrogenation. This thesis will examine progress towards tip-induced graphene nanoribbon fabrication.

1.8 Details on Thermal Self-assembly of Atomically Precise Graphene Nanoribbons

For nanoribbons to form from DBBA, several activation barriers must be overcome. There are barriers for precursor diffusion, C-Br bond cleavage, homoaromatic coupling, and cyclodehydrogenation.[8] Bromine atoms are placed on opposite ends of the precursor molecule, allowing for a one-dimensional polymer to form. Two tilted anthracene groups are required to ensure that precursors efficiently couple to each other. In the case of a single anthryl group, the molecule would lie flat on the surface. Polyanthrylene consists of anthryl groups at alternating angles to overcome steric hindrance and does not lie flat on the surface. By using a bianthryl molecule the activation energy required to form polyanthryelene is reduced, allowing for the formation of long polymer chains. Additional considerations are necessary for the choice of precursor molecules. For example, the chevron graphene nanoribbon precursor 6,11-dibromo-1,2,3,4-tetraphenyltriphenylene has its bromine atoms attached to a triphenylene group rather than the phenyl groups which have a rotational degree of freedom, ensuring that linking sites are always available 180 degrees apart from each other.

The noble metal surface acts as a catalyst for both Ullmann coupling and cyclodehydrogenation,[8, 9] so gold substrates are an appropriate starting point for tip-induced fabrication of GNRs. A series of experiments performed with the molecule 1,3,5 tris 4-bromophenyl benzene has demonstrated that substrate choice plays a significant role in the on-surface Ullman coupling of halogenated aromatic molecules. It was found that the temperature required for de-bromination and polymerization was lowest on copper, intermediate for silver, and highest on gold indicating their reactivities.[78] 1,3,5 tris 4-bromophenyl benzene does not polymerize on graphite surfaces because the molecular species desorb before Ullmann coupling can take place due to the lack of a catalytic substrate to lower the energy for C-Br bond cleavage.[29] For polyphenylene networks grown from hexa-iodo substituted macrocycle cyclohexa-m-phenylene precursors, the highest ordering was

achieved on gold surfaces.[7] The crystallographic orientation of the surface also plays a significant role by tuning the diffusivity of molecular species on the surface. The crystallographic orientation of the surface plays a significant role in determining its reactivity as well. For Ullmann coupling, (100) surfaces are the most reactive, followed by (110) and then (111) surfaces.[78] Substrate choice has drastic effects on the graphene nanoribbon synthesis. While DBBA forms 7A GNRs on Au(111), after some controversy, it was found that on Cu(111) surfaces chiral zigzag graphene nanoribbons form because edge-dehydrogenation of the nanoribbon precursors occurs before Ullmann coupling. On Cu(110) surfaces complete cyclodehydrogenation of the DBBA precursor takes place before Ullmann coupling, forming nanographene rather than nanoribbons.[65] Thermal self-assembly of DBBA on Au(110) does lead to N=7 armchair graphene nanoribbons, though at lower temperatures due to the higher reactivity of the surface.[54] The decreased mobility of the monomers leads to shorter graphene nanoribbons. Understanding, in detail, how the surface plays a role in graphene nanoribbon synthesis is critical for developing new synthetic strategies for achieving either better positional control during synthesis or growing graphene nanoribbons on new surfaces. The simple picture of carbon-halogen bonds breaking, reactive species diffusing on the surface, and polymer chains forming is not complete. The activation barrier for the polymerization reaction is lowered by organometallic intermediates that consist of C-metal-C bridges which are replaced by C-C bonds at higher temperatures.[26, 82, 85] The organometallic intermediates may be stabilized by the presence of halogen species, as was demonstrated for dibromobenzene on Cu(110).[24] STM imaging at low temperatures has been used to confirm the presence of an organometallic intermediate in the debromination of bromobenzene and fluoro-1-bromobenzene. Recently Simonov et al. reported the formation of organometallic chains when DBBA is deposited onto Ag(111)[63] yet an organometallic precursor to polyanthryelene formation on Au(111) has not yet been reported. X-ray photoelectron spectroscopy (XPS) studies of thermal GNR assembly indicate that there are distinct steps between C-Br cleavage and polyanthrylene formation.

While C-Br bonds cleave at 100 °C polyanthrylene does not form until 200 °C.[4, 64] This suggests a temperature window where dehalogenated species[7] are stable yet polyanthrylene does not form. XPS measurements show Br desorption occurs beyond 250 °C, in agreement with temperature programmed desorption studies.[13] The formation of species other than intact DBBA, polyanthrylene, and GNRs on Au(111) is not well documented. An STM study would provide more details that can aid in understanding the formation of graphene nanoribbons. Such a study is particularly important since such intermediates may form during tip-induced assembly and may be difficult to identify and distinguish.

1.9 Thesis Statement and Dissertation Structure

Some of the most pressing obstacles to using graphene nanoribbons in devices are developing techniques for accurately measuring the electronic bandgap of a graphene nanoribbon, cleanly placing nanoribbons onto device substrates, and positioning the nanoribbons to enable contact formation. Detailed electronic characterization of atomically precise graphene nanoribbons is lacking, in many cases, because the metal surfaces on which nanoribbons are studied have surface states that impede bandgap determination,[62] but also in the case of solution-synthesized nanoribbons solvent residue interferes with measurements. It is important to accurately measure the band structure of GNRs to aid in the quest to optimize nanoribbon geometry to achieve desirable electronic properties. Even if ideal nanoribbons can be made, on-surface polymerization and solution deposition typically result in nanoribbons randomly distributed over the surface, at a large variety of orientations. Positional control is necessary for one-dimensional materials, which is a key disadvantage for graphene nanoribbons not necessarily shared by 2D and 3D materials.

This thesis explores two closely related veins of research meant to tackle challenges towards making a graphene nanoribbon transistor. First I propose to measure the bandgaps of graphene nanoribbons transferred onto H:Si(100), a non-

metallic substrate. Cleanly transferring ribbons onto H:Si(100) under vacuum avoids challenges with metal surface states and residue and allows measurement of the local density of states of the GNRs via scanning tunneling spectroscopy. Secondly, I propose investigating whether electron-mediated synthesis can achieve positional control. Presently atomically precise graphene nanoribbons cannot be synthesized on insulating or semiconducting substrates, so positional control over graphene nanoribbon formation will be examined on a gold surface. Understanding the behavior of the molecules as they progress along reaction coordinates towards graphene nanoribbons can provide additional insights that may lead to better control over graphene nanoribbon synthesis.

The thesis is organized as follows: Chapter two covers dry contract transfer of solution-synthesized graphene nanoribbons onto H:Si(100). Chapter three discusses the dry contact transfer of extended chevron and hybrid GNRs. Chapter four explores positional control via tip-induced polymerization. Chapter 5 discusses future directions.

1.10 Figures

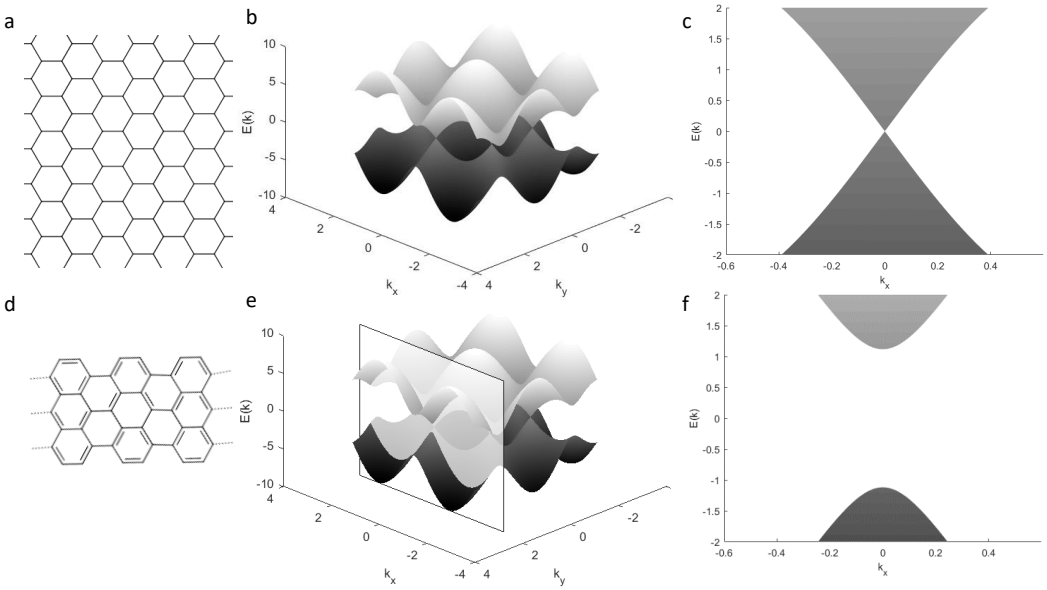

Figure 1.1: (a) The honeycomb lattice of graphene (b) A 3-dimensional view of the band structure of graphene showing 6 Dirac cones.[55] (c) A close-up of one of the Dirac cones showing the degeneracy at the Fermi level E=0. It should also be noted that the density of states vanishes at the Dirac point. (d) An N=7 armchair graphene nanoribbon (e) A plane containing a reciprocal lattice vector along the armchair direction is drawn. The electronic band structure of an armchair graphene nanoribbon can be approximated by projecting the band structure of graphene onto the plane indicated.[55] The narrow width of the nanoribbon forbids large scattering vectors in real space and small scattering vectors in reciprocal space, constraining the allowed k-points. (f) Qualitative illustration of how size confinement alters the bandgap of graphene.

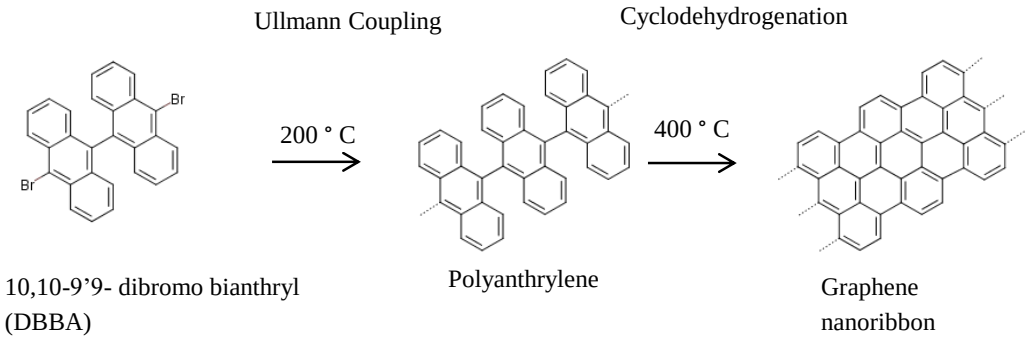

Figure 1.2: Schematic showing the major reaction steps for the synthesis of atomically precise graphene nanoribbons from the precursor 10,10-9'9- dibromo bianthryl. The process takes place at the indicated temperatures on a gold surface under ultra-high vacuum.

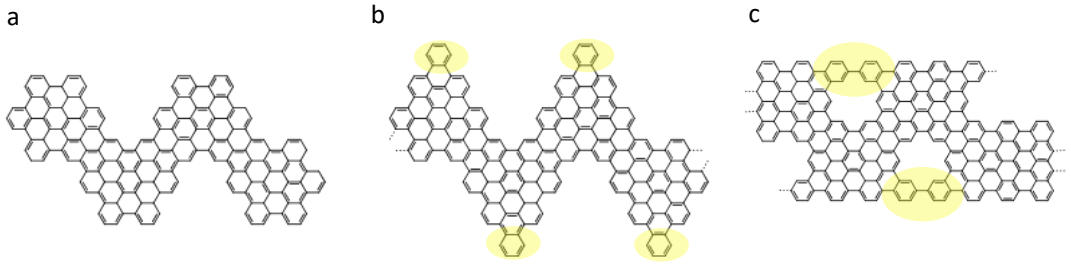

Figure 1.3: Overview of graphene nanoribbons to be examined via dry contact transfer onto H:Si(100) and scanning tunneling spectroscopy. (a) Chevron graphene nanoribbon (b) Extended chevron graphene nanoribbon with extra carbon atoms highlighted (c) Hybrid graphene nanoribbon with additional carbon atoms highlighted.

1.11 References

[1] Nasiba Abdurakhmanova, Nadja Amsharov, Sebastian Stepanow, Martin Jansen, Klaus Kern, and Konstantin Amsharov. Synthesis of wide atomically precise graphene nanoribbons from para-oligophenylene based molecular precursor. *Carbon*, 77:1187–1190, 2014.

[2] P. M. Albrecht and J. W. Lyding. Ultrahigh-vacuum scanning tunneling microscopy and spectroscopy of single-walled carbon nanotubes on hydrogen-passivated si(100) surfaces. *Applied Physics Letters*, 83(24):5029, 2003.

[3] Sebastian Anthony. Intel forges ahead to 10nm, will move away from silicon at 7nm. *Ars Technica*, February 2nd, 2015 2015.

[4] Arunabh Batra, Dean Cvetko, Gregor Kladnik, Olgun Adak, Claudia Cardoso, Andrea Ferretti, Deborah Prezzi, Elisa Molinari, Alberto Morgante, and Latha Venkataraman. Probing the mechanism for graphene nanoribbon formation on gold surfaces through x-ray spectroscopy. *Chem. Sci.*, 5(11):4419–4423, 2014.

[5] Patrick B. Bennett, Zahra Pedramrazi, Ali Madani, Yen-Chia Chen, Dimas G. de Oteyza, Chen Chen, Felix R. Fischer, Michael F. Crommie, and Jeffrey Bokor. Bottom-up graphene nanoribbon field-effect transistors. *Applied Physics Letters*, 103(25):253114, 2013.

[6] M. Bieri, M. Treier, J. Cai, K. Ait-Mansour, P. Ruffieux, O. Groning, P. Groning, M. Kastler, R. Rieger, X. Feng, K. Mullen, and R. Fasel. Porous graphenes: two-dimensional polymer synthesis with atomic precision. *Chem Commun (Camb)*, (45):6919–21, 2009.

[7] Marco Bieri, Manh-Thuong Nguyen, Oliver Groning, Jinming Cai, Matthias Treier, Kamel Ait-Mansour, Pascal Ruffieux, Carlo A Pignedoli, Daniele Passerone, and Marcel Kastler. Two-dimensional polymer formation on surfaces: insight into the roles of precursor mobility and reactivity. *Journal of the American Chemical Society*, 132(46):16669–16676, 2010.

[8] J. Bjork, F. Hanke, and S. Stafstrom. Mechanisms of halogen-based covalent self-assembly on metal surfaces. *J Am Chem Soc*, 135(15):5768–75, 2013.

[9] J. Bjork, S. Stafstrom, and F. Hanke. Zipping up: cooperativity drives the synthesis of graphene nanoribbons. *J Am Chem Soc*, 133(38):14884–7, 2011.

[10] Stephan Blankenburg, Jinming Cai, Pascal Ruffieux, Rached Jaafar, Daniele Passerone, Xinliang Feng, Klaus Müllen, Roman Fasel, and Carlo A. Pignedoli. Intraribbon heterojunction formation in ultranarrow graphene nanoribbons. *ACS Nano*, 6(3):2020–2025, 2012.

[11] L. Brey and H. A. Fertig. Electronic states of graphene nanoribbons studied with the dirac equation. *Physical Review B*, 73(23), 2006.

[12] C. Bronner, S. Stremlau, M. Gille, F. Brausse, A. Haase, S. Hecht, and P. Tegeder. Aligning the band gap of graphene nanoribbons by monomer doping. *Angew Chem Int Ed Engl*, 52(16):4422–5, 2013.

[13] Christopher Bronner, Jonas Björk, and Petra Tegeder. Tracking and removing br during the on-surface synthesis of a graphene nanoribbon. *The Journal of Physical Chemistry C*, 119(1):486–493, 2015.

[14] J. Cai, P. Ruffieux, R. Jaafar, M. Bieri, T. Braun, S. Blankenburg, M. Muoth, A. P. Seitsonen, M. Saleh, X. Feng, K. Mullen, and R. Fasel. Atomically precise bottom-up fabrication of graphene nanoribbons. *Nature*, 466(7305):470–3, 2010.

[15] C Julian Chen. *Introduction to scanning tunneling microscopy*, volume 2. Oxford University Press New York, 1993.

[16] L. Chen, L. He, H. S. Wang, H. Wang, S. Tang, C. Cong, H. Xie, L. Li, H. Xia, T. Li, T. Wu, D. Zhang, L. Deng, T. Yu, X. Xie, and M. Jiang. Oriented graphene nanoribbons embedded in hexagonal boron nitride trenches. *Nat Commun*, 8:14703, 2017.

[17] Liping Chen, Linjun Wang, and David Beljonne. Designing coved graphene nanoribbons with charge carrier mobility approaching that of graphene. *Carbon*, 77:868–879, 2014.

[18] Y. Chen, T. Jayasekera, A. Calzolari, K. W. Kim, and M. B. Nardelli. Thermoelectric properties of graphene nanoribbons, junctions and superlattices. *J Phys Condens Matter*, 22(37):372202, 2010.

[19] Y. C. Chen, T. Cao, C. Chen, Z. Pedramrazi, D. Haberer, D. G. de Oteyza, F. R. Fischer, S. G. Louie, and M. F. Crommie. Molecular bandgap engineering of bottom-up synthesized graphene nanoribbon heterojunctions. *Nat Nanotechnol*, 10(2):156–60, 2015.

[20] Y. C. Chen, D. G. de Oteyza, Z. Pedramrazi, C. Chen, F. R. Fischer, and M. F. Crommie. Tuning the band gap of graphene nanoribbons synthesized from molecular precursors. *ACS Nano*, 7(7):6123–8, 2013.

[21] Ryan R. Cloke, Tomas Marangoni, Giang D. Nguyen, Trinity Joshi, Daniel J. Rizzo, Christopher Bronner, Ting Cao, Steven G. Louie, Michael F. Crommie, and Felix R. Fischer. Site-specific substitutional boron doping of semiconducting armchair graphene nanoribbons. *Journal of the American Chemical Society*, 137(28):8872–8875, 2015.

[22] O. Deniz, C. Sanchez-Sanchez, T. Dumslaff, X. Feng, A. Narita, K. Mullen, N. Kharche, V. Meunier, R. Fasel, and P. Ruffieux. Revealing the electronic structure of silicon intercalated armchair graphene nanoribbons by scanning tunneling spectroscopy. *Nano Lett*, 2017.

[23] Sujay B. Desai, Surabhi R. Madhvapathy, Angada B. Sachid, Juan Pablo Llinas, Qingxiao Wang, Geun Ho Ahn, Gregory Pitner, Moon J. Kim, Jeffrey Bokor, Chenming Hu, H.-S. Philip Wong, and Ali Javey. Mos2 transistors with 1-nanometer gate lengths. *Science*, 354(6308):99–102, 2016.

[24] Marco Di Giovannantonio, Mohamed El Garah, Josh Lipton-Duffin, Vincent Meunier, Luis Cardenas, Yannick Fagot Revurat, Albano Cossaro, Alberto Verdini, Dmitrii F. Perepichka, Federico Rosei, and Giorgio Contini. Insight into organometallic intermediate and its evolution to covalent bonding in surface-confined ullmann polymerization. *ACS Nano*, 7(9):8190–8198, 2013.

[25] Z. Dong and J. Guo. Assessment of 2-d transition metal dichalcogenide fets at sub-5-nm gate length scale. *IEEE Transactions on Electron Devices*, 64(2):622–628, 2017.

[26] J. Eichhorn, T. Strunskus, A. Rastgoo-Lahrood, D. Samanta, M. Schmittel, and M. Lackinger. On-surface ullmann polymerization via intermediate organometallic networks on ag(111). *Chem Commun (Camb)*, 50(57):7680–2, 2014.

[27] Xinliang Feng, Jishan Wu, Min Ai, Wojciech Pisula, Linjie Zhi, Jürgen P Rabe, and Klaus Müllen. Triangle-shaped polycyclic aromatic hydrocarbons. *Angewandte Chemie*, 119(17):3093–3096, 2007.

[28] Mitsutaka Fujita, Katsunori Wakabayashi, Kyoko Nakada, and Koichi Kusakabe. Peculiar localized state at zigzag graphite edge. *Journal of the Physical Society of Japan*, 65(7):1920–1923, 1996.

[29] R. Gutzler, H. Walch, G. Eder, S. Kloft, W. M. Heckl, and M. Lackinger. Surface mediated synthesis of 2d covalent organic frameworks: 1,3,5-tris(4-bromophenyl)benzene on graphite(001), cu(111), and ag(110). *Chem Commun (Camb)*, (29):4456–8, 2009.

[30] M. Y. Han, B. Ozyilmaz, Y. Zhang, and P. Kim. Energy band-gap engineering of graphene nanoribbons. *Phys Rev Lett*, 98(20):206805, 2007.

[31] Patrick Han, Kazuto Akagi, Filippo Federici Canova, Hirotaka Mutoh, Susumu Shiraki, Katsuya Iwaya, Paul S Weiss, Naoki Asao, and Taro Hitosugi. Bottom-up graphene-nanoribbon fabrication reveals chiral edges and enantioselectivity. *ACS nano*, 2014.

[32] Saw-Wai Hla, Ludwig Bartels, Gerhard Meyer, and Karl-Heinz Rieder. Inducing all steps of a chemical reaction with the scanning tunneling microscope tip: towards single molecule engineering. *Physical review letters*, 85(13):2777, 2000.

[33] Han Huang, Dacheng Wei, Jiatao Sun, Swee Liang Wong, Yuan Ping Feng, A. H. Castro Neto, and Andrew Thye Shen Wee. Spatially resolved electronic structures of atomically precise armchair graphene nanoribbons. *Scientific Reports*, 2:983, 2012.

[34] R. M. Jacobberger, B. Kiraly, M. Fortin-Deschenes, P. L. Levesque, K. M. McElhinny, G. J. Brady, R. Rojas Delgado, S. Singha Roy, A. Mannix, M. G. Lagally, P. G. Evans, P. Desjardins, R. Martel, M. C. Hersam, N. P. Guisinger, and M. S. Arnold. Direct oriented growth of armchair graphene nanoribbons on germanium. *Nat Commun*, 6:8006, 2015.

[35] S. J. Jeong, S. Jo, J. Lee, K. Yang, H. Lee, C. S. Lee, H. Park, and S. Park. Self-aligned multichannel graphene nanoribbon transistor arrays fabricated at wafer scale. *Nano Lett*, 16(9):5378–85, 2016.

[36] J Jiang, R Saito, Ge G Samsonidze, A Jorio, SG Chou, G Dresselhaus, and MS Dresselhaus. Chirality dependence of exciton effects in single-wall carbon nanotubes: Tight-binding model. *Physical Review B*, 75(3):035407, 2007.

[37] Liying Jiao, Xinran Wang, Georgi Diankov, Hailiang Wang, and Hongjie Dai. Facile synthesis of high-quality graphene nanoribbons. *Nat Nano*, 5(5):321–325, 2010.

[38] A Jorio, R Saito, JH Hafner, CM Lieber, dM Hunter, T McClure, G Dresselhaus, and MS Dresselhaus. Structural (n, m) determination of isolated single-wall carbon nanotubes by resonant raman scattering. *Physical Review Letters*, 86(6):1118, 2001.

[39] T. Kato and R. Hatakeyama. Site- and alignment-controlled growth of graphene nanoribbons from nickel nanobars. *Nat Nanotechnol*, 7(10):651–6, 2012.

[40] S. Kawai, S. Saito, S. Osumi, S. Yamaguchi, A. S. Foster, P. Spijker, and E. Meyer. Atomically controlled substitutional boron-doping of graphene nanoribbons. *Nat Commun*, 6:8098, 2015.

[41] N. Kharche and V. Meunier. Width and crystal orientation dependent band gap renormalization in substrate-supported graphene nanoribbons. *J Phys Chem Lett*, 7(8):1526–33, 2016.

[42] A. Kimouche, M. M. Ervasti, R. Drost, S. Halonen, A. Harju, P. M. Joensuu, J. Sainio, and P. Liljeroth. Ultra-narrow metallic armchair graphene nanoribbons. *Nat Commun*, 6:10177, 2015.

[43] M. Koch, F. Ample, C. Joachim, and L. Grill. Voltage-dependent conductance of a single graphene nanoribbon. *Nat Nanotechnol*, 7(11):713–7, 2012.

[44] Dmitry V. Kosynkin, Amanda L. Higginbotham, Alexander Sinitskii, Jay R. Lomeda, Ayrat Dimiev, B. Katherine Price, and James M. Tour. Longitudinal unzipping of carbon nanotubes to form graphene nanoribbons. *Nature*, 458(7240):872–876, 2009.

[45] Xiaolin Li, Xinran Wang, Li Zhang, Sangwon Lee, and Hongjie Dai. Chemically derived, ultrasmooth graphene nanoribbon semiconductors. *Science*, 319(5867):1229–1232, 2008.

[46] Y. Y. Li, M. X. Chen, M. Weinert, and L. Li. Direct experimental determination of onset of electron-electron interactions in gap opening of zigzag graphene nanoribbons. *Nat Commun*, 5:4311, 2014.

[47] S. Linden, D. Zhong, A. Timmer, N. Aghdassi, J. H. Franke, H. Zhang, X. Feng, K. Müllen, H. Fuchs, L. Chi, and H. Zacharias. Electronic structure of spatially aligned graphene nanoribbons on au(788). *Physical Review Letters*, 108(21), 2012.

[48] Junzhi Liu, Bo-Wei Li, Yuan-Zhi Tan, Angelos Giannakopoulos, Carlos Sanchez-Sanchez, David Beljonne, Pascal Ruffieux, Roman Fasel, Xinliang Feng, and Klaus Müllen. Toward cove-edged low band gap graphene nanoribbons. *Journal of the American Chemical Society*, 137(18):6097–6103, 2015.

[49] Meizhuang Liu, Mengxi Liu, Limin She, Zeqi Zha, Jinliang Pan, Shichao Li, Tao Li, Yangyong He, Zeying Cai, Jiaobing Wang, Yue Zheng, Xiaohui Qiu, and Dingyong Zhong. Graphene-like nanoribbons periodically embedded with four- and eight-membered rings. *Nature Communications*, 8:14924, 2017.

[50] Chuanxu Ma, Zhongcan Xiao, Honghai Zhang, Liangbo Liang, Jingsong Huang, Wenchang Lu, Bobby G Sumpter, Kunlun Hong, J Bernholc, and An-Ping Li. Controllable conversion of quasi-freestanding polymer chains to graphene nanoribbons. *Nature Communications*, 8:14815, 2017.

[51] G. Z. Magda, X. Jin, I. Hagymasi, P. Vancso, Z. Osvath, P. Nemes-Incze, C. Hwang, L. P. Biro, and L. Tapaszto. Room-temperature magnetic order on zigzag edges of narrow graphene nanoribbons. *Nature*, 514(7524):608–11, 2014.

[52] K. Majumdar, C. Hobbs, and P. D. Kirsch. Benchmarking transition metal dichalcogenide mosfet in the ultimate physical scaling limit. *IEEE Electron Device Letters*, 35(3):402–404, 2014.

[53] J. A. Martin-Gago. Polycyclic aromatics: On-surface molecular engineering. *Nat Chem*, 3(1):11–2, 2011.

[54] Lorenzo Massimi, Oualid Ourdjini, Leif Lafferentz, Matthias Koch, Leonhard Grill, Emanuele Cavaliere, Luca Gavioli, Claudia Cardoso, Deborah Prezzi, Elisa Molinari, Andrea Ferretti, Carlo Mariani, and Maria Grazia Betti. Surface-assisted reactions toward formation of graphene nanoribbons on au(110) surface. *The Journal of Physical Chemistry C*, 119(5):2427–2437, 2015.

[55] Kyoko Nakada, Mitsutaka Fujita, Gene Dresselhaus, and Mildred S. Dresselhaus. Edge state in graphene ribbons: Nanometer size effect and edge shape dependence. *Physical Review B*, 54(24):17954–17961, 1996.

[56] Jeffrey B Neaton, Mark S Hybertsen, and Steven G Louie. Renormalization of molecular electronic levels at metal-molecule interfaces. *Physical review letters*, 97(21):216405, 2006.

[57] P. Nemes-Incze, Levente Tapaszt, G. Zs Magda, Z. Osváth, G. Dobrik, X. Jin, C. Hwang, and L. P. Bir. Graphene nanoribbons with zigzag and armchair edges prepared by scanning tunneling microscope lithography on gold substrates. *Applied Surface Science*, 291:48–52, 2014.

[58] Giang D Nguyen, Francesca M Toma, Ting Cao, Zahra Pedramrazi, Chen Chen, Daniel J Rizzo, Trinity Joshi, Christopher Bronner, Yen-Chia Chen, and Marco Favaro. Bottom-up synthesis of n= 13 sulfur-doped graphene nanoribbons. *The Journal of Physical Chemistry C*, 120(5):2684–2687, 2016.

[59] P. Olszowski, B. Zapotoczny, J. S. Prauzner-Bechcicki, M. Vilas-Varela, D. Pérez, E. Guitián, D. Peña, and M. Szymonski. Aryl halide c–c coupling on ge(001):h surfaces. *The Journal of Physical Chemistry C*, 119(49):27478–27482, 2015.

[60] Carlos-Andres Palma, Manohar Awasthi, Yenny Hernandez, Xinliang Feng, Klaus Müllen, Thomas A. Niehaus, and Johannes V. Barth. Sub-nanometer width armchair graphene nanoribbon energy gap atlas. *The Journal of Physical Chemistry Letters*, 6(16):3228–3235, 2015.

[61] K. A. Ritter and J. W. Lyding. The influence of edge structure on the electronic properties of graphene quantum dots and nanoribbons. *Nat Mater*, 8(3):235–42, 2009.

[62] Pascal Ruffieux, Shiyong Wang, Bo Yang, Carlos Sánchez-Sánchez, Jia Liu, Thomas Dienel, Leopold Talirz, Prashant Shinde, Carlo A. Pignedoli, Daniele Passerone, Tim Dumslaff, Xinliang Feng, Klaus Müllen, and Roman Fasel. On-surface synthesis of graphene nanoribbons with zigzag edge topology. *Nature*, 531(7595):489–492, 2016.

[63] Konstantin Simonov. *Effect of Substrate on Bottom-Up Fabrication and Electronic Properties of Graphene Nanoribbons*. Thesis, 2016.

[64] Konstantin A. Simonov, Nikolay A. Vinogradov, Alexander S. Vinogradov, Alexander V. Generalov, Elena M. Zagrebina, Nils Martensson, Attilio A. Cafolla, Tomas Carpy, John P. Cunniffe, and Alexei B. Preobrajenski. Effect of substrate chemistry on the bottom-up fabrication of graphene nanoribbons: Combined core-level spectroscopy and stm study. *The Journal of Physical Chemistry C*, 118(23):12532–12540, 2014.

[65] Konstantin A. Simonov, Nikolay A. Vinogradov, Alexander S. Vinogradov, Alexander V. Generalov, Elena M. Zagrebina, Gleb I. Svirskiy, Attilio A. Cafolla, Thomas Carpy, John P. Cunniffe, Tetsuya Taketsugu, Andrey Lyalin, Nils Martensson, and Alexei B. Preobrajenski. From graphene nanoribbons on cu(111) to nanographene on cu(110): Critical role of substrate structure in the bottom-up fabrication strategy. *ACS Nano*, 9(9):8997–9011, 2015.

[66] Y. W. Son, M. L. Cohen, and S. G. Louie. Energy gaps in graphene nanoribbons. *Phys Rev Lett*, 97(21):216803, 2006.

[67] Y. W. Son, M. L. Cohen, and S. G. Louie. Half-metallic graphene nanoribbons. *Nature*, 444(7117):347–9, 2006.

[68] L. Talirz, H. Sode, T. Dumslaff, S. Wang, J. R. Sanchez-Valencia, J. Liu, P. Shinde, C. A. Pignedoli, L. Liang, V. Meunier, N. C. Plumb, M. Shi, X. Feng, A. Narita, K. Mullen, R. Fasel, and P. Ruffieux. On-surface synthesis and characterization of 9-atom wide armchair graphene nanoribbons. *ACS Nano*, 11(2):1380–1388, 2017.

[69] L. Tapaszto, G. Dobrik, P. Lambin, and L. P. Biro. Tailoring the atomic structure of graphene nanoribbons by scanning tunnelling microscope lithography. *Nat Nanotechnol*, 3(7):397–401, 2008.

[70] Kristian S. Thygesen and Angel Rubio. Renormalization of molecular quasiparticle levels at metal-molecule interfaces: Trends across binding regimes. *Physical Review Letters*, 102(4), 2009.

[71] M. Treier, P. Ruffieux, P. Groning, S. Xiao, C. Nuckolls, and R. Fasel. An aromatic coupling motif for two-dimensional supramolecular architectures. *Chem Commun (Camb)*, (38):4555–7, 2008.

[72] J. van der Lit, M. P. Boneschanscher, D. Vanmaekelbergh, M. Ijas, A. Uppstu, M. Ervasti, A. Harju, P. Liljeroth, and I. Swart. Suppression of electron-vibron coupling in graphene nanoribbons contacted via a single atom. *Nat Commun*, 4:2023, 2013.

[73] T. H. Vo, M. Shekhirev, D. A. Kunkel, M. D. Morton, E. Berglund, L. Kong, P. M. Wilson, P. A. Dowben, A. Enders, and A. Sinitskii. Large-scale solution synthesis of narrow graphene nanoribbons. *Nat Commun*, 5:3189, 2014.

[74] T. H. Vo, M. Shekhirev, D. A. Kunkel, M. D. Morton, E. Berglund, L. M. Kong, P. M. Wilson, P. A. Dowben, A. Enders, and A. Sinitskii. Large-scale solution synthesis of narrow graphene nanoribbons. *Nature Communications*, 5:3189, 2014.

[75] T. H. Vo, M. Shekhirev, D. A. Kunkel, F. Orange, M. J. Guinel, A. Enders, and A. Sinitskii. Bottom-up solution synthesis of narrow nitrogen-doped graphene nanoribbons. *Chem Commun (Camb)*, 50(32):4172–4, 2014.

[76] Timothy H. Vo, U. Gayani E. Perera, Mikhail Shekhirev, Mohammad Mehdi Pour, Donna A. Kunkel, Haidong Lu, Alexei Gruverman, Eli Sutter, Mircea Cotlet, Dmytro Nykypanchuk, Percy Zahl, Axel Enders, Alexander Sinitskii, and Peter Sutter. Nitrogen-doping induced self-assembly of graphene nanoribbon-based two-dimensional and three-dimensional metamaterials. *Nano Letters*, 15(9):5770–5777, 2015.

[77] Timothy H. Vo, Mikhail Shekhirev, Alexey Lipatov, Rafal A. Korlacki, and Alexander Sinitskii. Bulk properties of solution-synthesized chevron-like graphene nanoribbons. *Faraday Discussions*, 173(0):105–113, 2014.

[78] Hermann Walch, Rico Gutzler, Thomas Sirtl, Georg Eder, and Markus Lackinger. Material-and orientation-dependent reactivity for heterogeneously catalyzed carbon bromine bond homolysis. *The Journal of Physical Chemistry C*, 114(29):12604–12609, 2010.

[79] J. Wang, L. Ma, Q. Yuan, L. Zhu, and F. Ding. Transition-metal-catalyzed unzipping of single-walled carbon nanotubes into narrow graphene nanoribbons at low temperature. *Angew Chem Int Ed Engl*, 50(35):8041–5, 2011.

[80] S. Wang, L. Talirz, C. A. Pignedoli, X. Feng, K. Mullen, R. Fasel, and P. Ruffieux. Giant edge state splitting at atomically precise graphene zigzag edges. *Nat Commun*, 7:11507, 2016.

[81] Shudong Wang and Jinlan Wang. Quasiparticle energies and optical excitations in chevron-type graphene nanoribbon. *The Journal of Physical Chemistry C*, 116(18):10193–10197, 2012.

[82] W. Wang, X. Shi, S. Wang, M. A. Van Hove, and N. Lin. Single-molecule resolution of an organometallic intermediate in a surface-supported ullmann coupling reaction. *J Am Chem Soc*, 133(34):13264–7, 2011.

[83] Wen-Xiao Wang, Mei Zhou, Xinqi Li, Si-Yu Li, Xiaosong Wu, Wenhui Duan, and Lin He. Energy gaps of atomically precise armchair graphene sidewall nanoribbons. *Physical Review B*, 93(24), 2016.

[84] Z. Q. Yu, C. M. Wang, Y. Du, S. Thevuthasan, and I. Lyubinetsky. Reproducible tip fabrication and cleaning for uhv stm. *Ultramicroscopy*, 108(9):873–7, 2008.

[85] H. Zhang and L. Chi. Gold-organic hybrids: On-surface synthesis and perspectives. *Adv Mater*, 2016.

CHAPTER 2

SOLUTION-SYNTHESIZED CHEVRON GRAPHENE NANORIBBONS EXFOLIATED ONTO H:SI(100)

2.1 Introduction

The versatility of bottom-up synthesis promises sophisticated GNR electronics, including transistors and quantum dot qubits,[7] which exhibit long spin coherence times.[41] To fabricate GNR devices, the development of a clean transfer is needed to move nanoribbons from the metal growth surface onto a device compatible substrate such as SiO_2. A wet transfer method previously demonstrated leaves organic residue that degrades device performance.[2]

A dry contact transfer (DCT) technique was developed in the Lyding group specifically to overcome the challenge of cleanly placing carbon nanomaterials onto semiconducting surfaces for ultrahigh vacuum scanning tunneling microscopy (UHV-STM) characterization.[1] Since the tip-sample junction is extremely sensitive to the presence of solvent molecules and mobile adsorbates, atomic-scale cleanliness is required. DCT has previously enabled detailed characterization of carbon nanotubes,[1, 35, 34] and graphene nanoflakes.[12, 17, 31] Fortuitously gram-scale quantities of atomically precise GNRs can be obtained via solution synthesis,[44, 46] allowing a fiberglass applicator to be coated for deposition of GNRs onto arbitrary surfaces. One may envision using a bare applicator to pick up surface-grown nanoribbons, however the transfer efficiency may be prohibitively low. So far, detailed electronic characterization has been limited for solution-

[1]Material in this chapter is modified and reproduced with permission from A. Radocea, T. Sun, T. Vo, A. Sinitskii, N. R. Aluru, and J. W. Lyding, "Solution-Synthesized Chevron Graphene Nanoribbons Exfoliated onto H:Si(100)," Nano Letters, vol. 17, no. 1, pp. 170-178, 2017. Copyright 2017 American Chemical Society.

synthesized nanoribbons, in part due to the use of ambient solvent-based deposition processes that interfere with STM spectroscopic characterization. When drop-casting nanoribbons onto surfaces, residue cannot be fully removed from the surface under conditions that do not also remove the GNRs.[45] Solution-synthesized graphene nanoribbons may feature additional side alkyl chains attached to graphene nanoribbon edges in order to increase GNR solubility.[36, 26] The alkyl groups may hinder electronic transport, especially in inter-GNR nanojunctions. In this study, the chevron graphene nanoribbons studied are hydrogen-terminated and have the same structure as chevron graphene nanoribbons synthesized via on-surface polymerization.[4]

The fabrication of GNRs via solution synthesis[44, 46] promises to be an avenue towards large-scale GNR manufacturing, however a lack of detailed atomic-scale imaging and electronic characterization poses a potential roadblock. This chapter shows how DCT avoids problems with solvent residue to overcome previous limitations and cleanly deposit armchair edged chevron GNRs directly onto H:Si(100). STM spectroscopy of the system reveals a 2.85 eV GNR bandgap, spatial and electronic mapping of the GNR electronic states, and metallic behavior for GNRs in contact with deliberately unpassivated silicon. The high spatial resolution spectroscopy achieved shows details of the electronic structure of chevron GNRs that have not yet been previously reported. To better understand the experimental results, first-principles density functional theory (DFT) simulations were carried out by Tao Sun in Professor Narayana Aluru's group. The DFT results are presented throughout the chapter and played a significant role in identifying the GNR electronic states. Depassivating H:Si(100) via STM nanolithography allowed the study of GNR-Si interactions, showing a semiconducting-to-metallic transition. We also find bilayer GNR junctions on the surface, formed by overlapping GNRs.

2.2 Imaging of Chevron Graphene Nanoribbons on H:Si(100)

The solution synthesis of chevron GNRs used for this study (Figure 2.1a) was carried out by Professor Alexander Sinitskii's group at the University of Nebraska-Lincoln and is described in a previously published protocol.[44] From the synthesis, a graphene nanoribbon powder is obtained, which is then applied to a frayed fiber-glass DCT applicator. A high temperature (300 – 500 °C) degas of the GNR-coated fiberglass applicator removes solvents and atmospheric contaminants. When the DCT applicator is manually pressed against the silicon surface under ultrahigh vacuum, nanoribbons cleanly exfoliate onto the surface (Figure 2.1b). Figure 2.1c is a room temperature STM image showing two chevron GNRs lying flat on the surface. Although the STM topographs in Figure 1 were all recorded at a sample bias of –2 V and a tunneling current of 10 pA, different imaging artifacts appear, potentially caused by variations in the density of states of the STM probe.

A high-resolution image (Figure 2.1e) shows intra-ribbon resolution not corresponding to the silicon dimer rows. The STM images presented in Figure 2.1 are suggestive of a clean transfer process when compared to previous STM imaging of GNRs transferred onto gold via solution deposition.[44] The graphene nanoribbons do not appear to align to the silicon lattice, indicating a weak coupling interaction (Figure 2.2). In Figure 2.1c-e silicon rows and individual dimers appear underneath the GNRs. This semitransparency effect was previously observed for graphene flakes on III-V semiconductors and arises when the forces between the tip and the flake push the graphene closer to the surface.[12] A similar effect was not observed for graphene flakes <8 nm in diameter on H:Si(100).[31] In contrast to graphene nanoflakes, the atomically precise chevron nanoribbons studied do show semitransparency, due to having a bandgap larger than the underlying substrate, allowing the silicon density of states to dominate the tunneling current.

Of 115 GNRs imaged at both positive and negative sample bias, 80 are imaged

as non-transparent, exhibiting an average apparent height of 3.0 Å relative to the surrounding silicon substrate. The 35 semitransparent nanoribbons had an average apparent height of 2.0 Å. An example of the analysis applied to determine GNR heights is shown in Figure 2.3. Semi-transparency is not an intrinsic property of GNRs, but an imaging artifact that arises when the STM probe pushes the GNR closer to the surface, allowing the tunneling current from the substrate to contribute to the STM topograph. As shown in Figure 2.4a,b the same GNR can appear as semitransparent or non-transparent under the same sample bias and tunneling current. Semitransparency is influenced by the tip-sample separation which can vary with the work function of the STM probe, as well as the interaction of the graphene nanoribbon with the surface. Chevron GNRs imaged on Au(111) show an apparent height of 1.8 Å,[4] which is significantly smaller than the apparent height observed for the non-transparent nanoribbons on H:Si(100). A previous study determined a 3.1 Å apparent height for graphene nanoflakes on H:Si(100).[31] The graphene lattice is only observed for nontransparent GNRs, indicating that the carbon plane is at a height near 3.0 Å. Since the inter-layer spacing of graphite is 3.3 Å, a van der Waals bonding interaction between the GNR and the H:Si(100) substrate is possible, although the apparent height is dictated by the local density of states (LDOS) and is not sufficient to determine atomic positions. The H:Si-GNR interaction is weak enough to enable movement of the GNR using the STM tip as shown in Figure 2.5.

2.3 Electronic Characterization of Chevron GNRs on H:Si(100)

DFT modeling of chevron GNRs, including the results shown in Figure 2.7e, predicts a 1.50-1.57 eV bandgap.[21, 44, 47] While for graphene nanostructures DFT captures reliable information about energy level ordering, orbital shapes and the spatial distribution of the LDOS,[33] it underestimates bandgaps. Corrections to DFT modeling made with the GW approximation predict an expected quasipar-

ticle bandgap of 3.62- 3.74 eV.[21, 47] However, when the substrate is included in the simulation, a screening interaction decreases the GNR bandgap.[9, 27, 39, 40] The estimated bandgap for chevron GNRs on Au(111) is predicted to be 2.96 eV.[21]

UV-vis-NIR spectroscopy and photoluminescence spectroscopy of solution- synthesized chevron gaphene nanoribbons suggest a 1.6-1.8 eV bandgap for ensembles of GNRs.[43, 46] However, these measurements probe the optical bandgap and neglect the exciton binding energy. The quasiparticle bandgap determined with angle-resolved ultraviolet photoemission (ARUPS) studies of chevron GNRs on Au(788) is 3.1 +/- 0.4 eV[23] and high-resolution energy electron loss spectroscopy (HREELS) estimates a 2.8 +/- 0.3 eV bandgap,[3] in close agreement with the theoretical GW predictions. STS data for pristine chevron GNRs on Au(111) are presented in two recent studies and similar bandgaps of 2.0 eV were reported.[5, 43] Studying the bandgap of solution-synthesized GNRs on H:Si(100) is important to confirm their electronic properties, and in understanding how GNR-H:Si(100) interactions modify the bandgap.

STM spectroscopy of GNRs is sometimes limited to point spectroscopy,[13] and tunneling conductance (dI/dV) maps,[95] which may not fully capture the electronic landscape of GNRs. Current imaging tunneling spectroscopy (CITS) was used to collect I-V spectra over 50 x 50 points to examine a GNR and the surrounding substrate at 512 sample biases between -2 V and + 3 V. Bandgap determination of atomically thin GNRs requires careful analysis because STS simultaneously probes both the GNR and the substrate. For GNRs on Au(111), a broadened surface state prevents the observation of the edge state of atomically precise zigzag GNRs.[32, 33] The STS measurements of chevron GNRs on H:Si(100) also show a significant substrate contribution.

Figure 2.6 illustrates the detection of substrate states underneath a GNR during scanning tunneling spectroscopy measurements. An STM topograph of the chevron GNR that was examined with CITS is shown in Figure 2.6a. Normalized conductance plots for three of the points corresponding to the GNR center, GNR edge, and the H:Si(100) surface are shown in Figure 2.6b, along with an

inset showing the topograph acquired simultaneously with CITS. Spectroscopy measured at the GNR center shows additional features resembling the peaks observed over the silicon substrate, indicating that the surface is contributing to the STS measurement (Figure 2.6c). A normalized conductance spectra map shown in Figure 2.6d shows how the density of states varies along the width of the GNR. The dashed vertical lines indicate the positions of the points plotted in Figure 2.6b. The normalized conductance at the center of the GNR shows contributions from the silicon valence band (VB) and conduction band (CB), shifted from their original positions due to interactions with the GNR. At higher energies, tunneling conductance peaks appear due to the GNR conduction and valence band states.

Remarkably, the silicon surface electronic structure is less pronounced at the GNR edge. The spatial distribution of the states identified as the silicon conduction band (Si CB) and the silicon valence band (Si VB) can be shown in the normalized tunneling conductance plots at sample biases of -0.62 V (+ 1.33 V) which are in Figure 2.6e (f). For both plots, the edges of the GNR are darker than the substrate and darker than the center of the GNR. A periodic modulation of the density of states commensurate with the silicon lattice supports the assignment of the silicon CB and VB states.

To more clearly depict the GNR states, spectroscopy collected along the edge of the GNR is shown in Figure 2.7. The normalized tunneling conductance spectral traces shown in Figure 2.7a and the corresponding spectra map shown in Figure 2.7b highlight states at -1.47 V, -1.17 V, 2.0 V, and 2.27 V, which are identified as the GNR VB-1, VB, CB, and CB + 1 states. To ensure that the GNR states are identified correctly, first principles simulations were used to simulate an infinite GNR with periodic boundary conditions and an isolated GNR comprising 6 unit cells (all edges terminated with hydrogen atoms) with a length comparable to that of the GNR experimentally examined. Figure 2.7d shows simulated normalized LDOS maps produced by selecting peaks in the DFT-calculated projected density of states (PDOS) indicated in Figure 2.7c and mapping them onto spatial coordinates for the 6-unit cell GNR. The LDOS contours are shown at a constant height

of 4 Å above the graphene plane. We estimate the distance between the tip and graphene sample plane is 4 Å. Tip-sample separation has previously been shown to have a significant effect on dI/dV imaging because of the three-dimensional distribution of the GNR LDOS.[8] (Additional LDOS maps at varying heights above the graphene plane, and the full LDOS maps are provided in Figure 2.13).

As shown in Figure 2.7c, the bandgap predicted with DFT for both infinite and 6-unit cell GNRs is about 1.6 eV. The more accurate GW approximation was only applied for the infinite GNR and the band structure in Figure 2e shows a quasiparticle band gap of 3.56 eV, which is consistent with previous studies.[47, 21] It also reveals that the band orders and band shapes within quasiparticle band structures are in agreement with those from Kohn-Sham band structures, confirming the fact that DFT could accurately capture this information for graphene nanostructures,[33] hence the LDOS obtained from DFT are reasonable. The simulated LDOS for the 6-unit cell GNR is compared to experimental normalized dI/dV maps in Figure 2.7e. Due to the huge computational cost, the silicon substrate was not included for the 6-unit cell GNR. (Figure 2.15 and show additional LDOS maps including the substrate for an infinite GNR.)

The simulated GNR VB-1 and VB states show good agreement with the normalized dI/dV maps. The valence band state at -1.17 V is located at the ends of the GNR, while the VB-1 state observed at -1.43 V is in the middle of the GNR. Analogous finite length effects were previously observed in dI/dV maps of carbon nanowires and straight armchair nanoribbons on gold.[16, 42] The simulated conduction band states also show good agreement with the experimental data, although the observed states appear in a different order. The CB state is predicted to have a density of states concentrated along the edges of the GNR as is observed at +2.27 V, and the CB+1 state is predicted to be concentrated at the ends of the GNR. However, a state concentrated at the GNR end is experimentally seen at +2.0 V. Since the state at +2.0 V appears first, it is assigned as the GNR CB and the state at +2.27 V is the GNR CB+1 state. The alignment between the substrate lattice and the GNR may cause energetic shifts in the states as

previously observed for carbon nanotubes on InAs.[34]

The increased charge density at the GNR edges agrees with previous STM studies of straight atomically precise graphene nanoribbons and GNR heterojunctions on Au(111) where an increased LDOS at the edges was measured.[8, 9, 13, 38] The enhanced LDOS is not due to an edge state but is instead an extended state with a three-dimensional shape that has a relatively higher value of the LDOS with increased height at the outer edges of the GNR.[8] Localized edge states are seen for 4 nm wide GNRs with disordered edges,[28] unzipped carbon nanotubes,[4] and zigzag GNRs.[33]An enhanced DOS is also seen at armchair edges of graphene sheets, due to the interference of backscattering electrons.[29]

Figure 2.8 illustrates that I-V spectroscopy of GNRs on H:Si(100) must be carefully presented and analyzed. When initially investigating the electronic structure of graphene nanoribbons, log(I)-V spectra maps were used to estimate the bandgap. The normalized tunneling conductance is useful for distinguishing the density of states (DOS) of a graphene nanoribbon from the DOS of the substrate. In Figure 2.8b the same STS data is presented as a log(I)-V spectra map and does not show distinct substrate and GNR features. Decoupling of substrates and nanoribbon states is of paramount importance for bandgap determination and can be accomplished by experimentally measuring the normalized tunneling conductance and comparing it with simulations of the density of states. From equation (2) in Chapter 1, the tunneling conductance is proportional to the density of states of the sample when the density of states of the tip is constant.

The bandgap is determined to be 2.80 eV by choosing the span between the CB and VB onsets, as was done for the STS measurement of chevron GNRs on Au(111).[43] Chevron GNRs on Au(111) were shown to have a bandgap of about 2.0 eV[5, 43] with STS, 2.8 +/- 0.03 eV with HREELS,[23] and 3.1 +/- 0.4 eV with ARUPS.[23] Here an experimental measurement of the chevron GNRs on H:Si(100) reveals a 2.8 eV bandgap. The 2.8 eV bandgap measured here approaches the expected 3.6 eV intrinsic GNR bandgap predicted using the GW approximation.[21] Theoretical modeling has previously shown that the bandgap

of a graphene nanoribbon on silicon is expected to be larger than the bandgap of a graphene nanoribbon on gold due to a decreased screening interaction.[14] To confirm the reproducibility of the bandgap measurement, line spectra collected over 21 graphene nanoribbons are examined. The average bandgap is 2.85 eV with a standard deviation of 0.13 eV (Figure 2.9).

2.4 Junctions Formed by Overlapping Chevron Graphene Nanoribbons

During dry contact transfer overlapping nanoribbons are also placed on the surface allowing the study of multilayer GNRs, which have not been previously examined. While the multilayer GNR cross-junctions that were investigated in this work accidentally formed on a surface during the transfer process, the demonstrated possibility of moving GNRs on H:Si(100) with an STM tip (Figure 2.5) suggests that such and other complex GNR structures may also be formed intentionally via STM nanomanipulation. Graphene nanoribbon junctions are expected to play an important role in creating novel electronic devices, as has been predicted for in-plane graphene nanowiggle junctions.[6] Figure 2.10a shows several nanoribbons on the H:Si(100) surface. Two GNRs greater than 20 nm in length are about 15 nm apart, with a third GNR spanning them to form a junction, labeled J. To the right of the junction, there is a short single layer GNR segment that may have torn off during the DCT process.

Figure 2.10b shows the height profile along the solid line in Figure 2.10a. The single layer GNR in the center of the image is 2.9 Å taller than the silicon terrace it sits on, and the short single layer segment on the right is about 3.5 Åtaller than the nearby silicon. The junction (J) has an apparent height of 6.4 Å, which is 3.5 Å taller than the GNR beneath it, which is consistent with the expected apparent height of a two-layer GNR junction.

Figure 2.10c shows a normalized spectra map calculated numerically from the I-V spectroscopy data. The bandgap at the junction is 2.6 eV. The bandgap over

the GNR is estimated as 2.6 eV for the GNR on the left terrace and 2.8 eV for the GNR on the right terrace. The valence band for both single layer GNRs examined is at -1.4 eV, however, the conduction band shifts to a position 0.2 eV lower on the left terrace.

Multi-layer armchair GNRs are expected to have decreasing bandgaps with increasing layer number.[15] Figure 3d shows the PDOS for a two-layer GNR junction calculated by DFT. The overlapping segment has a bandgap slightly smaller than the sections of single layer GNR. The experimental measurement does not show a significant bandgap shift, which is expected given that computational modeling predicts a small bandgap shift. It should be noted that the normalized dI/dV maps collected across a GNR junction shown in Figure 2.4c,d may show a slight decrease in the GNR bandgap at a GNR junction.

2.5 Depassivating H:Si(100) underneath a GNR

Previous work on graphene nanoflakes revealed that hydrogen depassivation of a supporting H:Si(100) substrate causes graphene to take on a metallic character due to charge transfer and Si-C bond formation.[48] Figure 2.11a shows an STM topograph of a GNR on passivated silicon before hydrogen depassivation. Silicon underneath part of the nanoribbon was depassivated by holding the sample bias at 8 V while moving the tip along the path indicated by the white arrow in Figure 4b at 100 Å/s and maintaining a tunneling current of 0.1 nA. The increased height of the depassivated silicon indicates hydrogen removal and the presence of silicon dangling bonds (the local density of states of the silicon dangling bonds protrudes farther away from the surface than the local density of states corresponding to the hydrogen terminated surface).[24] The apparent height and width of the nanoribbon are reduced after nanolithography as seen in Figure 2.11b and the height profile in Figure 2.11f. The 1.5 Å height decrease of the GNR after depassivation indicates an increased coupling to the Si(100) surface. The width decrease reflects a change in the electronic structure of the nanoribbon.

Spectra were collected along the white dashed lines indicated in Figure 2.11a and Figure 2.11c. As shown in the normalized dI/dV maps presented in Figure 2.11d and Figure 2.11e the GNR bandgap is 2.9 eV before depassivation. The metallic behavior seen after depassivation is attributed to Si-C bonding that modifies the GNR electronic structure.[48] While individual Si(100) dangling bonds are metallic, multiple neighboring dangling bonds are semiconducting, indicating that the GNR and not the Si(100) causes the observed metallic behavior.[49] To explain the electronic changes of the GNR on Si(100) after hydrogen depassivation, we performed DFT simulations to examine the geometry and charge distribution of a GNR on a Si(100) surface before and after hydrogen depassivation. We also show the PDOS of the GNR in Figure 2.11g. After hydrogen depassivation, the PDOS of the GNR shows finite states at the Fermi level and there is no longer a bandgap. The dangling bonds at the silicon surface interact with the pz orbitals of the GNR to form covalent bonds modifying the electronic structure of the GNR and leading to metallic behavior. Figure 2.11h and Figure 2.11i show the geometry and normalized charge distribution of the GNR on H:Si(100) and Si(100). Before hydrogen depassivation the GNR is flat above the substrate, and there is no charge density overlap between graphene and H:Si(100). However, after hydrogen depassivation, we see both the geometry and charge distribution change. The surface Si atoms move outward while the GNR above is distorted and some of the C atoms move inward to the Si surface. The corresponding charge density is strongly localized and there is some overlap between the GNR and silicon charge densities.

2.6 Conclusion

Dry contact transfer enables high-resolution STM imaging and spectroscopy of solution-synthesized atomically precise chevron graphene nanoribbons on technologically relevant substrates such as the H:Si(100)2x1 surface. This method overcomes challenges associated with solvent residue, and is very promising for

studies of other atomically precise solution-synthesized nanomaterials. One of the key insights from the study was that the nanoribbons are thin enough that tunneling to the substrate plays a significant role in STS measurements and must be carefully considered to determine the bandgap of GNRs. Future work using smaller bandgap GNRs and larger bandgap substrates may avoid this challenge. Through the use of normalized dI/dV images and LDOS simulations, the bandgap of chevron GNRs on H:Si(100) is determined to be 2.85 eV. The ability to cleanly place atomically precise GNRs onto H:Si(100) is unprecedented, and is expected to have an enormous impact on GNR device prototyping.

2.7 Methods

2.7.1 Synthesis of GNRs

Atomically precise chevron GNRs were made in solution by Yamamoto coupling of pre-synthesized 6,11-dibromo-1,2,3,4-tetraphenyltriphenylene ($C_{42}Br_2H_{26}$) followed by oxidative cyclodehydrogenation of the resulting polymer via Scholl reaction. The synthesis results in a black solid that is filtered and washed to obtain a graphene nanoribbon powder. The synthetic details and materials characterization of solution-synthesized chevron GNRs can be found in previous works.[44, 46]

2.7.2 Substrate preparation

H:Si(100) is prepared by degassing a Si(100) substrate at 600 °C for 8-16 hours, flashing at 1200 °C for 5-30 seconds several times, and holding the sample at 377 °C during exposure to 1200 L of atomic hydrogen. During the 1200 °C flash the chamber pressure is monitored, and the flash is stopped early if the pressure exceeds 1 x 10^{-8} Torr to avoid surface roughening. The silicon wafers used are Sb-doped Montco n-Si(100) (sheet resistance 5-20 mΩ-cm) and B-doped Montco p-Si(100) (sheet resistance .01-.02 Ω-cm). After passivation, the sample is cooled,

and surface cleanliness is confirmed with STM imaging.

2.7.3 STM experiments

STM imaging was performed with a home-built Lyding style STM[25] operating under ultrahigh vacuum (base pressure 3 x 10^{-11} Torr). Imaging is performed under constant current mode at room temperature (sample bias -2V, tunneling current 10 pA). Iridium coated field-directed sputter sharpened tungsten probes from Tiptek, and etched platinum-iridium tips were used for STS and STM imaging experiments. Images were also collected with etched tungsten probes. Scanning Tunneling Spectroscopy (STS) is collected in variable spacing mode (dS = 2 Å), with an initial set-point tunneling current of 100 pA. To convert to constant spacing STS data, the raw data is scaled by an exponential factor to account for the change in current due to change in tip-sample separation.[35] Hydrogen depassivation lithography is performed by moving the tip at 100 Å / second while maintaining a sample bias of 8V and a tunneling current of 0.1 nA.

2.7.4 DCT Applicator Preparation

Fiberglass tubing is cleaned by sonicating sequentially in detergent/water, acetone, and IPA. The fiber is dried using nitrogen and then mounted onto a sample holder. The tubing is gently frayed with a razor blade. Then the applicator is pressed against the graphene nanoribbon powder, and nitrogen gas is gently passed over the applicator to remove any loosely attached material. The applicator is then loaded into the UHV chamber and degassed overnight, typically under the same condition used for an STM tip degas – ˜300-500 °C. Nanoribbons are exfoliated onto the silicon surface by pressing the fiberglass applicator against the sample repeatedly until GNRs are found on the surface.

2.7.5 Computational Modeling

Density Functional Theory calculations for a 6-unit cell GNR were performed with Quantum Espresso package,[10] with a supercell arranged to separate GNR and its images. Norm-conserving pseudopotentials with the Perdew-Burke-Ernzerhof (PBE) exchange-correlation functional[30] were employed, with a planewave energy cut-off of 100 Ry. A Monkhorst-Pack grid of 1 x 1 x 1 was used for structural relaxations and 2 x 2 x 1 for electronic property calculations. The structures were relaxed until the maximum residual force was smaller than 0.05 eV/Å. For the systems of GNR on hydrogen passivated and depassivated silicon surface, due to the lattice mismatch, a GNR supercell of two unit cells was placed upon the substrate with 5 layers of silicon atoms. Tensile and compressive strain were applied to the GNR and silicon substrate respectively, whose magnitudes were all less than 1% to ensure the electronic properties of the systems were not altered too much. The Grimme-D2 van der Waals corrections[11] were used to describe the interaction between the GNR and the substrate. The structures were also relaxed with a Monkhorst-Pack grid of 1 x 1 x 1 until the maximum residual force was smaller than 0.05 eV/Å. Then the PDOS and charge distribution were calculated with a Monkhorst-Pack grid of 2 x 1 x 1. The visualization of geometries and LDOS was performed with XCrysDen.[18] The DFT and GW band structures for a GNR of infinite length with periodic boundary condition were calculated using the VASP package[19, 20] within the Perdew-Burke-Ernzerhof (PBE) exchange-correlation functional.[30] The projector augmented wave (PAW) pseudopotentials with a 400 eV energy cutoff were used. The Gamma-point-centered k-point of 4 x 1 x 1 was applied for structural relaxation and band structure calculations. The structure was relaxed until the maximum residual force was less than 0.01 eV/Å. Starting from DFT ground state, quasiparticle energies were calculated using the single-shot G0W0 approximation[37] implemented in VASP. Concerning the memory requirement and computational time, the key parameters of NBANDS=512, ENCUT=400, ENCUTGW=80 and NOMEGA=36 were used to conduct the GW

simulation. These parameter settings were similar to those listed in a previous study.[22]

2.8 Figures

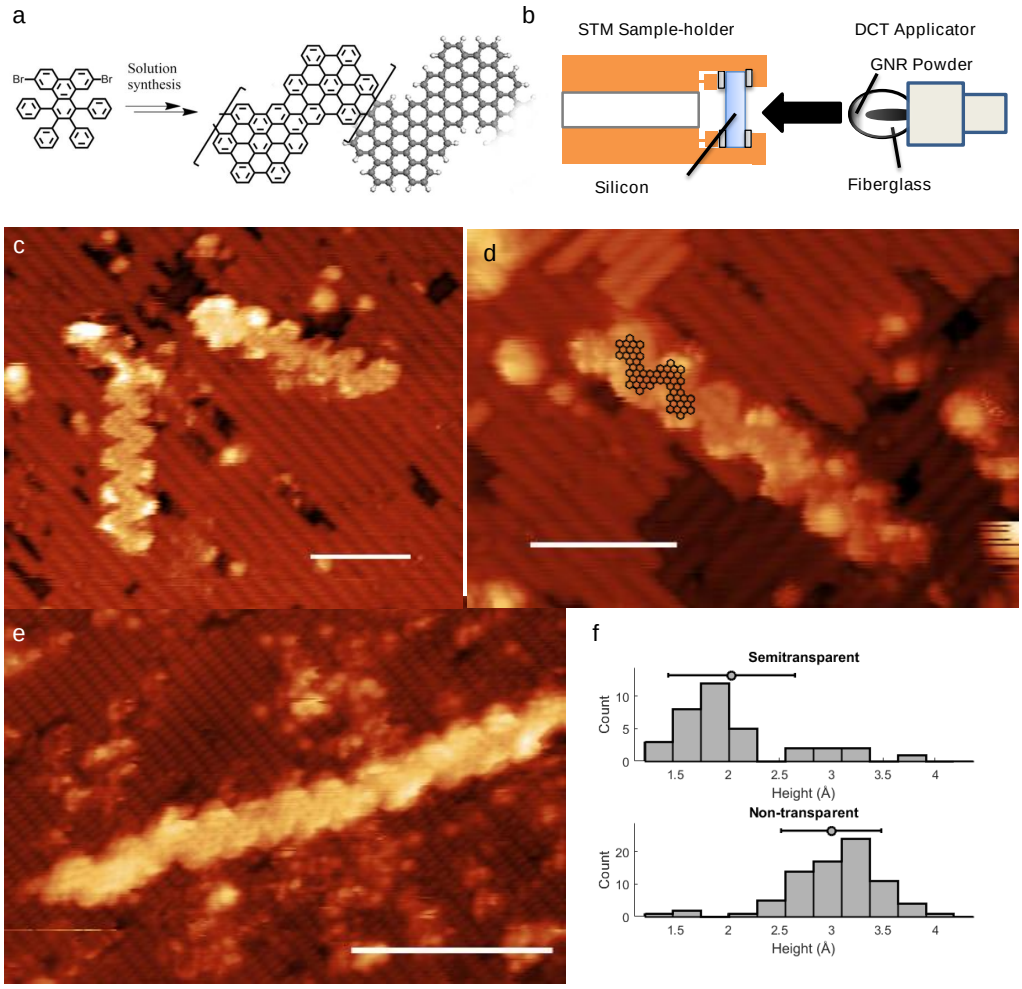

Figure 2.1: Scanning tunneling microscopy (STM) images of graphene nanoribbons (GNRs) on H:Si(100) sample bias: -2V tunneling current: 10pA (a) Schematic showing precursor used for solution synthesis of chevron GNRs; see ref.[44] for the detailed synthetic procedure. (b) Sketch of dry contact transfer method used to exfoliate GNRs onto H:Si(100) (c,d) Graphene nanoribbon transparency – the silicon substrate is visible through the graphene nanoribbon. Scalebar is 5 nm (e) Image showing intraribbon resolution corresponding to the graphene lattice. Scalebar is 5 nm. Tunneling current is 100 pA (f) Histograms of semitransparent and non-transparent GNR heights.

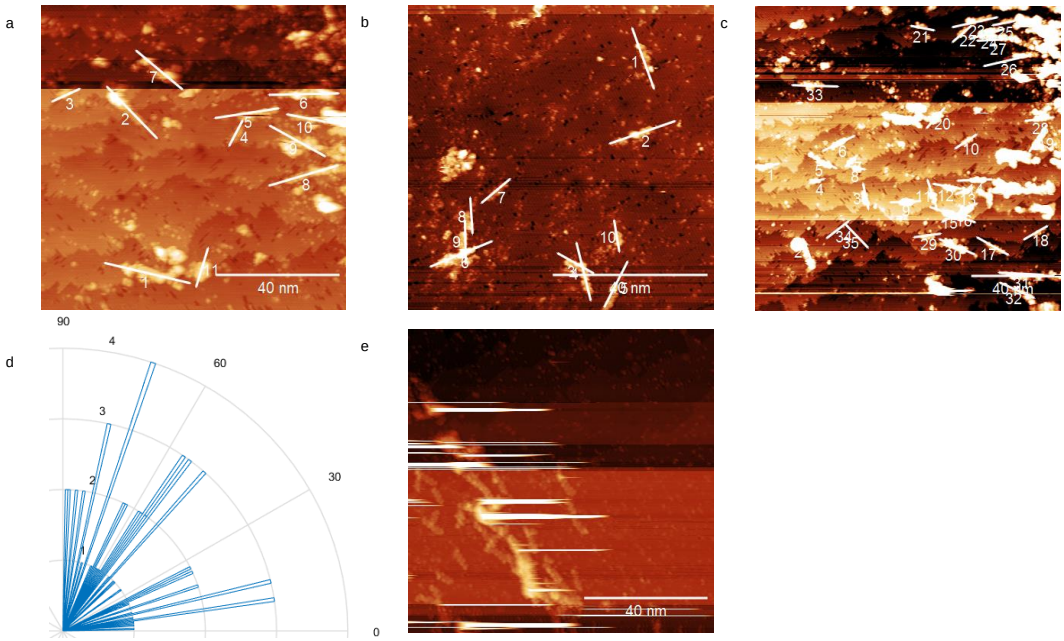

Figure 2.2: (a-c) STM images showing 64 graphene nanoribbons with solid lines indicating the nanoribbon longitudinal axis directions. When the longitudinal axis of the graphene nanoribbon is parallel to the silicon dimer row direction, the relative angle is 0 degrees, and when the longitudinal axis of the graphene nanoribbon is perpendicular to the dimer row direction, the relative angle is 90 degrees. (d) Histogram showing the measured orientations of chevron GNRs relative to the silicon dimer rows. Although fewer ribbons were found oriented at 45 degrees relative to the dimer row direction, no claims are made about GNR-substrate alignment because the motion of the applicator is not well-controlled and may play a role in causing the GNRs to align to a particular orientation. (e) Additional STM topograph showing several graphene nanoribbons with correlated orientations. The movement of the applicator may align the GNRs on the surface independently of substrate-GNR interactions.

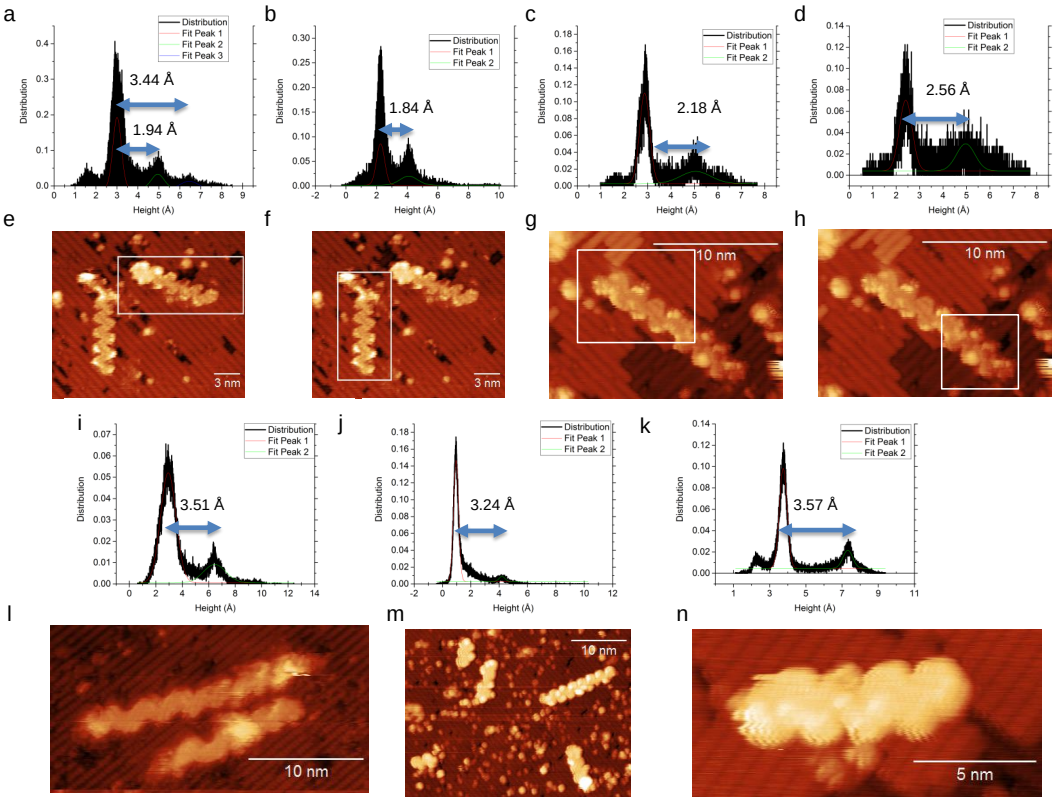

Figure 2.3: (a-d) Height distributions of semitransparent graphene nanoribbons showing a height of 1.84 – 2.56 Å (e-h) STM topographs with white rectangles indicating regions used to generate height distributions in (a-d). (i-k) Height distributions for non-transparent graphene nanoribbons, showing heights of 3.24 Å – 3.57 Å. (l-n) The topographs used to generate the height maps in i-k. These ribbons do not show semitransparency, and several GNRs are simultaneously examined. The GNR height is determined as the difference between the substrate and GNR peak centers. In some cases, the peak position is determined using a Gaussian fit, as illustrated above, but in many cases the peak position is estimated. Images with artifacts or where the substrate near the GNR is not clearly imaged are excluded. The topographs used to generate Figure 2.1f includes STM images collected at +2V, -2V, and -1.5V. The tunneling current ranges from 10 pA to 1000 pA, with most of the data collected at 10 or 100 pA. The height difference observed is greater than what has been previously seen for semitransparent graphene, possibly due to the narrow lateral dimensions and nanowiggles of the GNR enabling additional pliability.[12] The height distribution for a nanoribbon that shows both semitransparency and non-transparency is shown in (a) and the corresponding topograph is shown in (e). There is a 1.5 Å height difference between the semitransparent and non-transparent portion of the same nanoribbon. In this case, there is no evidence of a change in the configuration of the probe, so the semitransparency may be influenced by buckling of the nanoribbon, which depends on a lattice mismatch between graphene and the H:Si(100)2x1 surface or defects on the substrate.

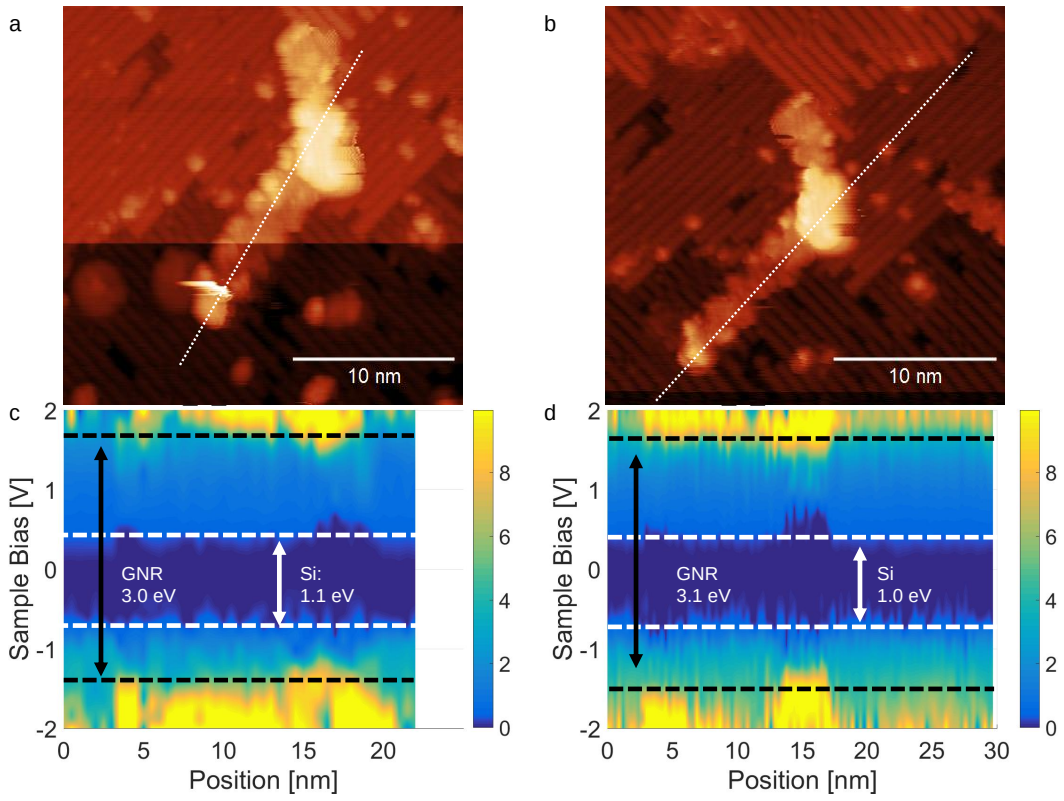

Figure 2.4: (a-b) STM topographs of graphene nanoribbons on H:Si(100). Sample bias: -2V; tunneling current: 10 pA. In (a) the lower graphene nanoribbon appears non-transparent. In (b) the same graphene nanoribbon appears semitransparent, with the corrugation of the silicon dimer rows visible underneath the graphene nanoribbon. The STM images shown in (a) and (b) demonstrate that the same nanoribbon can exhibit both semitransparency and non-transparency. A previous study determined that the tip pushing the GNR closer to the surface can cause the semi-transparency effect.[12] The dashed lines indicate positions where scanning tunneling spectroscopy was collected (c-d) Normalized dI/dV spectra maps collected along dashed lines indicated in (a,b). The positions of the silicon and GNR valence and conduction band edges are indicated by dashed lines. The bandgap of the GNR is comparable in both cases.

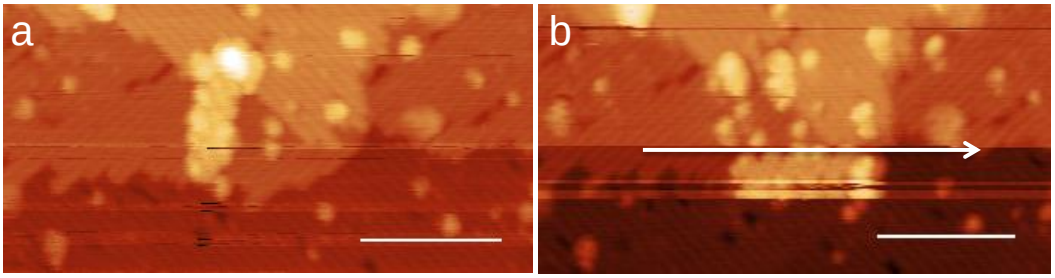

Figure 2.5: The scanning tunneling microscope was used to change the position and orientation of graphene nanoribbons. A graphene nanoribbon before and after nanomanipulation. Sample bias: -2V; tunneling current: 10 pA. Scale bar is 10 nm (a) Graphene nanoribbon on H:Si(100) surface (b) The tip is moved 4 Å closer to the surface and moved from left to right along the indicated white arrow. The feedback loop is off and the sample bias is held at -2 V. The ribbon is rotated by 80 degrees and translated several nanometers. The weak interaction between the H:Si(100) surface and GNRs allows the nanoribbons to be pushed with the STM probe. The STM tip traces a height contour obtained from a previously collected topograph. As the tip travels along its predefined path, the tip is displaced an additional 5-9 Å closer to the surface. The sample bias is typically held at 0 V while the feedback loop is turned off.

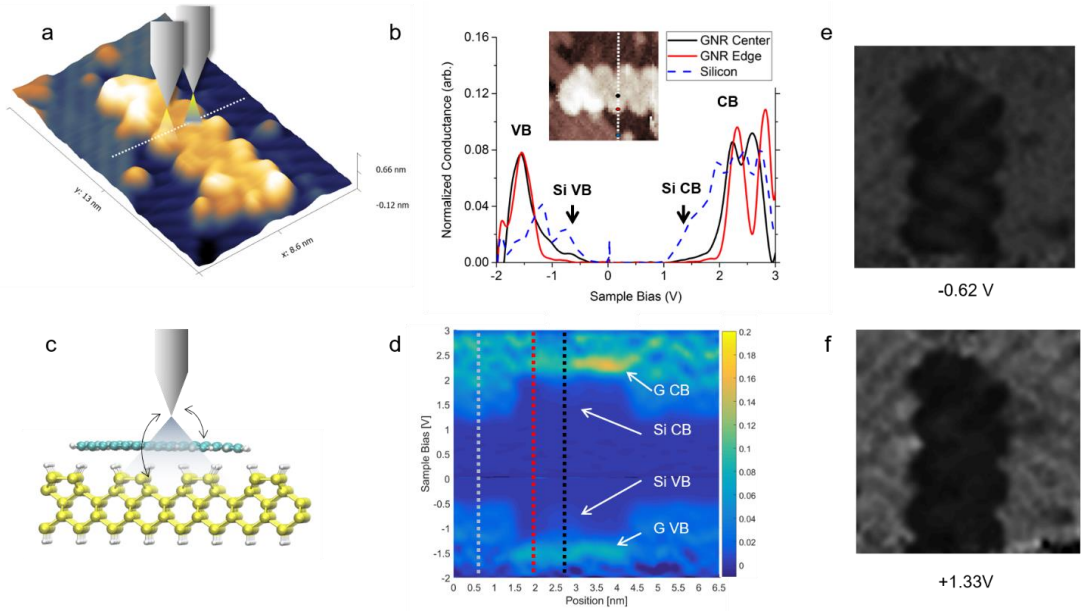

Figure 2.6: (a)Topograph of graphene nanoribbon, and (b) normalized conductance collected over the silicon, the edge of the graphene nanoribbon, and the center of the graphene nanoribbon. (c) Schematic indicating contributions to the tunneling current from both the substrate and the GNR, and (d) normalized conductance map corresponding to the dashed line in (a). The dashed vertical lines correspond to the traces plotted in (b). Arrows indicate silicon and graphene states. (e,f) Normalized dI/dV maps at sample biases corresponding to the energies of the silicon states. The GNRs appear darker than the surrounding silicon due to their decreased density of states. There is a modulation of the density of states collected over the GNRs that is commensurate with the silicon lattice, supporting the claim of substrate contribution to the spectroscopy measurement.

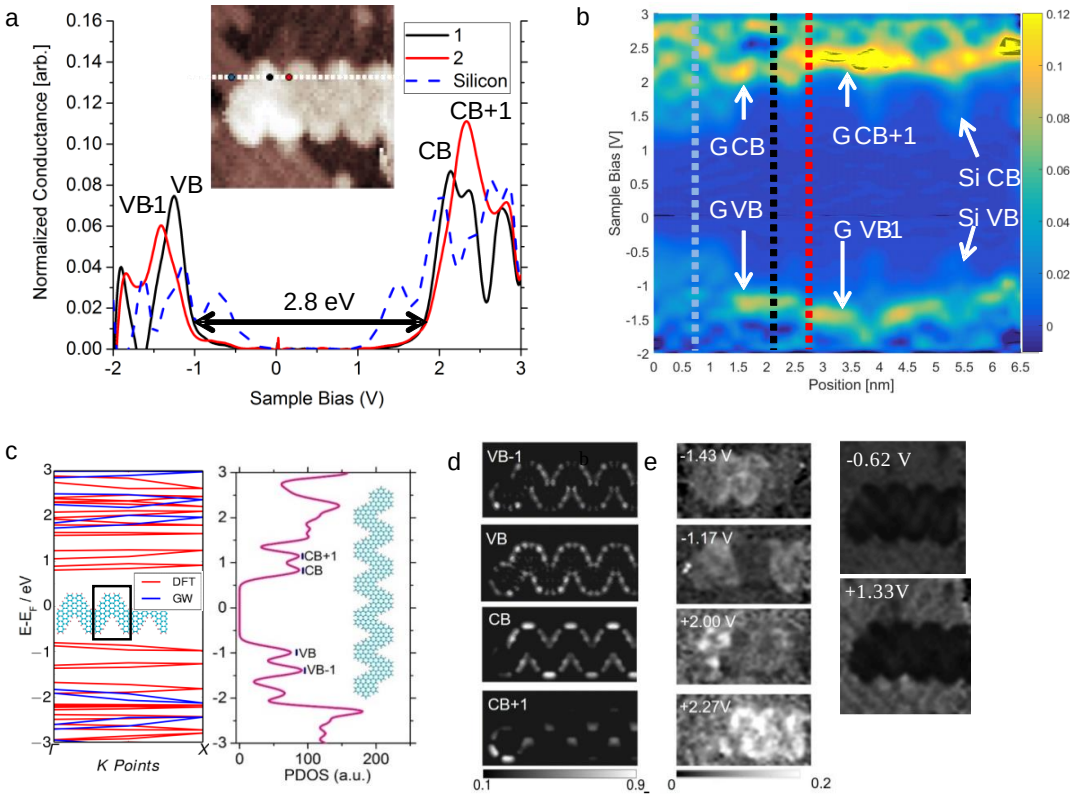

Figure 2.7: STS and CITS of graphene nanoribbon. Current imaging tunneling spectroscopy was collected over an array of 50 x 50 points spanning 6.5 x 6.5 nm^2. The normalized tunneling conductance dI/dV / (I/V) was numerically calculated and portions of the data are shown here. (a) Normalized tunneling conductance at the GNR center, the GNR edge, and over the silicon substrate. The inset shows a topograph of the GNR studied. (b) Normalized tunneling conductance spectra map across the length of the GNR, corresponding to positions along the dashed white lines in the inset of (a). The black, blue, and red dashed lines indicate the positions of the spectra points shown in (a). The conduction and valence bands for the graphene and silicon are indicated. (c) Left: the band structure obtained from both DFT and GW for an infinite GNR with periodic boundary condition (the inset shows the unit cell as incorporated in the black rectangle). The band energies were shifted so that the Fermi level was located at the mid-gap position. Right: the projected density of states (PDOS) for an isolated 6-unit cell GNR (atomic structure shown in inset, cyan atoms for C and red atoms for H) computed using DFT, four states VB-1, VB, CB+1, and CB are marked at the corresponding peaks, the window is set to be 0.1 eV to be consistent with the resolution of room temperature STM experiments. (d) DFT-simulated normalized LDOS maps of the VB-1, VB, CB, and CB +1 states at 4 Å above the GNR plane, the color range of [0.1, 0.9] is used to show features more clearly. (g) Normalized dI/dV maps at energies corresponding to the bands indicated in (b).

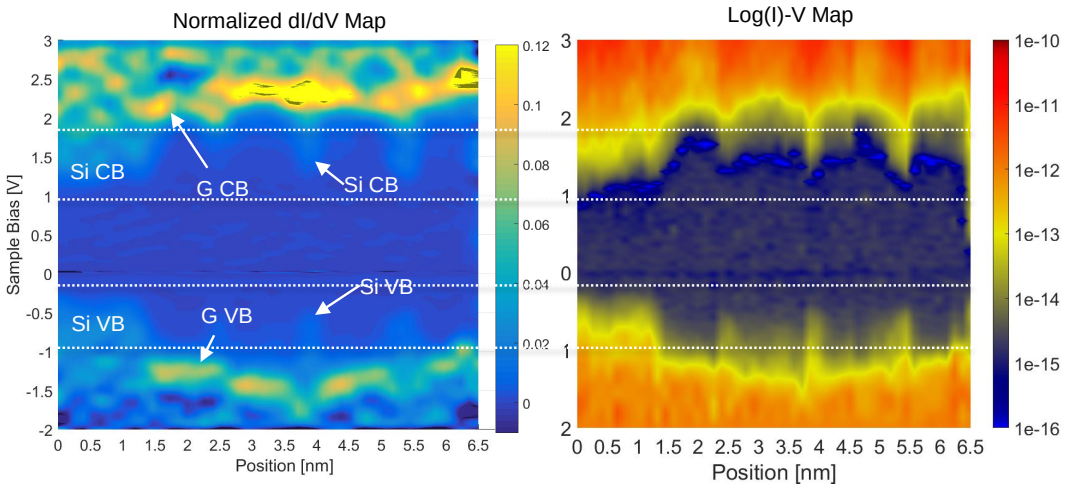

Figure 2.8: Comparison of the normalized dI/dV plot in Figure 2.7 and the corresponding log(I)-V map. The log(I)-V map does not properly capture the GNR band edges, and the normalized dI/dV map should be used to determine the GNR bandgap.

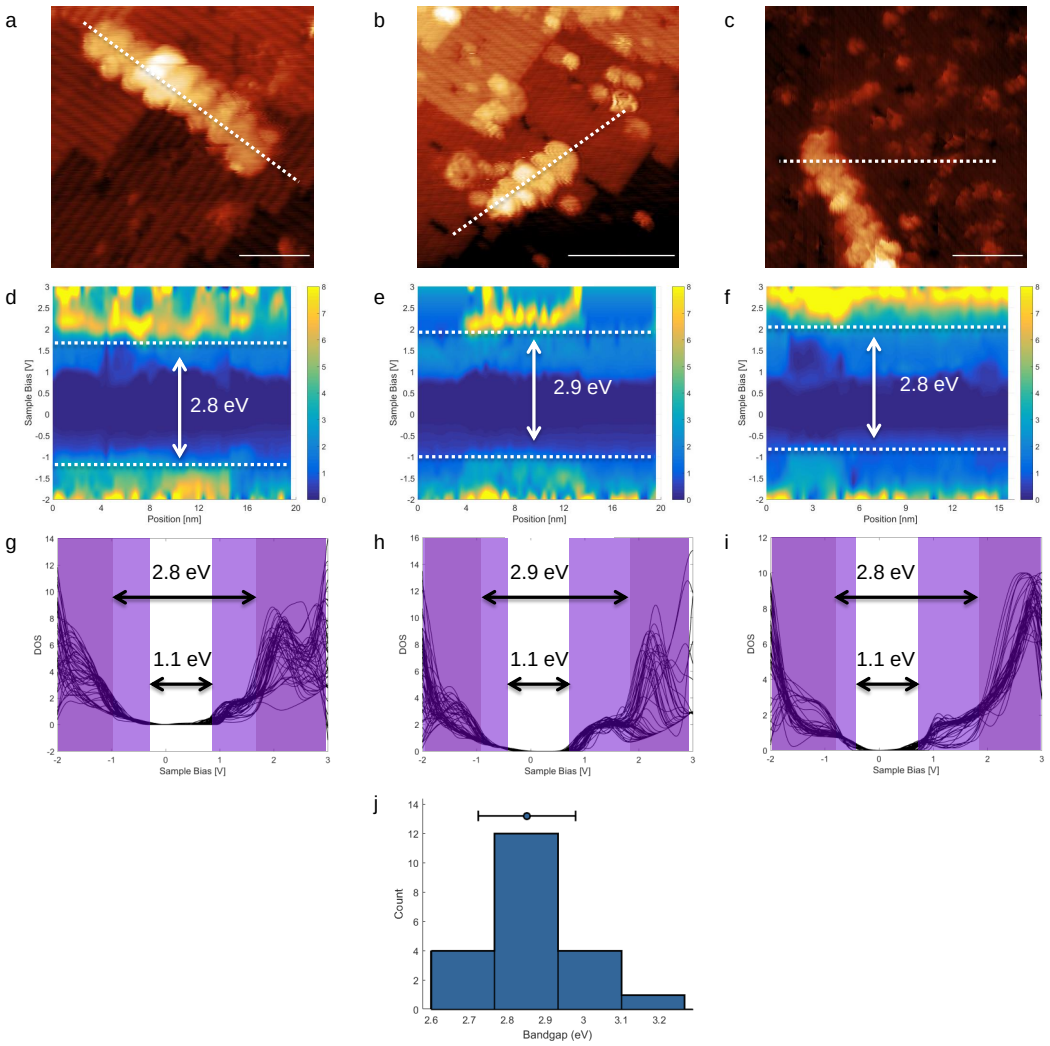

Figure 2.9: Density of states maps used to determine GNR bandgaps. (a-c) STM topographs of graphene nanoribbons on H:Si(100). Scalebars are 5 nm. The dashed lines indicate positions where variable spacing I-V spectroscopy was collected (d-f) Normalized dI/dV spectra maps across GNRs. The positions of the GNR valance and conduction band edges are indicated by dashed lines. (g-i) Normalized dI/dV plots showing data used to generate the maps shown in d-f. The GNR and Si bandgaps are indicated. (j) Histogram plotting the bandgaps of 21 GNRs measured. The average bandgap is found to be 2.85 +/- 0.13 eV.

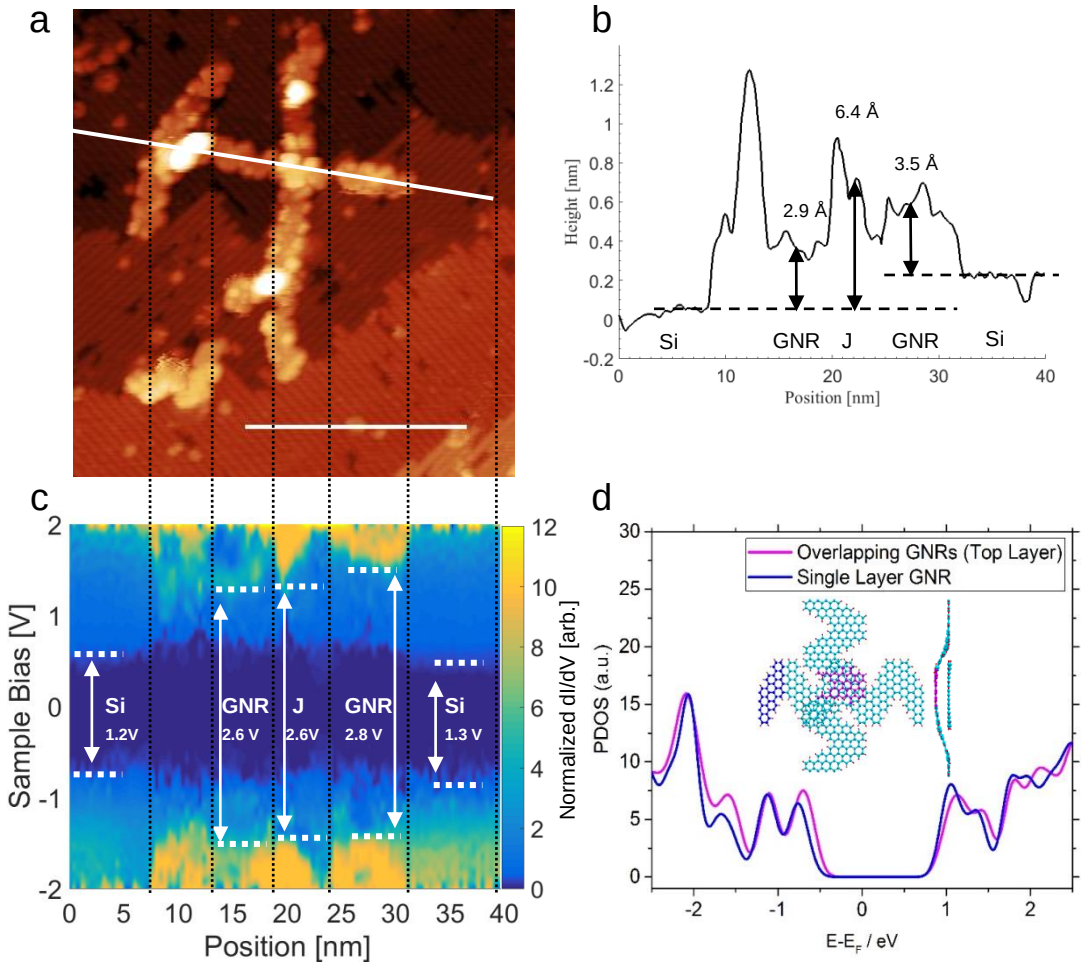

Figure 2.10: Scanning tunneling spectroscopy (STS) of nanoribbon junctions (a) STM topograph showing several overlapping graphene nanoribbons. Sample bias -2V tunneling current 10 pA. Scalebar length is 20 nm. (b) Height profile along solid line in (a). The height of the GNR relative to the surrounding H:Si(100) is 2.9-3.5 Å. The junction appears to be 3-3.5 Å taller than the single layer GNRs (c) Spectra map taken along the solid line indicated in a. The regions are labeled Si- H:Si(100) substrate, GNR – graphene nanoribbon, and J – the graphene nanoribbon junction (d) DFT-calculated PDOS for overlapping GNR (top layer) and single layer GNR, whose atomic structure is shown in the inset. The atoms in the single layer part are colored blue while those in the overlapping region are colored pink.

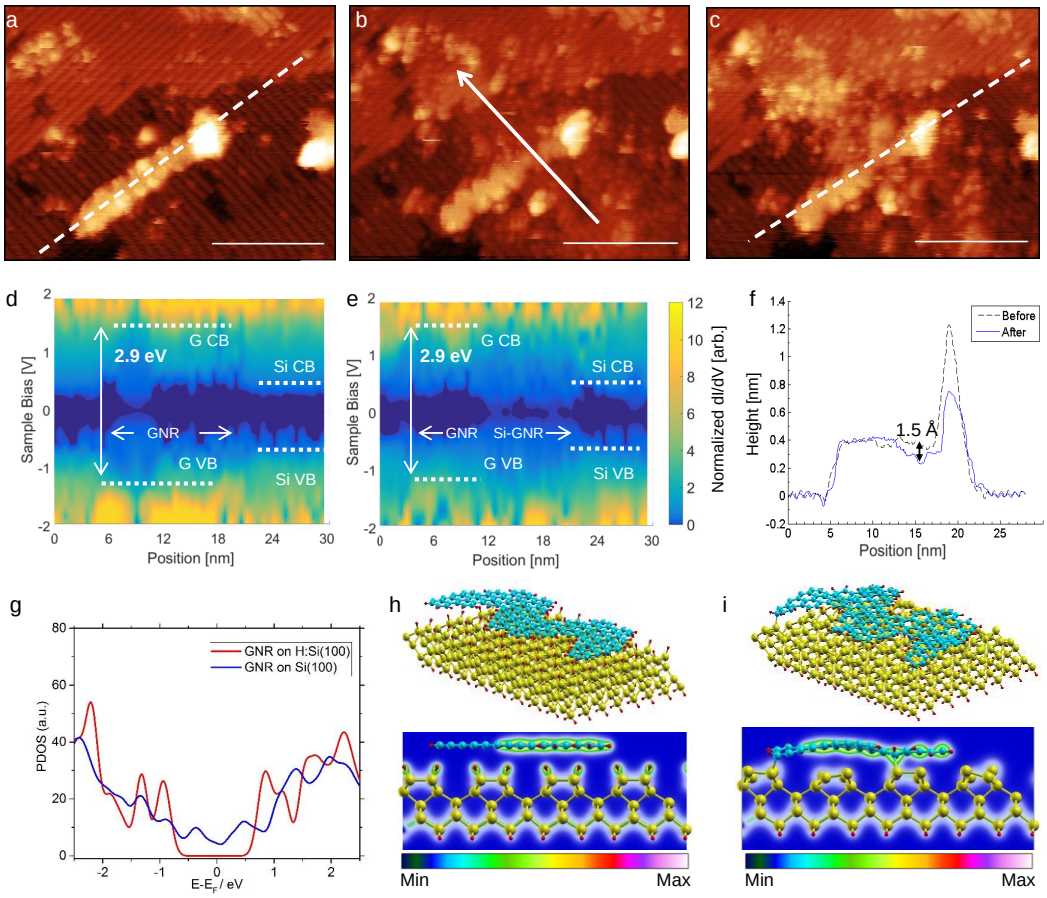

Figure 2.11: Hydrogen depassivation underneath a GNR (a) STM image of a GNR on H:Si(100). (b) Nanoribbon after hydrogen depassivation lithography. The tip was moved along indicated arrow with a sample bias of +8 V, tunneling current 0.1 nA, and a tip speed of 100 Å/s. The depassivated region appears taller than the surrounding H:Si(100) due to the increased spatial extent of the Si dangling bonds. (c) STM image collected along with STS over the dashed line. Images collected at -2V 10 pA. All scale bars are 10 nm (d,e) Normalized dI/dV maps corresponding to the spectroscopy collected in (a,c). (f) Height profiles along dashed lines in (a) and (c) to show height changes along GNR after depassivation. (g) Simulated PDOS for GNR on H:Si(100) and Si(100) respectively. (h,i) Atomic structures and normalized charge density contour plots for GNR on H:Si(100) and Si(100) shown to visualize the interactions between GNR and the substrate. The cyan, red and yellow atoms are for C, H and Si, respectively.

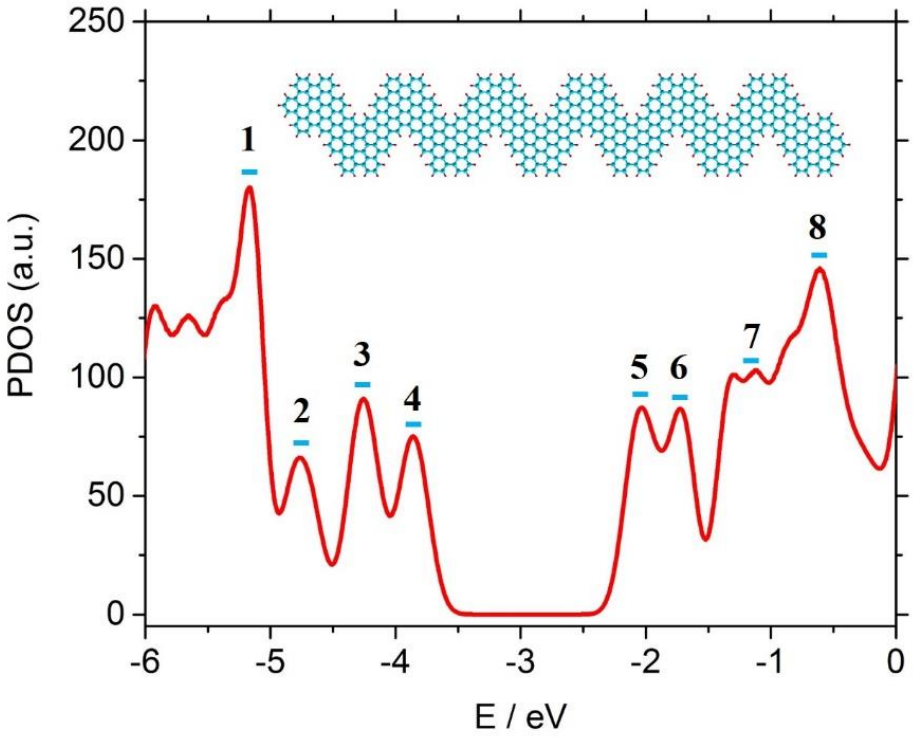

Figure 2.12: Projected density of states for a six-unit cell GNR. Inset shows the structure of the modeled GNR. No substrate is included. States 1-8 are labeled and mapped onto spatial coordinates in Figure 2.13. Two valence states and two conduction states were indicated in Figure 2.7e and the corresponding normalized LDOS at 4 Å above GNR plane were calculated and compared with the normalized dI/dV images from experiments. Here, more states near the Fermi level are indicated and the corresponding normalized LDOS at different heights above GNR plane are shown. Figure 2.13 shows the DFT calculated PDOS of the isolated 6-monomer GNR with the states marked out using indices from 1 to 8. The PDOS from DFT shows the bandgap to be ˜1.6 eV, which is much smaller than the true quasi-particle bandgap of ˜3.6 eV.

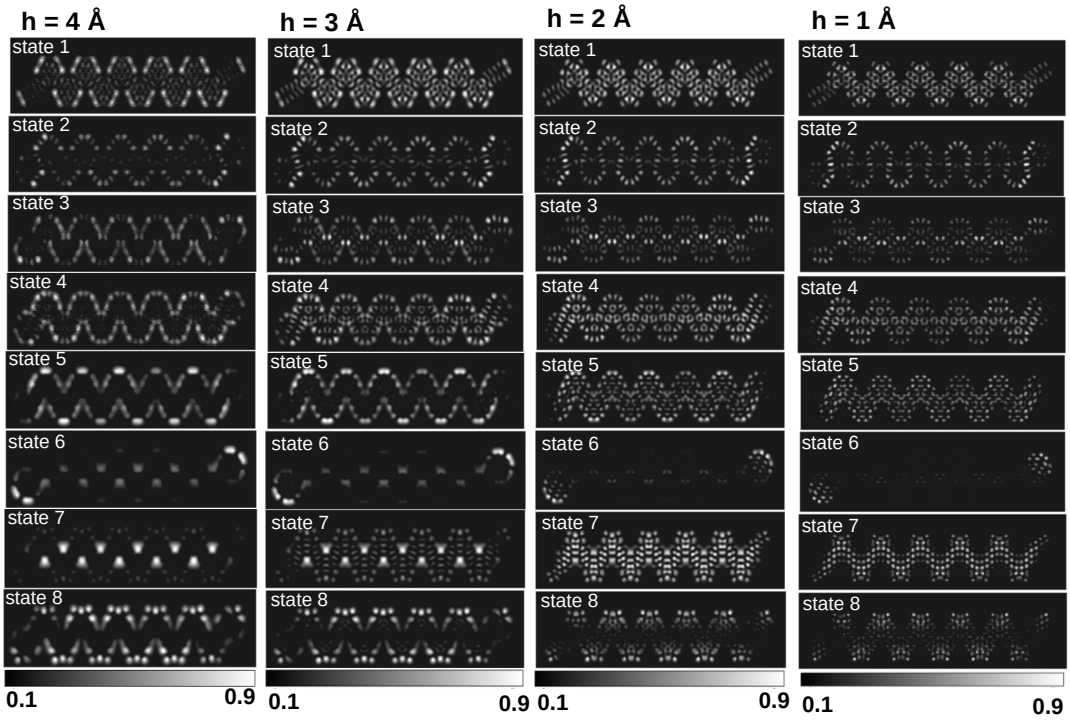

Figure 2.13: Simulated local density of states of a six-unit cell chevron GNR is plotted at heights of 4 Å to 1 Å above the GNR plane. The color range is set to be [0.1, 0.9] to more clearly reveal the features.

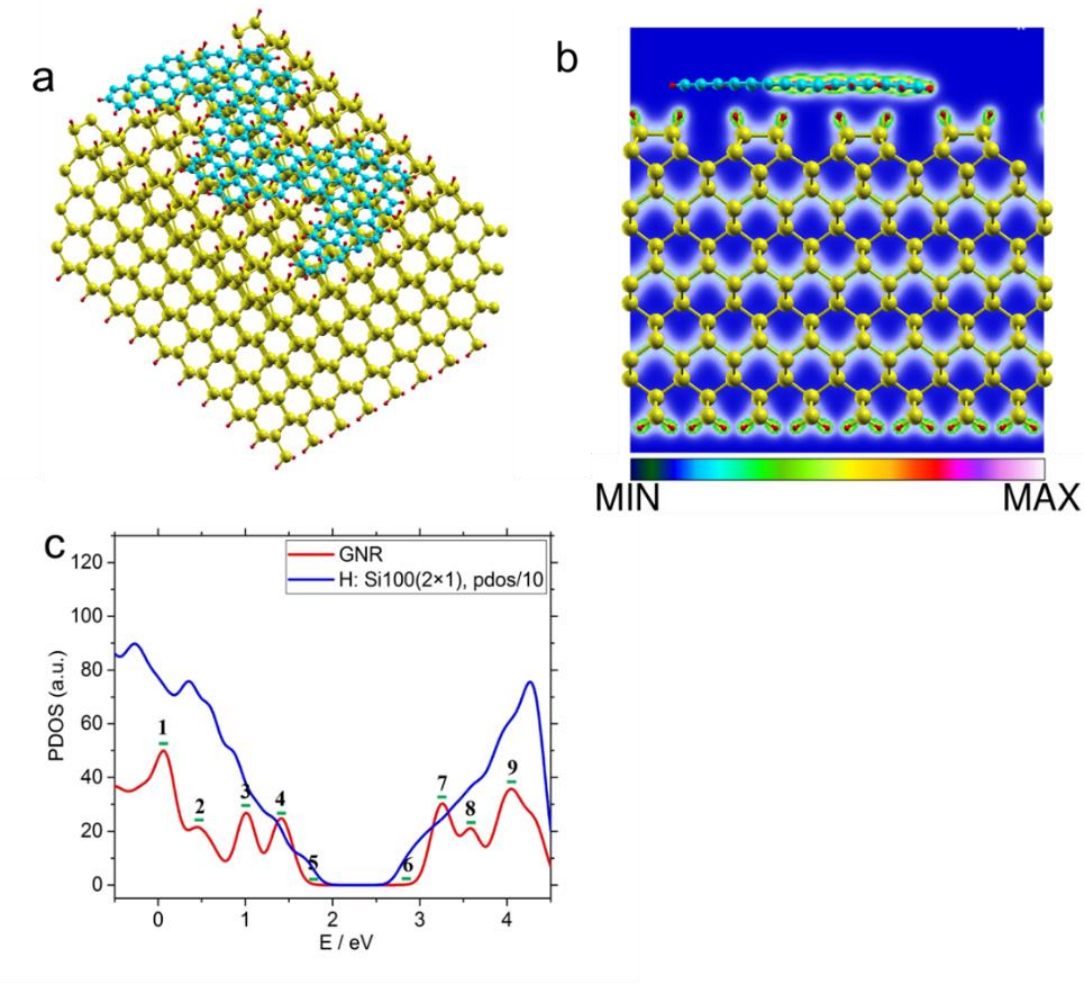

Figure 2.14: The experimental results show the influence of the silicon substrate on the GNR. Here simulations are performed to show the change of the GNR LDOS once it is placed on the H:Si(100) substrate. Periodic boundary conditions are applied to obtain the PDOS for an infinite GNR on H:Si(100) (a) Model showing chevron GNR on H:Si(100) slab. The atomic structure is shown with 16 layers of silicon included in the substrate to capture the bulk silicon bandgap (b) Cross-sectional view showing the atomic structure and normalized charge distribution of GNR relaxed on the H:Si(100) surface. (c) PDOS plot of GNR and H:Si(100). The silicon slab has a Kohn-Sham bandgap of ˜1.2 eV, which is the same as its bulk value.

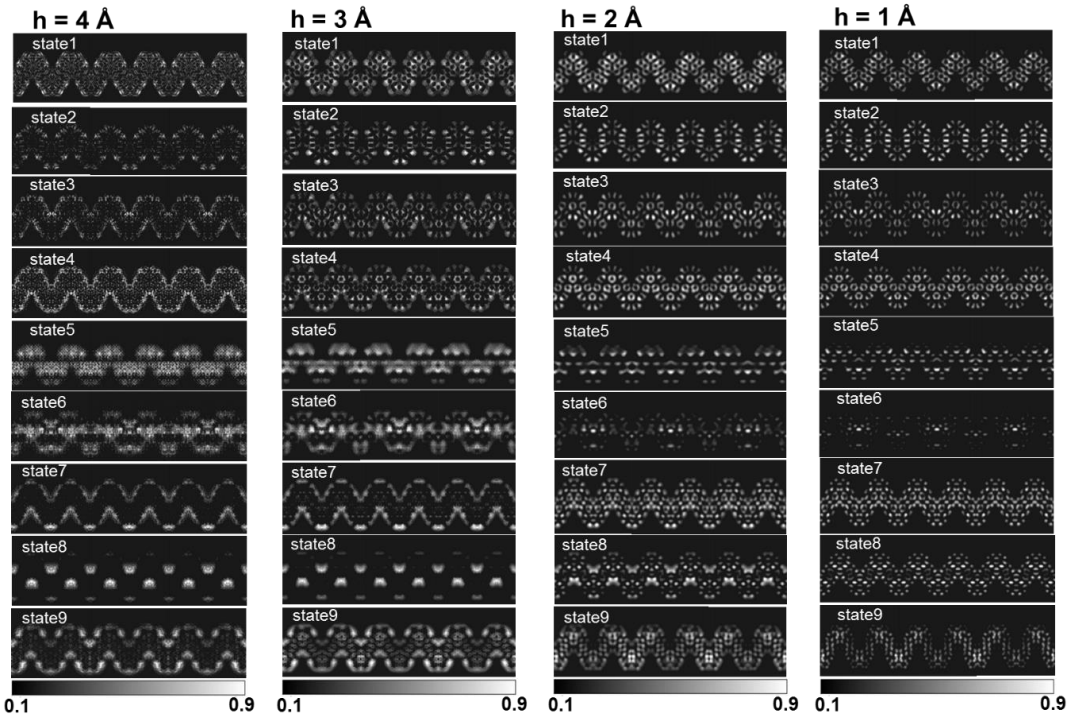

Figure 2.15: Simulated local density of states (LDOS) for an infinite chevron GNR on H:Si(100) plotted at heights from 4 to 1 Å above the GNR plane. The states are chosen at energies corresponding to peaks of the GNR PDOS and the corresponding normalized LDOS at different heights above GNR plane are shown. Since the bandgap of the silicon substrate is smaller than that of the GNR on top, some features seen in the normalized LDOS within the bandgap of the GNR (State 5 and State 6) are caused by the LDOS of silicon. For other states, there are small signatures shown in the normalized LDOS of GNR, which are also attributed to silicon DOS.

2.9 References

[1] P. M. Albrecht and J. W. Lyding. Ultrahigh-vacuum scanning tunneling microscopy and spectroscopy of single-walled carbon nanotubes on hydrogen-passivated si(100) surfaces. *Applied Physics Letters*, 83(24):5029, 2003.

[2] Patrick B. Bennett, Zahra Pedramrazi, Ali Madani, Yen-Chia Chen, Dimas G. de Oteyza, Chen Chen, Felix R. Fischer, Michael F. Crommie, and Jeffrey Bokor. Bottom-up graphene nanoribbon field-effect transistors. *Applied Physics Letters*, 103(25):253114, 2013.

[3] C. Bronner, S. Stremlau, M. Gille, F. Brausse, A. Haase, S. Hecht, and

P. Tegeder. Aligning the band gap of graphene nanoribbons by monomer doping. *Angew Chem Int Ed Engl*, 52(16):4422–5, 2013.

[4] J. Cai, P. Ruffieux, R. Jaafar, M. Bieri, T. Braun, S. Blankenburg, M. Muoth, A. P. Seitsonen, M. Saleh, X. Feng, K. Mullen, and R. Fasel. Atomically precise bottom-up fabrication of graphene nanoribbons. *Nature*, 466(7305):470–3, 2010.

[5] Jinming Cai, Carlo A Pignedoli, Leopold Talirz, Pascal Ruffieux, Hajo Söde, Liangbo Liang, Vincent Meunier, Reinhard Berger, Rongjin Li, and Xinliang Feng. Graphene nanoribbon heterojunctions. *Nature Nanotechnol*, 9(11):896–900, 2014.

[6] Tyler Cary, Eduardo Costa Girão, and Vincent Meunier. Electronic properties of three-terminal graphitic nanowiggles. *Physical Review B*, 90(11):115409, 2014.

[7] Chih-Chieh Chen and Yia-Chung Chang. Theoretical studies of graphene nanoribbon quantum dot qubits. *Physical Review B*, 92(24), 2015.

[8] Y. C. Chen, T. Cao, C. Chen, Z. Pedramrazi, D. Haberer, D. G. de Oteyza, F. R. Fischer, S. G. Louie, and M. F. Crommie. Molecular bandgap engineering of bottom-up synthesized graphene nanoribbon heterojunctions. *Nat Nanotechnol*, 10(2):156–60, 2015.

[9] Y. C. Chen, D. G. de Oteyza, Z. Pedramrazi, C. Chen, F. R. Fischer, and M. F. Crommie. Tuning the band gap of graphene nanoribbons synthesized from molecular precursors. *ACS Nano*, 7(7):6123–8, 2013.

[10] P. Giannozzi, S. Baroni, N. Bonini, M. Calandra, R. Car, C. Cavazzoni, D. Ceresoli, G. L. Chiarotti, M. Cococcioni, I. Dabo, A. Dal Corso, S. de Gironcoli, S. Fabris, G. Fratesi, R. Gebauer, U. Gerstmann, C. Gougoussis, A. Kokalj, M. Lazzeri, L. Martin-Samos, N. Marzari, F. Mauri, R. Mazzarello, S. Paolini, A. Pasquarello, L. Paulatto, C. Sbraccia, S. Scandolo, G. Sclauzero, A. P. Seitsonen, A. Smogunov, P. Umari, and R. M. Wentzcovitch. Quantum espresso: a modular and open-source software project for quantum simulations of materials. *J Phys Condens Matter*, 21(39):395502, 2009.

[11] Stefan Grimme. Semiempirical ggatype density functional constructed with a longrange dispersion correction. *Journal of computational chemistry*, 27(15):1787–1799, 2006.

[12] Kevin T. He, Justin C. Koepke, Salvador Barraza-Lopez, and Joseph W. Lyding. Separation-dependent electronic transparency of monolayer graphene membranes on iiiv semiconductor substrates. *Nano Lett*, 10(9):3446–3452, 2010.

[13] R. M. Jacobberger, B. Kiraly, M. Fortin-Deschenes, P. L. Levesque, K. M. McElhinny, G. J. Brady, R. Rojas Delgado, S. Singha Roy, A. Mannix, M. G. Lagally, P. G. Evans, P. Desjardins, R. Martel, M. C. Hersam, N. P. Guisinger, and M. S. Arnold. Direct oriented growth of armchair graphene nanoribbons on germanium. *Nat Commun*, 6:8006, 2015.

[14] N. Kharche and V. Meunier. Width and crystal orientation dependent band gap renormalization in substrate-supported graphene nanoribbons. *J Phys Chem Lett*, 7(8):1526–33, 2016.

[15] Neerav Kharche, Yu Zhou, Kevin P. O'Brien, Swastik Kar, and Saroj K. Nayak. Effect of layer stacking on the electronic structure of graphene nanoribbons. *ACS Nano*, 5(8):6096–6101, 2011.

[16] A. Kimouche, M. M. Ervasti, R. Drost, S. Halonen, A. Harju, P. M. Joensuu, J. Sainio, and P. Liljeroth. Ultra-narrow metallic armchair graphene nanoribbons. *Nat Commun*, 6:10177, 2015.

[17] Justin C Koepke, Joshua D Wood, Cedric M Horvath, Joseph W Lyding, and Salvador Barraza-Lopez. Preserving the 7 7 surface reconstruction of clean si (111) by graphene adsorption. *Applied Physics Letters*, 107(7):071603, 2015.

[18] Anton Kokalj. Xcrysden—a new program for displaying crystalline structures and electron densities. *Journal of Molecular Graphics and Modelling*, 17(3–4):176–179, 1999.

[19] Georg Kresse and Jürgen Furthmüller. Efficiency of ab-initio total energy calculations for metals and semiconductors using a plane-wave basis set. *Computational Materials Science*, 6(1):15–50, 1996.

[20] Georg Kresse and Jürgen Furthmüller. Efficient iterative schemes for ab initio total-energy calculations using a plane-wave basis set. *Physical Review B*, 54(16):11169, 1996.

[21] Liangbo Liang and Vincent Meunier. Electronic structure of assembled graphene nanoribbons: Substrate and many-body effects. *Physical Review B*, 86(19):195404, 2012.

[22] Liangbo Liang and Vincent Meunier. Atomically precise graphene nanoribbon heterojunctions for excitonic solar cells. *The Journal of Physical Chemistry C*, 119(1):775–783, 2014.

[23] S. Linden, D. Zhong, A. Timmer, N. Aghdassi, J. H. Franke, H. Zhang, X. Feng, K. Müllen, H. Fuchs, L. Chi, and H. Zacharias. Electronic structure of spatially aligned graphene nanoribbons on au(788). *Physical Review Letters*, 108(21):216801, 2012.

[24] JW Lyding, TC Shen, JS Hubacek, JR Tucker, and GC Abeln. Nanoscale patterning and oxidation of hpassivated si (100)2 1 surfaces with an ultrahigh vacuum scanning tunneling microscope. *Applied physics letters*, 64(15):2010–2012, 1994.

[25] JW Lyding, S Skala, JS Hubacek, R Brockenbrough, and G Gammie. Variable-temperature scanning tunneling microscope. *Review of Scientific Instruments*, 59(9):1897–1902, 1988.

[26] A. Narita, X. Feng, Y. Hernandez, S. A. Jensen, M. Bonn, H. Yang, I. A. Verzhbitskiy, C. Casiraghi, M. R. Hansen, A. H. Koch, G. Fytas, O. Ivasenko, B. Li, K. S. Mali, T. Balandina, S. Mahesh, S. De Feyter, and K. Mullen. Synthesis of structurally well-defined and liquid-phase-processable graphene nanoribbons. *Nat Chem*, 6(2):126–32, 2014.

[27] J. B. Neaton, Mark S. Hybertsen, and Steven G. Louie. Renormalization of molecular electronic levels at metal-molecule interfaces. *Physical Review Letters*, 97(21):216405, 2006.

[28] M. Pan, E. C. Girao, X. Jia, S. Bhaviripudi, Q. Li, J. Kong, V. Meunier, and M. S. Dresselhaus. Topographic and spectroscopic characterization of electronic edge states in cvd grown graphene nanoribbons. *Nano Lett*, 12(4):1928–33, 2012.

[29] C. Park, H. Yang, A. J. Mayne, G. Dujardin, S. Seo, Y. Kuk, J. Ihm, and G. Kim. Formation of unconventional standing waves at graphene edges by valley mixing and pseudospin rotation. *Proc Natl Acad Sci U S A*, 108(46):18622–5, 2011.

[30] John P Perdew, Kieron Burke, and Matthias Ernzerhof. Generalized gradient approximation made simple. *Physical review letters*, 77(18):3865, 1996.

[31] K. A. Ritter and J. W. Lyding. The influence of edge structure on the electronic properties of graphene quantum dots and nanoribbons. *Nat Mater*, 8(3):235–42, 2009.

[32] P. Ruffieux, J. Cai, N. C. Plumb, L. Patthey, D. Prezzi, A. Ferretti, E. Molinari, X. Feng, K. Mullen, C. A. Pignedoli, and R. Fasel. Electronic structure of atomically precise graphene nanoribbons. *ACS Nano*, 6(8):6930–5, 2012.

[33] Pascal Ruffieux, Shiyong Wang, Bo Yang, Carlos Sánchez-Sánchez, Jia Liu, Thomas Dienel, Leopold Talirz, Prashant Shinde, Carlo A. Pignedoli, Daniele Passerone, Tim Dumslaff, Xinliang Feng, Klaus Müllen, and Roman Fasel. On-surface synthesis of graphene nanoribbons with zigzag edge topology. *Nature*, 531(7595):489–492, 2016.

[34] Laura B. Ruppalt and Joseph W. Lyding. Charge transfer between semiconducting carbon nanotubes and their doped gaas(110) and inas(110) substrates detected by scanning tunnelling spectroscopy. *Nanotechnology*, 18(21):215202, 2007.

[35] Laura B Ruppalt and Joseph W Lyding. Metalinduced gap states at a carbonnanotube intramolecular heterojunction observed by scanning tunneling microscopy. *Small*, 3(2):280–284, 2007.

[36] M. G. Schwab, A. Narita, Y. Hernandez, T. Balandina, K. S. Mali, S. De Feyter, X. Feng, and K. Mullen. Structurally defined graphene nanoribbons with high lateral extension. *J Am Chem Soc*, 134(44):18169–72, 2012.

[37] M Shishkin and G Kresse. Self-consistent g w calculations for semiconductors and insulators. *Physical Review B*, 75(23):235102, 2007.

[38] Hajo Söde, Leopold Talirz, Oliver Gröning, Carlo Antonio Pignedoli, Reinhard Berger, Xinliang Feng, Klaus Müllen, Roman Fasel, and Pascal Ruffieux. Electronic band dispersion of graphene nanoribbons via fourier-transformed scanning tunneling spectroscopy. *Physical Review B*, 91(4):045429, 2015.

[39] L. Talirz, P. Ruffieux, and R. Fasel. On-surface synthesis of atomically precise graphene nanoribbons. *Adv Mater*, 28(29):6222–6231, 2016.

[40] Kristian S. Thygesen and Angel Rubio. Renormalization of molecular quasiparticle levels at metal-molecule interfaces: Trends across binding regimes. *Physical Review Letters*, 102(4):216405, 2009.

[41] Björn Trauzettel, Denis V. Bulaev, Daniel Loss, and Guido Burkard. Spin qubits in graphene quantum dots. *Nature Physics*, 3(3):192–196, 2007.

[42] G. Vasseur, Y. Fagot-Revurat, M. Sicot, B. Kierren, L. Moreau, D. Malterre, L. Cardenas, G. Galeotti, J. Lipton-Duffin, F. Rosei, M. Di Giovannantonio, G. Contini, P. Le Fevre, F. Bertran, L. Liang, V. Meunier, and D. F. Perepichka. Quasi one-dimensional band dispersion and surface metallization in long-range ordered polymeric wires. *Nat Commun*, 7:10235, 2016.

[43] T. H. Vo, U. G. Perera, M. Shekhirev, M. Mehdi Pour, D. A. Kunkel, H. Lu, A. Gruverman, E. Sutter, M. Cotlet, D. Nykypanchuk, P. Zahl, A. Enders, A. Sinitskii, and P. Sutter. Nitrogen-doping induced self-assembly of graphene nanoribbon-based two-dimensional and three-dimensional metamaterials. *Nano Lett*, 15(9):5770–7, 2015.

[44] T. H. Vo, M. Shekhirev, D. A. Kunkel, M. D. Morton, E. Berglund, L. Kong, P. M. Wilson, P. A. Dowben, A. Enders, and A. Sinitskii. Large-scale solution synthesis of narrow graphene nanoribbons. *Nat Commun*, 5:3189, 2014.

[45] T. H. Vo, M. Shekhirev, D. A. Kunkel, M. D. Morton, E. Berglund, L. M. Kong, P. M. Wilson, P. A. Dowben, A. Enders, and A. Sinitskii. Large-scale solution synthesis of narrow graphene nanoribbons. *Nature Communications*, 5:3189, 2014.

[46] T. H. Vo, M. Shekhirev, A. Lipatov, R. A. Korlacki, and A. Sinitskii. Bulk properties of solution-synthesized chevron-like graphene nanoribbons. *Faraday Discuss*, 173:105–13, 2014.

[47] Shudong Wang and Jinlan Wang. Quasiparticle energies and optical excitations in chevron-type graphene nanoribbon. *The Journal of Physical Chemistry C*, 116(18):10193–10197, 2012.

[48] Y. Xu, K. T. He, S. W. Schmucker, Z. Guo, J. C. Koepke, J. D. Wood, J. W. Lyding, and N. R. Aluru. Inducing electronic changes in graphene through silicon (100) substrate modification. *Nano Lett*, 11(7):2735–42, 2011.

[49] Wei Ye, Kyoungmin Min, Pamela Peña Martin, Angus A. Rockett, N. R. Aluru, and Joseph W. Lyding. Scanning tunneling spectroscopy and density functional calculation of silicon dangling bonds on the si(100)-21:h surface. *Surface Science*, 609:147–151, 2013.

CHAPTER 3

EXTENDED CHEVRON AND POROUS GNRS ON H:SI(100)

3.1 Motivation and Theoretical Comparisons

Understanding how to modify the electronic band structure of materials is an area of important investigation. For silicon transistors, introducing a strain on the order of 10-30% can increase the hole mobility of silicon by as much as 50%.[10] The resulting performance improvement has been of tremendous commercial value. Strain engineering has also played a key role in altering the behavior of ferroelectric materials, allowing for the creation of materials that simultaneously exhibit large spontaneous electrical and magnetic polarizations, deviating from the behavior of the bulk material.[11] Another approach towards modifying the electronic band structure of materials has been to grow complex thin film heterostructures, one monolayer at a time, achieving one-dimensional atomic precision to achieve desired material behavior.[18] Atomically precise graphene nanoribbons provide an opportunity to change the band structure of a material by fabricating materials with control over the position of each atom, pushing fundamental limits in materials design. For atomically precise GNRs synthesized via solution-synthesis, dry contact transfer (DCT) enables atomic-scale characterization to assist with structural validation and electronic characterization. For graphene nanoribbons of the same chirality and family, as the width of the graphene nanoribbon increases, the bandgap is expected to decrease.[19] Verification of width-dependent bandgaps has

[1]Material in this chapter is modified and reproduced with permission from M. M. Pour, A. Lashkov, A. Radocea, X. Liu, T. Sun, A. Lipatov, R. A. Korlacki, M. Shekhirev, N. R. Aluru, J. W. Lyding, V. Sysoev, and A. Sinitskii, "Laterally extended atomically precise graphene nanoribbons with improved electrical conductivity for efficient gas sensing" Nature Communications, 2017, in press.

been shown experimentally, as demonstrated by the N = 7,[3] N = 14,[4, 13] and N = 21[4, 13] AGNRs . Understanding how the band structure of a GNR changes when there is a non-trivial width modification while working with complex GNR geometries, or increasing the width of a GNR only at selected sites requires more investigation.

The addition of a fluoranthene subunit at the edges of zigzag graphene nanoribbons (ZGNRs) dramatically alters their band strucure.[23] The 6Z GNR was found to have a bandgap of 1.3 eV with a valence band state (VB) at -0.3 eV and a GNR conduction band state (CB) at + 1.0 eV. In comparison, 6ZGNRs with fluoranthene groups attached to the edges have 0.3 eV bandgaps with VB and CB states at -0.15 eV and +0.15 eV respectively. The side groups also reduced the interaction between the zigzag GNRs and the gold substrate, allowing STS measurement of the GNR DOS without the need to place the ZGNRs onto an insulating NaCl layer. Since the measurements of the edge-modified ZGNRs were performed directly on a gold substrate, an increased screening interaction may also decrease the measured bandgap.[14, 21] More work is needed to understand how increasing the width of a GNR at only selected sites alters GNR bandgaps.

Towards this end, an extended chevron GNR (eGNR) was synthesized and characterized. The extended chevron GNR consists of a chevron backbone with an additional naphthalene group attached at the outer elbow site oriented normal to the GNR longitudinal axis. The chevron GNR and the eGNR are shown in Figure 3.1 along with their corresponding molecular precursors. Solution-synthesis was carried out by the Sinitskii group using the precursor molecules shown in Figure 3.1. Since these graphene nanoribbons have never been previously studied, scanning tunneling microscopy plays a key role in confirming their structure. Scanning tunneling spectroscopy provides electronic characterization to evaluate structure property relationships and measure changes in electronic structure that arise from structural modifications.

3.2 Extended Chevron GNRs

The extended chevron GNR was studied on H:Si(100) to enable a direct comparison to the parent chevron geometry while ruling out any substrate effects. The surface is prepared by heating Si(100) at 600 °C for 8 x 10^{-16} hours under UHV (base pressure 5 x 10^{-11} Torr) to removed adsorbates. The sample is then rapidly heated to 1200-1250 °C for up to 30 seconds over three or more cycles with the last cycle lasting 10 seconds. The sample is then slowly cooled to 377 °C and exposed to 1200 Langmuir of atomic hydrogen produced by a heated tungsten cracking filament in a background pressure of 1 x 10^{-6} Torr of H_2. The substrate is then cooled to room temperature, and imaged with STM to verify substrate cleanliness. GNR solution synthesis results in a powder which is coated onto a frayed fiberglass applicator for dry contact transfer. The DCT applicator is degassed under UHV for 8-16 hours, and repeatedly pressed against the silicon surface under UHV until GNRs are found.

STM imaging of the eGNRs on H:Si(100) (Figure 3.2) shows the characteristic chevron geometry. In Figure 3.2c some intraribbon resolution is visible, which corresponds to the electronic structure of the graphene nanoribbon. The uniform height of the graphene nanoribbon is most clearly seen in Figures 3.2 b-e indicating complete cyclodehydrogenation has occurred. As compared to the STM characterization of cGNRs on H:Si(100), the eGNRs were more difficult to image on the surface. Often under typical imaging conditions for the imaging of cGNRs, sample bias: -2 V, tunneling current: 10 pA, the eGNRs were found to be mobile. As a result, the imaging resolution that could be obtained has been limited. One possible reason for the increased mobility of the eGNRs on H:Si(100) is that the additional naphthalene group alters the GNR-H:Si(100) interaction analogous to the way fluoranthene side groups decreased the GNR-Au interaction for 6ZGNRs.[23] The decreased electronic coupling for the case of the ZGNRs could also indicate that side groups may reduce attractive forces between the GNR and the substrate, reducing the barrier for diffusion.

The dimensions of the eGNR and cGNR are compared in Figure 3.3. The length scales are calibrated to the silicon lattice. Height profiles taken along the solid white lines in Figure 3.3a,b along and across the nanoribbon are shown in Figure 3.3c-f. The expected 1.7 nm period is observed for both the eGNR and the cGNR.[3] While the cGNR has an apparent width of 2.2 nm, the apparent width of the eGNR is 2.45 nm, which is consistent with increased lateral extension. Since scanning tunneling microscopy detects the sample's local of density of states, it does not reflect the true atomic positions. Furthermore, the tip has a finite width leading to tip convolution effects that result in a lateral width measurement that is larger than would be expected from considering only atomic positions (1.7 nm for the cGNR). Although a difference in the apparent height (0.4 nm for the eGNR and 0.28 nm for the cGNR) is measured, the 0.40 nm height of the eGNR falls within the distribution of heights that has been previously observed for cGNRs on H:Si(100).[23]

3.3 Scanning Tunneling Spectroscopy of Extended Chevron GNR

The results of first principles computational modeling carried are shown in Figure 3.4. DFT predicts that the additional extension of the chevron GNR will change the bandgap from 1.6 eV (3.78 GW correction) to 1.38 eV (3.38 GW correction). Notably the dispersion relation is altered as well, and the increased slope of the conduction and valence bands indicates that the eGNRs are expected to have a smaller effective mass than the cGNRs. Scanning tunneling spectroscopy is performed to experimentally determine the bandgap of the eGNR. While an STM topograph is being collected in constant current mode, the tip is paused at selected locations, and I-V spectroscopy is collected with the feedback loop suspended. During variable spacing mode, the tip is moved a few angstroms closer to the surface than the setpoint distance along a linear ramp so that at zero sample bias the tip is closest to the surface. Variable spacing spectroscopy provides additional

sensitivity to very small tunneling signals to aid in band edge determination. The normalized tunneling conductance, $dI/dV/(I/V)$ which is proportional to the local density of states is numerically calculated from the $I-V$ data. To accurately compare bandgaps of GNRs, band onsets must be systematically determined. In the DCT study of graphene flakes on H:Si(100) by Ritter and Lyding, bandgaps were found by examining normalized dI/dV spectra. The band edge position was assigned as the intersection between the noise floor and straight lines fit to the tails of the conduction and valence bands.[24] For the narrow atomically precise graphene nanoribbons studied here, the bandgap of the silicon (1.1 eV) is smaller than that of the GNRs (2-3 eV), so the noise floor cannot be used to determine the band edge position. For GNRs on Au(111) a similar problem occurs because the gold surface state lies inside the bandgap of the GNR.[28] To overcome the challenge of a nonzero tunneling conductance (dI/dV) near the GNR band onsets, the band edge position is determined to be the intersection between straight lines fit to the tail of the GNR bands and the substrate states.[28] An example of band onset determination is shown in Figure 3.5a. The schematic in Figure 3.5b illustrates the overlap between silicon and GNR states.

STM topographs of three eGNRs are shown in Figure 3.5c-e. Dashed lines indicated show positions where I-V spectroscopy was collected. The numerically calculated normalized tunneling conductance maps $(dI/dV)/(I/V)$ are shown in Figure 3.5f-h. To determine the bandgaps of the eGNRs, the band onsets were assigned at each position along the eGNR, and the average position of the CB and VB onsets was used to determine the bandgaps. By combining all three measurements, an average eGNR bandgap of 2.66 eV $\pm$ 0.5 eV is determined. In comparison, a similar analysis of STS measurements performed for solution-synthesized chevron GNRs on H:Si(100) reveals a bandgap of ˜2.76 $\pm$ 0.3 eV. The experimentally measured bandgap of eGNRs is smaller than the theoretically predicted bandgap determined with the GW approximation (3.38 eV, Figure 3.4) due to a surface polarization effect,[6, 20, 25] which decreases the GNR bandgap. A bandgap smaller than predicted with the GW approximation is consistent with

similar data obtained for other atomically precise GNRs.[6, 25] The STS measurements reveal that eGNRs have a slightly smaller bandgap than cGNRs, which is consistent with the results of computational simulations (Figure 3.4) and the predicted effect of lateral extension. In contrast to the modification of 6ZGNRs with fluoranthene side groups, attaching naphthalene units at the elbows of eGNRs results in a modest bandgap decrease.

3.4 Porous Graphene Nanoribbons

Graphene nanopores have drawn great interest because of their ability to modify the electronic structure of graphene[1, 22, 27] as well as for use in DNA sequencing,[9, 26] molecular sieving,[15] and water desalination.[5] Experimental demonstrations of porous graphene have previously been limited by top-down fabrication methods which lack control over nanopore size and position.[7] The bottom-up self-assembly approach has produced ordered polyphenylene networks on size scales of tens of nanometers, but not ordered porous graphene.[1, 2] Forming ordered covalent porous materials is challenging due to the difficulty of preventing void and defect formation. This work shows the first experimental demonstration of atomically precise nanopores embedded into graphene nanoribbons.

The structure of the porous GNR (hGNR) studied here, shown in Figure 3.6d, resembles a chevron graphene nanoribbon with two additional naphthalene groups at the outer elbow oriented 60 degrees relative to the GNR transverse axis. An additional C-C bond leads to a closed pore. If the pores were filled, the GNR would be equivalent to an N=15 armchair GNR. STM topographs of hGNRs on H:Si(100) reveal surprising features. One would expect the pores to be imaged as depressions yet protrusions appear at the expected pore locations (Figure 3.6). The graphene nanoribbon has straight edges, and the protrusions are located at alternating sides of the ribbon, as expected from the hGNR structure. A height profile along the length of the ribbon shown in Figure 3.6b shows that the protrusions are 1.5 Å taller than the surrounding GNR. The apparent height of

the GNR away from the protrusions is 2.1 Å. The structural model (Figure 3.6d) indicates an expected width of ˜1.7 nm. The apparent width of the GNR is 2.4 nm, which is slightly larger than the width observed for the chevron GNR (Figure 3.3).

A semitransparency effect allows the underlying silicon dimer rows to be seen underneath the graphene nanoribbon.[12] The length of the GNR and the trapezoidal shape suggests that the GNR is made up of 9 monomers. The tall feature at the right of the GNR may have been formed by tearing during the DCT process. Figure 3.6c shows a three-dimensional rendering of the STM topograph in Figure 3.6a to better visualize the heights of the protrusions.

STM topographs collected in constant current mode are a result of the convolution of the density of states of the tip with that of the substrate and reflects both electronic and topographic features. Regions with high conductivity appear brighter because the same tunneling current is achieved with the tip farther from the surface. To investigate whether the observation of protrusions rather than depressions are a result of an electronic effect, images at several biases were collected. Figure 3.7a-c show topographs collected at -2.0V, -1.5 V, and -1.3 V respectively. While at -2.0 V protrusions are observed at the expected pore location, at a sample bias of -1.5 V valleys appear. Further decreasing the sample bias to -1.3 V allows the underlying substrate to be visible suggesting that the sample bias is within the bandgap of the GNR. It is expected that as the sample bias is decreased, the silicon features will become more pronounced since the GNR bandgap is larger than that of the substrate. Figure 3.7d shows an overlay of the GNR structure to indicate the pore positions. A height profile (Figure 3.7e) shows a pore period of 1.75 nm, close to the expected 1.7 nm value.

3.5 Scanning Tunneling Spectroscopy of Porous GNRs

To better understand how pores modify the band structure of atomically precise graphene nanoribbons, STS experiments were performed. The results are com-

pared to first principles computational modeling. Figure 3.8a shown an STM topograph of an hGNR on H:Si(100). The pores are not resolved, however periodic modulations along the edge of the GNR are consistent with the expected 1.7 nm period. STS I-V data were collected along the white dashed line. The normalized tunneling conductance is numerically calculated and potted in Figure 3.8b. The conduction band features a distinct state at the center of the GNR, and another state located at the ends of the GNR. The valence band shows similar behavior, with a distinct state at the center of the GNR, and another set of states at the GNR ends. The bandgap between the states at the ends of the GNR is 2.73 eV, while the separation between the states at the center of the GNR is 1.76 eV.

The GW approximation for cGNRs predicted a bandgap of 3.8 eV, yet experimentally a 2.76 eV bandgap was measured. For hGNRs, the GW approximation predicts a 2.89 eV bandgap (Figure 3.8f) for infinite hGNRs (Figure 3.8e), roughly 0.9 eV smaller. The 1.76 eV bandgap measured in Figure 3.8b is roughly 1.0 eV smaller than the average bandgap found for cGNRs, consistent with the expected behavior of the hGNR bandgap. In contrast, the STS map shown in Figure 3.8d shows a bandgap of 2.50 eV, which is significantly larger than expected for hGNRs based on the considerations above, and probably results from additional quantum size effects due to the short length of the hGNR (Figure 3.8c). To verify whether the observed states are due to the GNR, the substrate, or if any states can be attributed to the GNR pores, the DOS of a 9-monomer long GNR (Figure 3.8g) was simulated. Since DFT underestimates bandgaps by as much as 50%, the simulated DOS should not be used to directly compare energy positions. Instead, the emphasis should be on comparisons between the experimental and expected spatial distribution of the local density of states, and the energy level ordering. The four simulated electronic states corresponding to the VB-1, VB, CB, and CB+1 states labeled in in Figure 3.8h have a spatial distribution that is plotted in simulated LDOS maps in Figure 3.8k. State 1 (VB-1) is expected to have a nearly uniform DOS across the GNR, with a nearly even distribution of DOS

between the pores and the GNR edges. State 2 (VB) is expected to have a DOS concentrated at the ends of the GNR, with the density concentrated at the pore locations. State 3 (CB) is expected to be concentrated long the edges of the GNR. State 4 (CB+1) shows a significant DOS at the GNR pores, and is expected to span the entire length of the GNR. These results disagree with the experimentally measured normalized dI/dV map (Figure 3.8i) which clearly show that the CB and the VB states are expected to be concentrated at the center of the GNR while the CB+1 and the VB-1 states are located at the ends of the GNR.

One potential reason for the disagreement could be that there is an energetic splitting of the GNR states due to magnetic ordering, which is not captured by the present set of DFT simulations which do not consider spin. Magnetic ordering leads to an energy splitting in zigzag GNRs causing them to be magnetic.[16, 17, 23, 29] Non spin-polarized DFT simulations of periodic graphene nanopores with periodic boundary conditions reveal that not all graphene nanopores lead to semiconducting behavior. For a hexagonal graphene nanopore array of the same size present in the hGNRs, the band structure depends strongly on the pore separation.[22] When the pore separation along the armchair direction is an odd number of carbon atoms, the nanopore arrays are predicted to be metallic, analogous to the predicted behavior for zigzag GNRs. Spin-polarized DFT studies show that when the graphene sublattices are symmetric in porous graphene systems, no magnetic ordering takes place.[8] For triangularly shaped pores there are degenerate bands at the Fermi level, and since there are a different number of atoms on each sublattice, according to Lieb's rule magnetic ordering is expected as is observed from the spin-polarized DFT calculations.[27] However it should be noted that Lieb's rule fails to predict magnetic ordering in zigzag GNRs which feature an equal number of sublattice sites. Additional scanning tunneling spectroscopy and spin-polarized DFT modeling may assist in reaching better agreement between theoretical modeling and experimental measurements of the hGNR density of states.

3.6 Figures

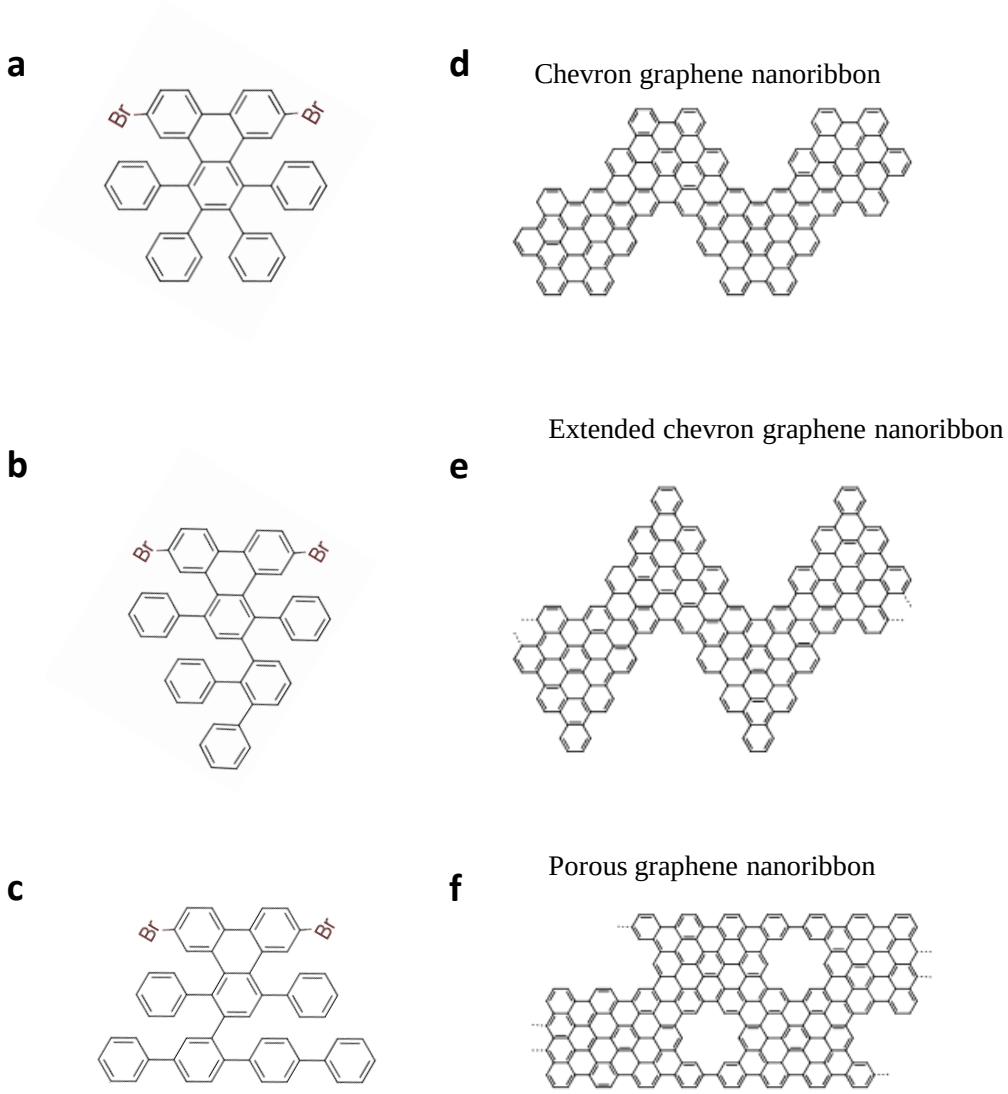

Figure 3.1: The precursors (a) 6,11-Dibromo-1,2,3,4-tetraphenyltriphenylene , (b) 2-([1,1':2',1"-terphenyl]-3'-yl)-6,11-dibromo-1,4-diphenyltriphenylene, and (c) 2-([1,1':4',1":4",1"'-quaterphenyl]-2"-yl)-6,11-dibromo-1,4-diphenyltriphenylene are used to synthesize chevron graphene nanoribbons (cGNRs), extended chevron graphene nanoribbons (eGNRs), and porous graphene nanoribbons (hGNRs), respectively.

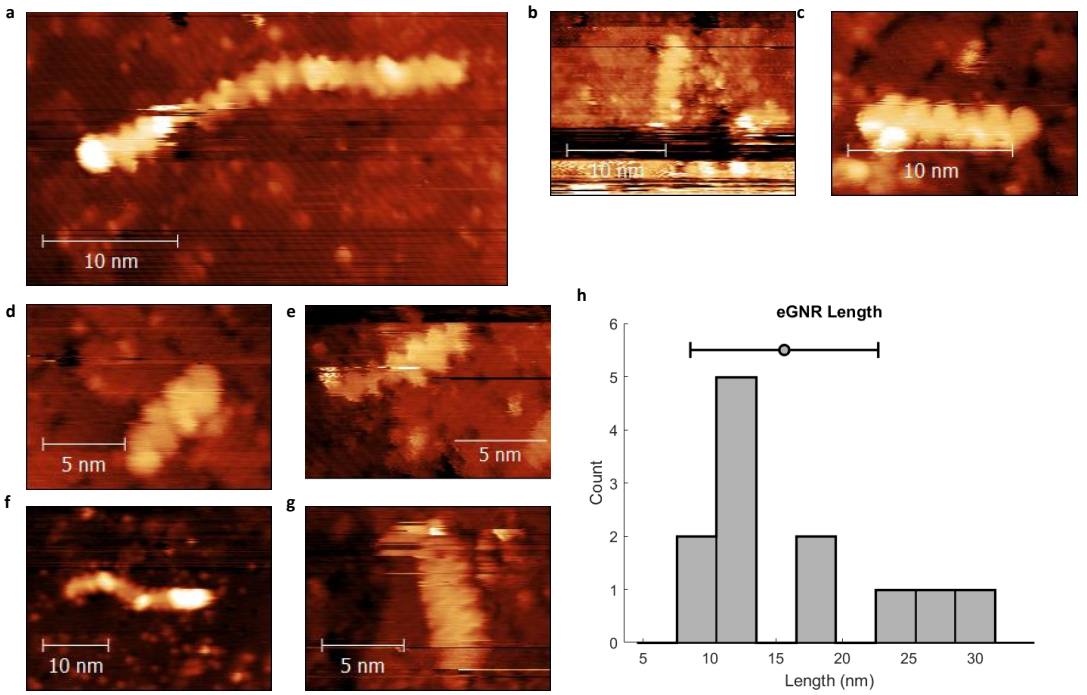

Figure 3.2: (a-d) STM image of eGNR on H:Si(100) samples bias: -2V tunneling current: 10 pA (e) STM image of eGNR on H:Si(100) sample bias: -2 V tunneling current: 0.1 nA (e) STM image of eGNR on H:Si(100) sample bias: -3 V tunneling current: 50 pA (g) STM image of eGNR on H:Si(100) sample bias: -2.5 V tunneling current: 10 pA (h) Length distributions of eGNRs imaged with DCT. The mean length is found to be 15.6 nm.

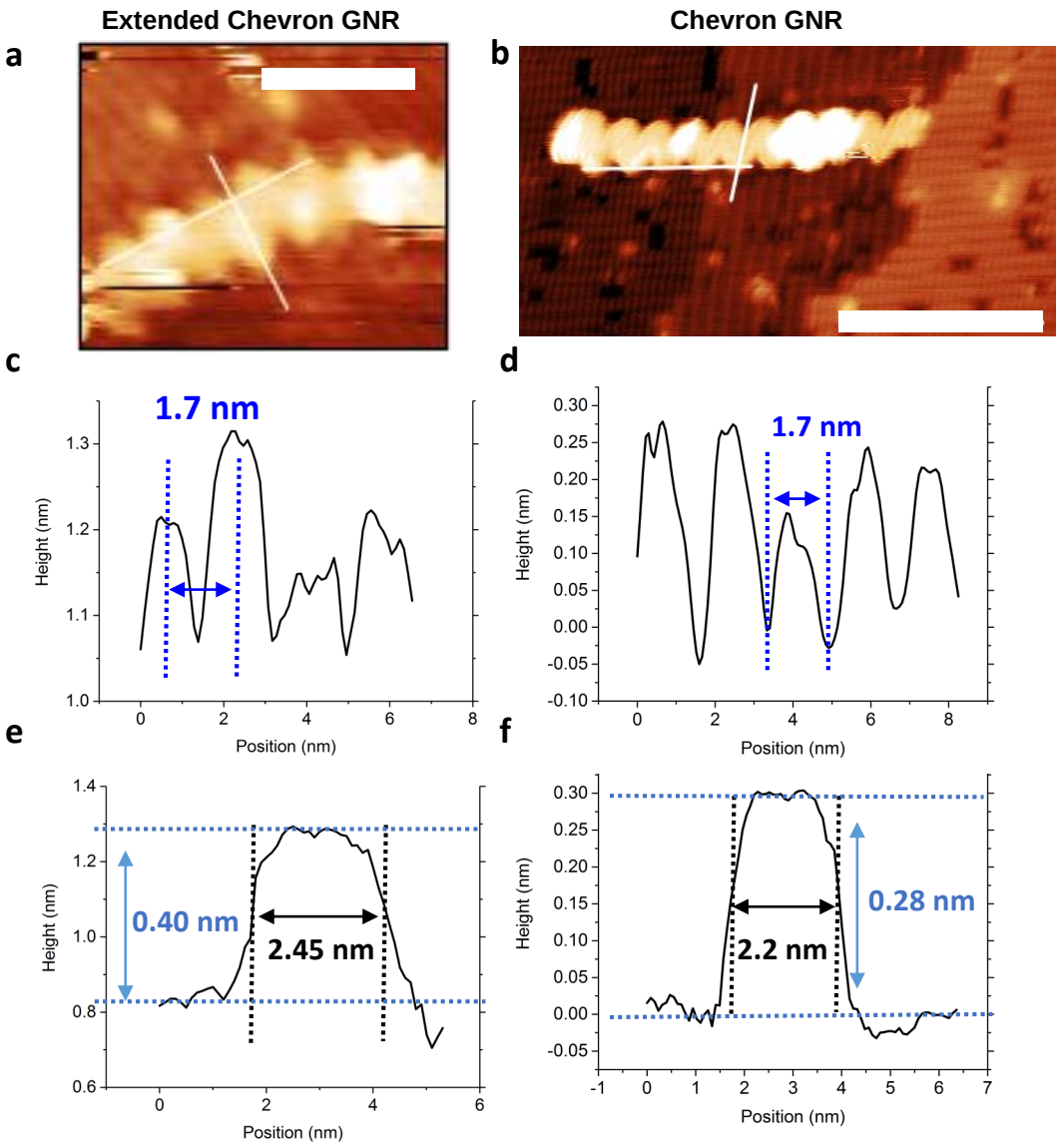

Figure 3.3: (a) STM image of eGNR on H:Si(100). Scale bar is 5 nm. Scan parameters: -2 V, 10 pA. (b) STM image of cGNR on H:Si(100). Scale bar is 5 nm. Scan parameters: -2V, 10 pA. (c,d) Height profiles along lengths of eGNR from panel (a) and cGNR from panel (b), respectively, showing the expected 1.7 nm period. (e,f) Height profiles across width of eGNR and cGNR showing an increased apparent width for the eGNR.

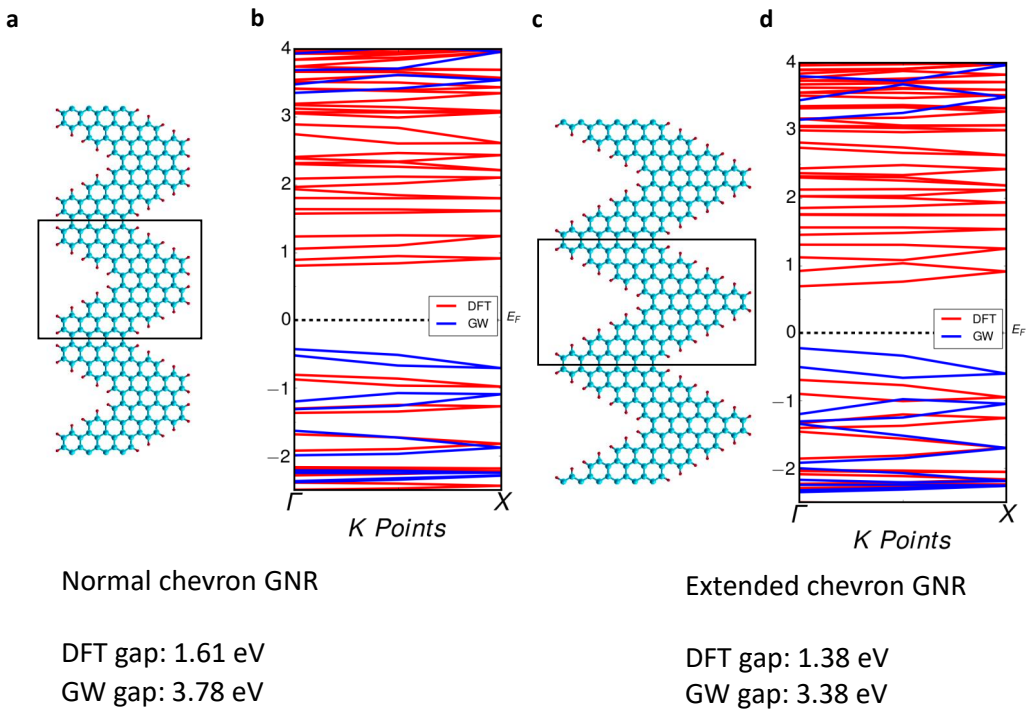

Figure 3.4: (a) structural model for chevron GNR, with the black square indicating the unit cell. (b) Band structure calculated with DFT for an infinite chevron graphene nanoribbon. The estimated bandgap is 1.61 eV. With the GW approximation, a rigid shift of the bands occurs, and the bandgap is estimated to be 3.78 eV. (c) Structural model for the extended chevron GNR indicating the eGNR unit cell. (d)Band structure calculated with DFT and the GW approximation showing a 1.38 eV bandgap and a 3.38 eV corrected bandgap. The decrease in the GNR bandgap is expected from the increased width of the eGNR.

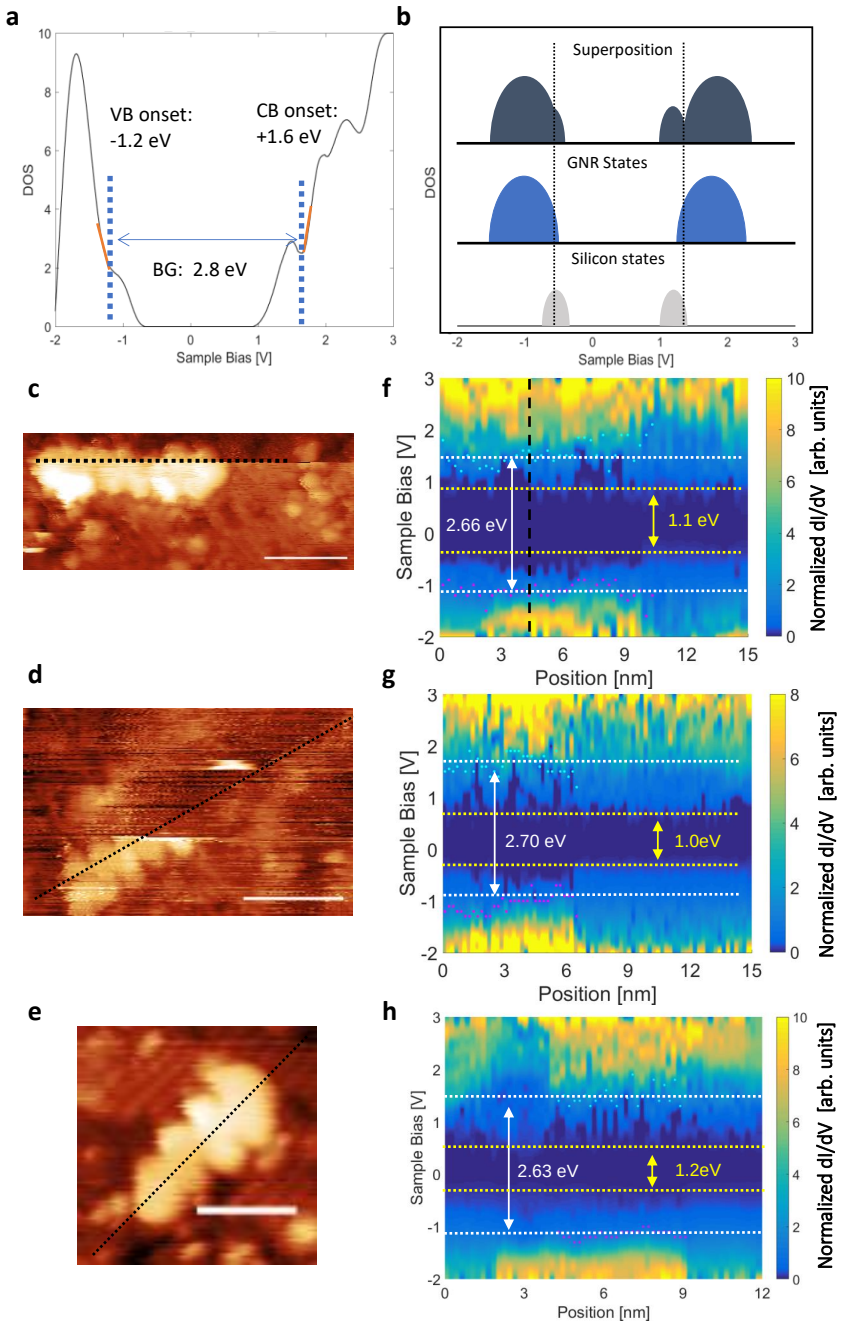

Figure 3.5: Scanning Tunneling Spectroscopy of eGNR on H:Si(100). (a) Normalized dI/dV trace corresponding to horizontal dashed line in (c). (b) A schematic illustrating that silicon and GNR states overlap, leading to a superposition of states that is experimentally measured. (c-e) STM topographs of eGNRs on H:Si(100). Scale bars are 5 nm. Scan parameters: -3 V, 10 pA. The dashed lines indicate positions where scanning tunneling spectroscopy data was collected. (f-h) Normalized dI/dV spectra maps collected along dashed line indicated in (c-e) with band onsets indicated. The valence band onsets are indicated by magenta points, and the conduction band onsets are shown in cyan. The bandgaps found are 2.66, 2.70, and 2.63 eV.

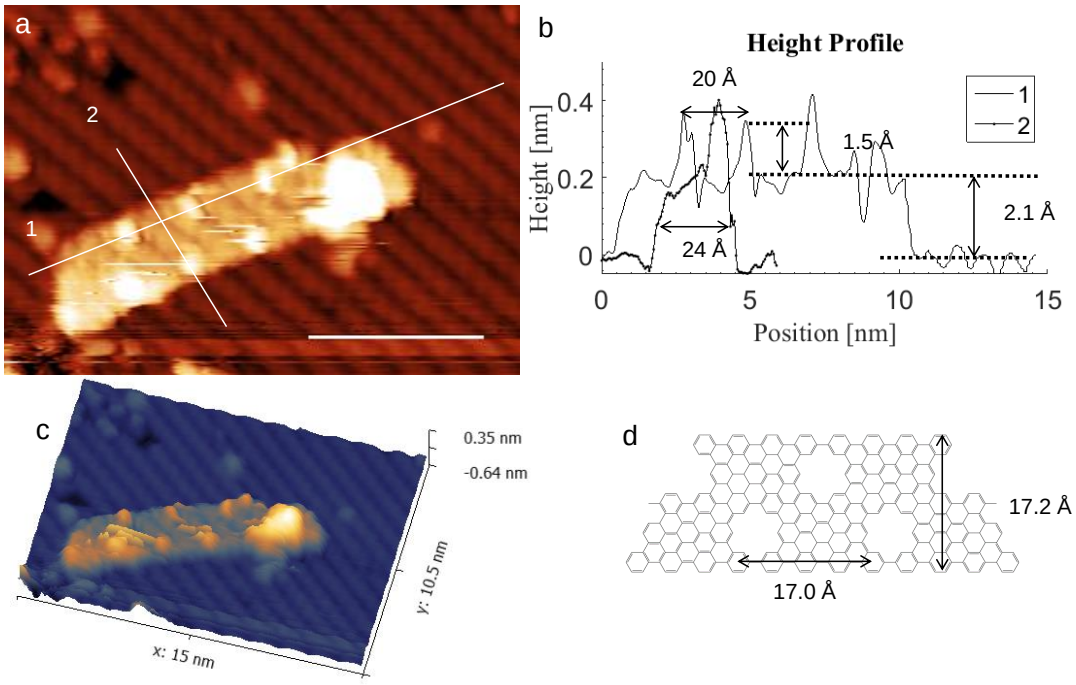

Figure 3.6: STM image of porous graphene nanoribbon on H:Si(100) collected at a sample bias of -3 V and tunneling current of 10 pA, scalebar 5 nm (a) Close-up showing graphene nanoribbon transparency as well as periodic protrusions at expected pore locations. (b) Height profile along solid white lines in (a) showing a roughly 20 Å spacing between the protrusions, consistent with the expected GNR structure. The nanoribbon height is 2.1 Å relative to the H:Si(100) substrate and the protrusions are 1.5 Å taller than surrounding GNR. Line profile 2 shows a GNR width of 2.4 nm, larger than the expected 1.72 nm width. The increased apparent width is caused by tip convolution as well as the lateral extension of the local density of states. (c) Three-dimensional view of STM topograph in (a). (d) Structure of the porous graphene nanoribbon structure and expected dimensions

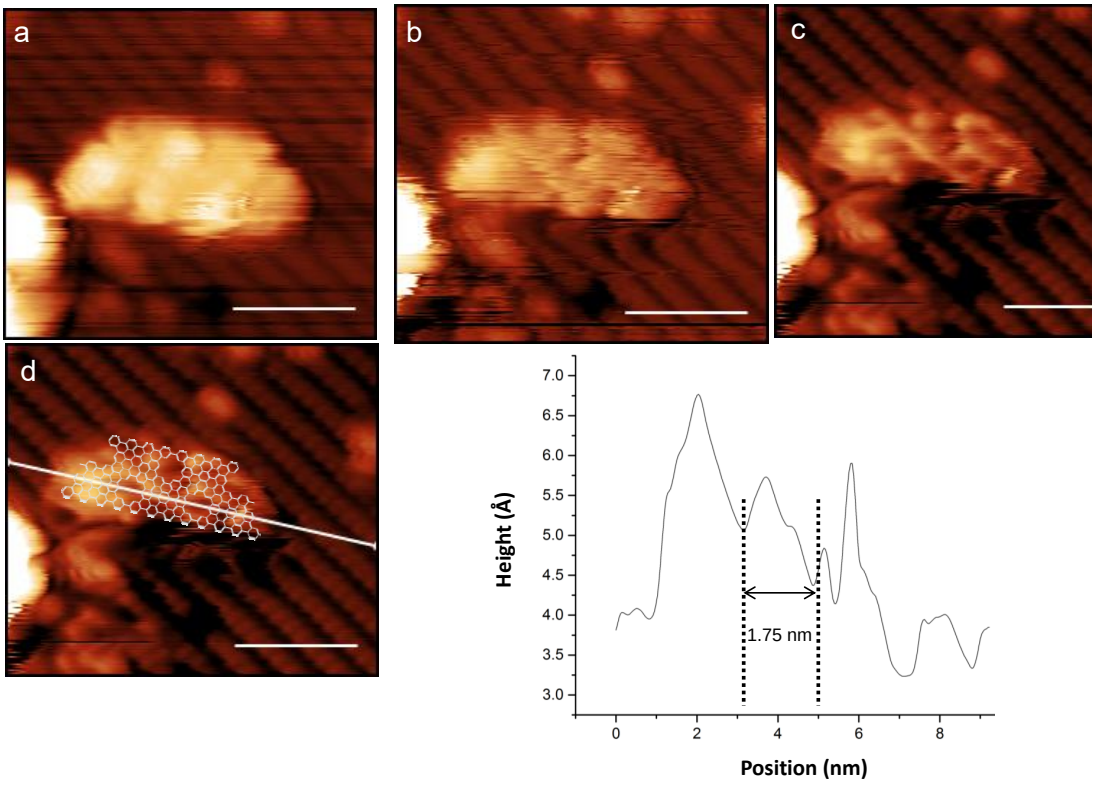

Figure 3.7: STM images of porous graphene nanoribbon on H:Si(100) collected at various sample biases. (a) At -2.0 V alternating protrusions are visible near the expected pore locations. (b) At -1.5 V valleys appear near pore locations (c) At -1.3 V valleys are clearly visible, along with a substrate transparency effect. The tunneling current is 10 pA and the,scalebars are 5 nm. (d) overlay showing positions of pores (e) Height profile along line indicated in (d). Arrow indicates pore spacing.

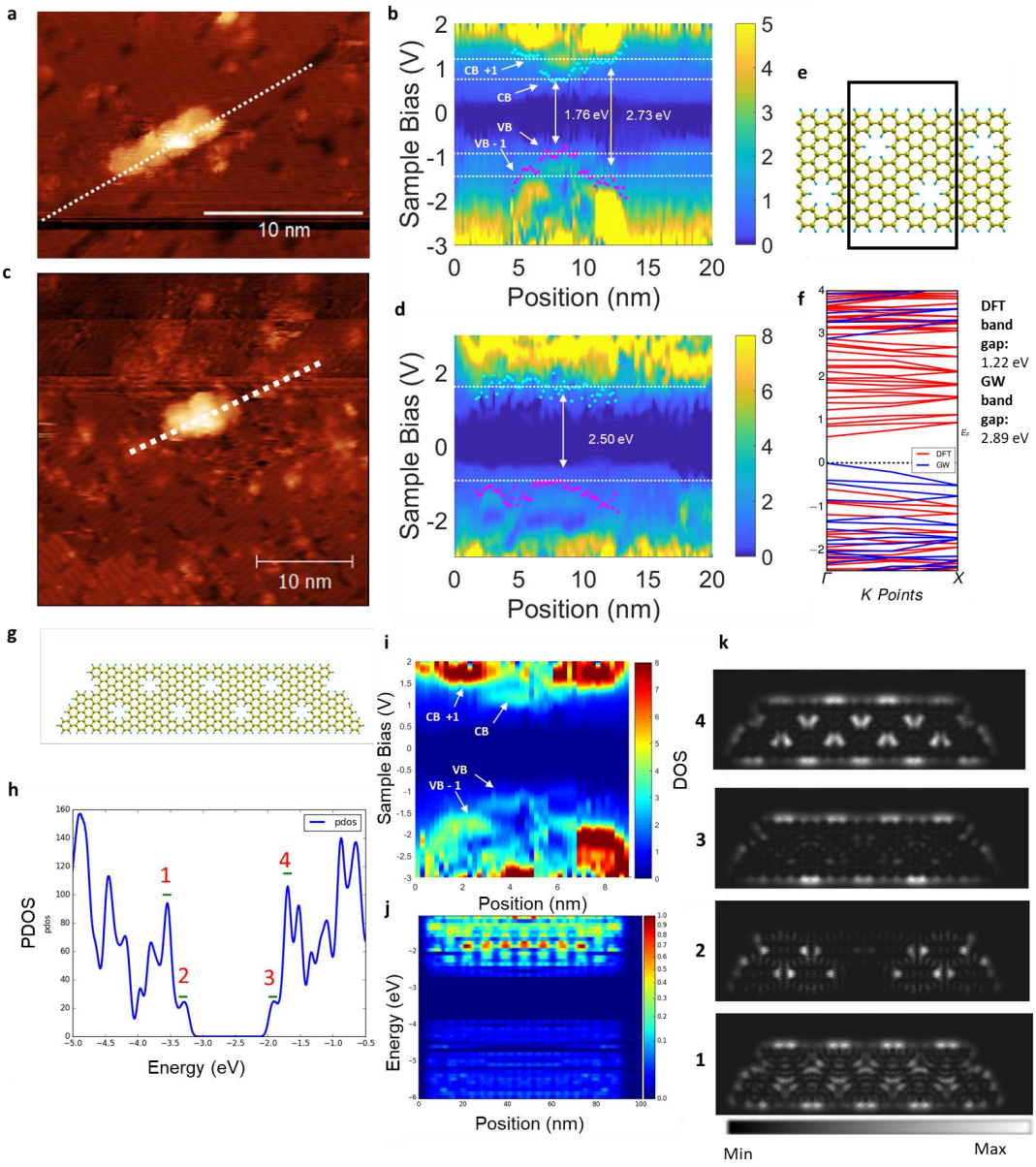

Figure 3.8: (a) STM image of hGNR on H:Si(100). Sample bias: +2.0 V tunneling current: 0.1 nA (b) Normalized dI/dV map collected along the dashed line in (a) A 1.76 eV energy separation is found between the CB and VB states. A 2.73 eV gap is measured between the CB+1 and VB-1 states. (c) STM topograph of a short hGNR on H:Si(100). -2.0 V tunneling current: 0.1 nA (d) Normalized dI/dV map collected along dashed line in (c). A 2.50 eV bandgap is measured. (e) Structural model for an hGNR. (f) Calculated band structure for infinite hGNR. (g) Structural model of a 4.5 unit-cell GNR, consistent with the lengths of the GNRs observed in both (a) and (b). (h) Partial density of states (PDOS) plot indicating the positions of states 1-4. The green bar indicates expected energy broadening of 0.1 eV at room temperature. (i) Close-up of the STS map shown in (b) (j) Simulated LDOS map obtained by integrating the LDOS of the GNR across its width. (k) Simulated LDOS images

3.7 References

[1] M. Bieri, M. Treier, J. Cai, K. Ait-Mansour, P. Ruffieux, O. Groning, P. Groning, M. Kastler, R. Rieger, X. Feng, K. Mullen, and R. Fasel. Porous graphenes: two-dimensional polymer synthesis with atomic precision. *Chem Commun (Camb)*, (45):6919–21, 2009.

[2] Marco Bieri, Manh-Thuong Nguyen, Oliver Groning, Jinming Cai, Matthias Treier, Kamel Ait-Mansour, Pascal Ruffieux, Carlo A Pignedoli, Daniele Passerone, and Marcel Kastler. Two-dimensional polymer formation on surfaces: insight into the roles of precursor mobility and reactivity. *Journal of the American Chemical Society*, 132(46):16669–16676, 2010.

[3] J. Cai, P. Ruffieux, R. Jaafar, M. Bieri, T. Braun, S. Blankenburg, M. Muoth, A. P. Seitsonen, M. Saleh, X. Feng, K. Mullen, and R. Fasel. Atomically precise bottom-up fabrication of graphene nanoribbons. *Nature*, 466(7305):470–3, 2010.

[4] Y. C. Chen, D. G. de Oteyza, Z. Pedramrazi, C. Chen, F. R. Fischer, and M. F. Crommie. Tuning the band gap of graphene nanoribbons synthesized from molecular precursors. *ACS Nano*, 7(7):6123–8, 2013.

[5] David Cohen-Tanugi and Jeffrey C Grossman. Water desalination across nanoporous graphene. *Nano letters*, 12(7):3602–3608, 2012.

[6] Richard Denk, Michael Hohage, Peter Zeppenfeld, Jinming Cai, Carlo A. Pignedoli, Hajo Söde, Roman Fasel, Xinliang Feng, Klaus Müllen, Shudong Wang, Deborah Prezzi, Andrea Ferretti, Alice Ruini, Elisa Molinari, and Pascal Ruffieux. Exciton-dominated optical response of ultra-narrow graphene nanoribbons. *Nature Communications*, 5:4253, 2014.

[7] Jonathan Eroms and Dieter Weiss. Weak localization and transport gap in graphene antidot lattices. *New Journal of Physics*, 11(9):095021, 2009.

[8] J. A. Fürst, J. G. Pedersen, C. Flindt, N. A. Mortensen, M. Brandbyge, T. G. Pedersen, and A. P. Jauho. Electronic properties of graphene antidot lattices. *New Journal of Physics*, 11(9):095020, 2009.

[9] S. Garaj, W. Hubbard, A. Reina, J. Kong, D. Branton, and J. A. Golovchenko. Graphene as a subnanometre trans-electrode membrane. *Nature*, 467(7312):190–193, 2010.

[10] Tahir Ghani, Michael Armstrong, Chris Auth, M Bost, P Charvat, G Glass, T Hoffmann, K Johnson, C Kenyon, and J Klaus. A 90nm high volume manufacturing logic technology featuring novel 45nm gate length strained silicon cmos transistors. In *Electron Devices Meeting, 2003. IEDM'03 Technical Digest. IEEE International*, pages 11.6. 1–11.6. 3. IEEE.

[11] J. H. Haeni, P. Irvin, W. Chang, R. Uecker, P. Reiche, Y. L. Li, S. Choudhury, W. Tian, M. E. Hawley, B. Craigo, A. K. Tagantsev, X. Q. Pan, S. K. Streiffer, L. Q. Chen, S. W. Kirchoefer, J. Levy, and D. G. Schlom. Room-temperature ferroelectricity in strained srtio3. *Nature*, 430(7001):758–61, 2004.

[12] Kevin T. He, Justin C. Koepke, Salvador Barraza-Lopez, and Joseph W. Lyding. Separation-dependent electronic transparency of monolayer graphene membranes on iiiv semiconductor substrates. *Nano Lett*, 10(9):3446–3452, 2010.

[13] Han Huang, Dacheng Wei, Jiatao Sun, Swee Liang Wong, Yuan Ping Feng, A. H. Castro Neto, and Andrew Thye Shen Wee. Spatially resolved electronic structures of atomically precise armchair graphene nanoribbons. *Scientific Reports*, 2:983, 2012.

[14] N. Kharche and V. Meunier. Width and crystal orientation dependent band gap renormalization in substrate-supported graphene nanoribbons. *J Phys Chem Lett*, 7(8):1526–33, 2016.

[15] Steven P Koenig, Luda Wang, John Pellegrino, and J Scott Bunch. Selective molecular sieving through porous graphene. *Nature nanotechnology*, 7(11):728–732, 2012.

[16] Y. Y. Li, M. X. Chen, M. Weinert, and L. Li. Direct experimental determination of onset of electron-electron interactions in gap opening of zigzag graphene nanoribbons. *Nat Commun*, 5:4311, 2014.

[17] G. Z. Magda, X. Jin, I. Hagymasi, P. Vancso, Z. Osvath, P. Nemes-Incze, C. Hwang, L. P. Biro, and L. Tapaszto. Room-temperature magnetic order on zigzag edges of narrow graphene nanoribbons. *Nature*, 514(7524):608–11, 2014.

[18] Julia A Mundy, Charles M Brooks, Megan E Holtz, Jarrett A Moyer, Hena Das, Alejandro F Rébola, John T Heron, James D Clarkson, Steven M Disseler, and Zhiqi Liu. Atomically engineered ferroic layers yield a room-temperature magnetoelectric multiferroic. *Nature*, 537(7621):523–527, 2016.

[19] Kyoko Nakada, Mitsutaka Fujita, Gene Dresselhaus, and Mildred S. Dresselhaus. Edge state in graphene ribbons: Nanometer size effect and edge shape dependence. *Physical Review B*, 54(24):17954–17961, 1996.

[20] J. B. Neaton, Mark S. Hybertsen, and Steven G. Louie. Renormalization of molecular electronic levels at metal-molecule interfaces. *Physical Review Letters*, 97(21):216405, 2006.

[21] Jeffrey B Neaton, Mark S Hybertsen, and Steven G Louie. Renormalization of molecular electronic levels at metal-molecule interfaces. *Physical review letters*, 97(21):216405, 2006.

[22] Fangping Ouyang, Shenglin Peng, Zhongfan Liu, and Zhirong Liu. Bandgap opening in graphene antidot lattices: The missing half. *ACS Nano*, 5(5):4023–4030, 2011.

[23] A. Radocea, T. Sun, T. H. Vo, A. Sinitskii, N. R. Aluru, and J. W. Lyding. Solution-synthesized chevron graphene nanoribbons exfoliated onto h:si(100). *Nano Lett*, 17(1):170–178, 2017.

[24] K. A. Ritter and J. W. Lyding. The influence of edge structure on the electronic properties of graphene quantum dots and nanoribbons. *Nat Mater*, 8(3):235–42, 2009.

[25] Pascal Ruffieux, Jinming Cai, Nicholas C. Plumb, Luc Patthey, Deborah Prezzi, Andrea Ferretti, Elisa Molinari, Xinliang Feng, Klaus Müllen, Carlo A. Pignedoli, and Roman Fasel. Electronic structure of atomically precise graphene nanoribbons. *ACS Nano*, 6(8):6930–6935, 2012.

[26] Zuzanna S Siwy and Matthew Davenport. Nanopores: graphene opens up to dna. *Nature nanotechnology*, 5(10):697–698, 2010.

[27] Mihajlo Vanevi, Vladimir M. Stojanovi, and Markus Kindermann. Character of electronic states in graphene antidot lattices: Flat bands and spatial localization. *Physical Review B*, 80(4):045410, 2009.

[28] Timothy H. Vo, U. Gayani E. Perera, Mikhail Shekhirev, Mohammad Mehdi Pour, Donna A. Kunkel, Haidong Lu, Alexei Gruverman, Eli Sutter, Mircea Cotlet, Dmytro Nykypanchuk, Percy Zahl, Axel Enders, Alexander Sinitskii, and Peter Sutter. Nitrogen-doping induced self-assembly of graphene nanoribbon-based two-dimensional and three-dimensional metamaterials. *Nano Letters*, 15(9):5770–5777, 2015.

[29] S. Wang, L. Talirz, C. A. Pignedoli, X. Feng, K. Mullen, R. Fasel, and P. Ruffieux. Giant edge state splitting at atomically precise graphene zigzag edges. *Nat Commun*, 7:11507, 2016.

CHAPTER 4

TIP-INDUCED POLYMERIZATION OF POLYANTHRYLENE

4.1 Background and Motivation

One of the most promising routes for controlling the bandgap of graphene is the bottom-up synthesis of graphene into nanoribbons from bromoaromatic precursors. While this approach forms nanoribbons with well-defined widths and atomically precise armchair edges that are necessary to ensure bandgap uniformity, thermal synthesis does not adequately address the problem of positional control, hindering the fabrication of graphene nanoribbon transistors. To address this challenge we use UHV STM to demonstrate spatial control over the polymerization of 10,10-dibromo-9,9-bianthracene (DBBA) into polyanthrylene (PA) on Au(111). STM imaging shows that precursor molecules assemble into non-covalent two-dimensional islands. By varying sample temperature during and after deposition, we observe three different adsorbate arrangements. Polymerization of the molecules is initiated by tunneling electrons at sufficiently high sample bias. By moving the tip along a controlled path, polyanthrylene nucleation is positionally controlled. This work highlights the feasibility of electron-driven polyanthrylene formation, indicating a path towards positional control of graphene nanoribbon synthesis.

Graphene is a two-dimensional honeycomb lattice of carbon atoms. The high carrier mobility of graphene makes the material particularly attractive for computing, where high switching speeds are desirable. Because graphene has no bandgap, its use is limited to applications such as transparent electrodes, and ultrahigh frequency transistors, where low on-off ratios are tolerable.[24] Opening

a bandgap in graphene is paramount for controlling its transport characteristics and expanding graphene's uses.[26] Strategies for band-gap engineering of graphene include chemical modification via fluorination,[30] hydrogenation,[2] or oxidation[22] as well as applying a bias to bilayer graphene.[39] These approaches are not sufficient because the bandgap of the resulting material is too small, the high mobility is lost, or thermal and chemical stability is poor. Alternatively, the bandgap of graphene can be controlled by lateral confinement in the form of rafts or ribbons.[38] But because the band structure of such quantum confined forms of graphene depends sensitively on the width and length of the raft or ribbon, and also on the structure of the edge (zigzag vs. armchair), it is crucial to ensure that these structural attributes are precisely controlled.[29] One way to achieve such control is through bottom-up synthesis from precursors designed to form ordered graphene nanostructures. For example, when adsorbed monolayers of 10,10-dibromo-9,9-bianthracene (DBBA) on gold surfaces are heated, they self-assemble by means of dehalogenation and dehydrogenation reactions into atomically precise armchair graphene nanoribbons (GNRs).[13] There is considerable interest in the synthesis of GNRs by such thermally driven reactions.[3, 17, 1]

Although this thermal method gives GNRs with precisely controlled widths and edge structures, the positions and the orientations of the resulting GNRs are more or less random, and this lack of control greatly complicates the formation of contacts to such structures and their integration into devices.[37, 25] Alignment of GNRs in particular orientations can be achieved by taking advantage of step edges on the underlying surface, but much more precise control over the position of GNRs will be needed for reproducible device fabrication on a large scale.[14] In general, controlled top-down nanostructure formation at the atomic scale is challenging due to the difficulty in positioning individual atoms and molecules.

Here we describe a method for growing GNRs at precisely controlled positions and orientations by locally driving chemical synthesis using a scanning tunneling microscope (STM). The ability of STM to precisely deliver tunneling electrons that interact with molecules using sub-angstrom positional control enables

atomic engineering of nanostructures. One mode for inducing chemical modifications of surfaces is inelastic tunneling manipulation, where tunneling electrons access available conduction pathways using vibrational modes, and excitations of those modes lead to bond stretching and dissociation events.[34] While thermal assembly of aromatic molecules on noble metal surfaces has been studied extensively[6, 19, 5, 16] there have been few reports of the electron-mediated assembly of aromatic molecules on surfaces. In one study, the irradiation of 1,1-biphenyl-4-thiols on copper with 50 eV electrons from an electron flood-gun afforded a cross-linked carbon nanomembrane, which on annealing formed graphene.[28] In another study, STM-induced dehydrocyclization was used to form two-dimensional organometallic thienoanthracene networks at a sample bias of +3V.[32] Additionally, electrons from an STM tip were used to couple iodobenzene into biphenyl on Cu(111) at 20 K.[21] Also relevant here is the observation that STM imaging of DBBA on Cu(111) at +3.5 V at 5.6 K leads to debromination, but not covalent coupling.[20] STM tips can also induce the dehydrocyclization of partially dehydrogenated ribbons[8] and short segments of polyanthrylene that are decoupled from the Au(111) substrate.[8, 27]

The studies mentioned above indicate that interaction of surface adsorbates with the tunneling current from an STM tip can drive both dehalogenation and dehydrogenation reactions, suggesting that it should be possible to achieve the tip-induced fabrication of graphene nanostructures from bromoaromatic compounds. If suitably designed, bromoaromatic compounds can form atomically precise edges, and are constrained to linking up along one spatial dimension minimizing the potential for disorder. DBBA on Au(111) is a particularly effective system for STM manipulation because individual molecules are mobile enough for room temperature diffusion yet ensembles of molecules self-assemble into two dimensional islands that are stable at room temperature. With the molecules held in place, a controlled dose of electrons can be delivered to a fixed number of molecules; increasing the likelihood that debromination will take place. Because the C-Br bonds are the weakest in bromoaromatic compounds, choosing an

appropriate energy for the tunneling electrons should lead to selective breaking of these bonds. After dehalogenation, the molecules should polymerize. In this work, we confirm this hypothesis, and demonstrate the feasibility of a hybrid top-down/bottom-up approach towards a direct write process for fabricating GNRs at room temperature.

4.2 Experimental Setup

Experiments were performed with a home-built ultra-high vacuum (UHV) STM (base pressure 5 x 10^{-11} Torr). Au(111) on mica was prepared by magnetron sputtering ex-situ. The samples were degassed overnight before using STM imaging to confirm surface cleanliness prior to use. 10,10'-Dibromo-9,9-bianthracene (98%, AK Scientific, Inc.) was degassed for $>$ 24 hours in UHV. The precursor was thermally sublimed onto the surface in-situ using a home-made evaporator. The substrate was either held at room temperature during deposition, heated during deposition to 40 – 80 °C or held at room temperature during deposition and then heated to 100 °C for 20 minutes. The gold substrate was heated by passing current through a silicon backing. Substrate temperature was determined after STM characterization by removing the sample from the vacuum chamber, clamping a thermocouple to the Au(111) surface, and replacing the sample in the load lock. The load lock was pumped down to 5 x 10^{-9} Torr and then the sample temperature was measured as a function of heating power. STM imaging and manipulation experiments were performed at room temperature. The models for the arrangement of DBBA and PA were constructed and rendered using VMD.[23, 35]

4.3 Monolayers of DBBA

Understanding how 10,10-dibromo-9,9-bianthracene (DBBA) adsorbs onto Au(111) is a critical step towards using the STM to control the polymerization of polyanthrylene. The initial STM studies of DBBA, showing that it could thermally

self-assemble into atomically precise GNRs on Au(111)[14] did not provide STM images of the isolated monomer. Furthermore, some have reported that at low surface coverages, DBBA is highly mobile and difficult to image at room temperature.[15] A model of DBBA is shown in Figure 4.1. The molecule consists of two anthracene units joined by a single C-C bond, which allows the two halves of the molecule to rotate with respect to each other. Because of steric hindrance between adjacent hydrogen atoms, the two lobes twist relative to each other, lifting the molecule from the substrate. DBBA adsorbs onto substrates in one of two enantiomers which are indicated in Figure 4.1a.[31] The chirality of the monomer may play a role during polymerization, due to an additional activation barrier needed to overcome steric hindrance when monomers of opposite chirality attempt to couple. STM images of DBBA typically reveal a pair of round protrusions for each molecule, which correspond to the uppermost portions of the bianthryl lobes, at the locations indicated by the blue circles in Figure 4.1a.,[149, 20] The rotation angle between the two anthracene units is known as the dihedral angle (Figure 4.1b), and as the dihedral angle increases, the separation between the two uppermost protrusions of a DBBA molecule increase.[31] When viewed from the top-down, the orientation of the molecule may be ambiguous. An enantiomer rotated by 90 degrees forms the same two-lobe pattern as its chiral opposite (illustrated in Figure 4.1c). At low coverages, isolated DBBA molecules evaporated onto Au(111) are not observed at room temperature due to the high diffusivity of the species. At higher surface coverages, the molecules self-assemble into two-dimensional islands with three structures depending on the sample history, which are referred to as the columnar zigzag, armchair, and close-packed zigzag structures (Figure 4.2). DBBA molecules deposited onto Au(111) at room temperature assemble into a structure characterized by a near-rectangular 1.80 x 0.93 nm unit cell. The molecules form rows of alternating protrusions along the row direction (Figure 4.2a); each pair of protrusions corresponds to the upper halves of the two staggered anthracene rings of a single DBBA molecule. The 0.93 nm repeat distance along the row direction is larger than the 0.84 nm repeat distance seen for co-

valently linked polyanthrylene species,[14] which strongly suggests that the DBBA molecules are not covalently linked to one another. This latter finding is consistent with the observation that DBBA does not spontaneously polymerize on Au(111) at room temperature.[14, 33, 4] The 0.93 nm repeat distance is too short to allow the C-Br bonds to point along the row axis. The 1.80 nm repeat distance from row to row, however, leaves enough room for the C-Br bonds to be directed into the spaces between the rows.

The proposed arrangement of the DBBA molecules in the columnar zigzag structure is depicted by the model in Figure 4.2c. This arrangement is similar to that seen for DBBA self-assembled at room temperature on Cu(111),[20] except that the 1.1 nm repeat distance observed on Cu(111) along the row direction is larger than the 0.93 nm spacing we observe on Au(111). The zigzag structure previously reported for self-assembled DBBA deposited on Au(111) at room temperature and imaged at 77 K showed a significantly larger repeat distance of 1.25 nm.[14] STM manipulation of DBBA deposited onto Au(111) revealed that each lobe was from an individual DBBA molecule.[10] The 0.76 nm lobe-to-lobe spacing and the lattice spacings observed in Figure 4.2a are too small to accommodate two molecules.[10] The discrepancy probably reflects different coverages. At high coverages, intermolecular interactions may decrease the dihedral angle of DBBA, allowing for packing at higher densities.[31] Manipulating the structure with the STM tip readily disrupts the self-assembled network, indicating that the structure is non-covalent (Figure 4.3). Islands disrupted by the tip re-assemble at a different orientation relative to the gold lattice. If the deposition of the DBBA molecules is conducted while the Au(111) substrate is heated to ˜40 to 80 °C, an armchair structure results (Figure 4.2b) that is characterized by a 2.6 x 1.4 nm oblique unit cell ($\gamma = 102.4°$). This arrangement agrees with previous observations of DBBA self-assembled on Ag(111) at room temperature.[14, 31] We note that this configuration was previously observed for DBBA on Ag(111) at low surface coverages of up to 0.4 ML.[31] The DBBA molecules are arranged in rows of alternating enantiomers, with the C-Br bonds rotated slightly from the normal

to the row axis (Figure 4.2f) The anthracene subunits within each molecule are staggered as usual, and neighboring molecules are of opposite chirality. The 2.6 nm lattice vector along the row corresponds to two molecular units so that the molecules are spaced with a repeat distance of 1.3 nm along the row; and the perpendicular repeat distance from row to row is 1.4 nm. On Ag(111) a 2.36 nm x 1.51 nm unit cell was reported.[31] Because the armchair structure is not observed on Au(111) during deposition at room temperature, a kinetic barrier may be associated with its formation. Alternatively, differences in surface coverage may change the conformation of the molecules. This self-assembled armchair structure is non-covalent, as shown by the molecule-molecule distance, and by the ability to disrupt the structure with STM manipulation (Figure 4.5). Further annealing of the armchair structure results in polyanthrylene and nanoribbon formation.

If DBBA is deposited onto Au(111) at room temperature and the surface is then annealed at 100 °C for 20 minutes, a close-packed zigzag structure is formed which is characterized by an 2.9 x 1.6 nm rectangular unit cell which contains four DBBA molecules. Figure 4.2i depicts a tentative structure to explain the observed STM images in Figure 4.2g,h. The proposed structure features rows of DBBA dimers. Each dimer consists of two molecules parallel to each other, with the C-Br axis of each molecule rotated by 60° relative to the row axis. The two molecules inside the dimer are of opposite chirality and translated from each other. The angle between the row direction and the C-Br axis alternates between + 60° and – 60° between adjacent rows. The intermolecular spacing inside a dimer is 1 nm. Height profiles used to measure distances are shown in Figure 4.4. The close-packed zigzag structure was used to demonstrate tip-induced polyanthrylene formation.

4.4 Tip-induced polymerization of DBBA

After depositing DBBA onto Au(111) held at room temperature and subsequently annealing at 100 °C to form the close-packed zigzag structure imaged in Figure

4.2g, no polyanthrylene islands were observed. Typical imaging of the close-packed zigzag structure is non-perturbative at a sample bias of -2 V. However, scanning at a sample bias of +2 V is sufficient to polymerize the self-assembled DBBA-based radicals into polyanthrylene. Figure 4.6 shows a molecular island (a) before and (b) during scanning at a sample bias of +2 V and a tunneling current of 10 pA. Although entire scan areas are exposed to tunneling electrons, polymerization begins stochastically, and several scans can be necessary for polyanthrylene to form and reach a size large enough to become immobilized for characterization. The images acquired at a sample bias of +2 V (Figure 4.6b,d) show streaky regions indicating an unstable tip-sample junction, but the tunneling junction is more stable when imaging at a sample bias of -2 V (Figure 4.6c,e). The structures that appear in the lower-left portion of Figure 4.6e are consistent with polyanthrylene chains. The measured period is 0.78 nm (Figure 4.6g) which is similar to the 0.84 nm repeat distance previously observed for polyanthrylene.[14] Importantly, the small period excludes non-covalent species which would be expected to have larger inter-molecular spacings. Figure 4.7 shows another example of tip-induced polyanthrylene formation via STM manipulation at a sample bias of +2 V. The chains formed have a height taller than expected. As shown in Figure 4.7c,f the chains are 0.45 nm higher than the surrounding close-packed zigzag structure, which suggests a two-layer polyanthrylene island. In Figure 4.7c, the anthracene subunits are more clearly resolved.

The PA chains formed via STM manipulation align parallel to each other, however they line up at a variety of orientations relative to the close-packed zigzag structure. Figure 4.7d shows the angles observed for PA chains formed by five tip-induced polymerization experiments. The PA orients at angles in intervals of 30 degrees, indicating possible alignment to the Au(111) surface. The chains do not grow strictly parallel to the C-Br axis indicated in the proposed close-packed zigzag structural model (Figure 4.2i), and do not align to the row axis of the DBBA lattice. The chains in each island do align parallel to each other, indicating a possible self-templating effect, where PA chains can more easily grow

adjacent to an already formed PA island. Examining the orientation of the PA islands with respect to the close-packed zigzag conformation of DBBA indicates that significant structural rearrangement is required, involving the rotation of each DBBA monomer.

After the sample is scanned at a positive bias to initiate PA, the lengths of the PA chains increase with time while the sample is imaged at a bias of -2 V and a tunneling current of 10 pA (Figure 4.8). Gaps in the one-dimensional structure, as shown by the red circles in Figure 4.8, may be caused by steric hindrance preventing the growing chains from fusing because neighboring anthracene units have the same tilt directions. Designing molecular precursors without steric constraints during coupling could enable the growth of longer graphene nanoribbons.

Although covalent coupling of aryl halides is highly exothermic, diffusion barriers and the presence of adsorbed halogen atoms produced by dehalogenation provide activation barriers for covalent coupling.[7]As previously mentioned, X-ray photoelectron spectroscopy (XPS) studies show that thermal dehalogenation of DBBA on Au(111) begins at temperatures as low as 100 °C, but PA formation does not occur until 200 °C.[33, 4] It has been suggested that the presence of surface-bound bromine atoms inhibit diffusion of the DBBA-derived radicals and prevents polymerization at lower temperatures,[4] but that above 200 °C the adsorbed bromine atoms and radicals become mobile enough to enable polymerization to occur. Temperature programmed desorption studies indicate that bromine does not desorb until temperatures above 250 °C.[11] The observation of room temperature polymerization suggests that the exothermic nature of aryl coupling on Au(111) is sufficient to rearrange surface adsorbates and drive the coupling reaction.

Initiation of tip-induced polymerization can be enhanced by increasing the sample bias to +3 V and the tunneling current to 50 pA. Under these conditions, moving the tip in a straight line indicated by the arrow in Figure 4.9b, corresponding to a dose of 3 x 10^{-4} C/cm, causes polyanthrylene chains to nucleate along the path of the tip and grow along several directions. The polyanthrylene growth direction does not appear to be directly aligned to the orientation of the self-

assembled DBBA molecules. In subsequent scans the size of the polyanthrylene island continues to increase, showing that the polymerization reaction continues following initiation. The final polyanthrylene island is shown in Figure 4.9d.

4.5 Structure of polyanthrylene islands on Au(111)

The sample was further annealed to a temperature of 130 °C to drive thermal debromination of DBBA and coupling of reactive monomers into polyanthrylene. The sample was found to have regions of close-packed zigzag islands, disordered regions, and polyanthrylene islands. A high-resolution close-up of a polyanthrylene island not formed via STM manipulation reveals details about the stacking of the two-layer polyanthrylene islands. The STM topograph shown in Figure 4.11a indicates a period of 0.77 nm for both the upper and lower polyanthrylene layers (height profiles shown in Figure 4.11e-f). The height profile shown in Figure 4.11d indicates a 0.32 nm height difference between the two PA layers and a 2.41 nm spacing between the upper PA chains. The apparent height of the second layer may be lower than the expected 0.4 nm due to tip convolution effects. In Figure 4.11a, region ii provides imaging of the lower PA layer enabling determination of the structural motif. Triangles in both the STM topograph (region i) and a structural model (Figure 4.11b and Figure 4.11c) are used to label the enantiomers based on the ordering of the uplifted polyanthrylene units. The PA chains in the first layer form into pairs of enantiomers, with neighboring pairs having opposite chirality. Two PA chains are of the same chirality when the positions of the uplifted subunits are the same with respect to the length coordinate, and of opposite chirality when the uplifted unit is shifted by a half unit cell. Polyanthrylene chains in the second layer sit directly on top of every other row of the first layer, matching the chirality of the chain on which they rest, resulting in attractive π stacking interactions.[20] As indicated by the phase slip in region ii, enantiomers in the second layer do not assemble adjacent to each other suggesting that PA-substrate interactions may be necessary to overcome repulsive interactions between adjacent

chains. Surface coverage may also influence the arrangement of the second layer.

On another sample, a polyanthrylene island surrounded by gold was found. Height profiles in Figure 4.10 reveal an apparent height of 0.78 nm relative to the bare gold, indicating that the PA island is two layers high. The edges of the island have an apparent height of 0.5 nm, which is consistent with the expected height of single layer of polyanthrylene.[14, 24]

To help verify the proposed polyanthrylene structure, a sample annealed to a temperature sufficient for complete aryl-aryl coupling as well as cyclodehydrogenation was examined (Figure 4.12). By annealing the armchair DBBA structure shown in Figure 4.2b, graphene nanoribbons could be formed. However, not all of the polyanthrylene could be converted to graphene nanoribbons, and polyanthrylene was observed on top of the graphene nanoribbons. The top layer of polyanthrylene does not undergo complete cyclodehydrogenation due to separation from the gold substrate which catalyzes the cyclodehydrogenation reaction.[24] Two neighboring polyanthrylene chains are found to have a peak-to-peak separation of 1.3 nm, and an anthracene subunit spacing of 0.78 nm in agreement with single layer polyanthrylene (Figure 4.12c-d). The apparent height of the polyanthrylene chains was found to be 0.4 nm relative to the surrounding graphene nanoribbons, in agreement with previous measuremnts.[24]

Several gaps are visible in the top layer of polyanthrylene. Possible explanations may include partial dehydrogenation, the intercalation of bromine atoms, or stacking errors which arise when neighboring units of opposite chirality are unable to covalently bond due to steric hindrance. Partial dehydrogenation can be ruled out because the period along the chain inside the gaps is always 0.77 nm, rather than the expected 0.42 nm N=7 armchair graphene nanoribbon period.[13] It is possible that the height variations may be caused by the presence of intercalated Br atoms,[12] however most of the protrusions that form the top layer appear in pairs.

4.6 Discussion

Since PA is expected to have a smaller bandgap than unreacted monomers, electronic characterization can help confirm its identification.[9] STS data was obtained using PA formed on another sample prepared by depositing DBBA onto Au(111) held at room temperature, and annealing to an estimated temperature of 80 °C for 10 minutes. On this sample coexisting PA and DBBA islands were found, indicating nonuniform heating may have interfered with an accurate estimate of the sample temperature. Conversion of DBBA into PA was observed while scanning at -2 V. Figure 4.13a shows an STM topograph of a PA island that has begun forming adjacent to self-assembled DBBA molecules. In Figure 4.13b the PA island has expanded into the region previously occupied by the unreacted molecules. STS data (Figure 4.13d) indicate a 3.25 eV bandgap, in agreement with the value previously reported for PA.[18] Denk et al. plot dI/dV data and estimate a 3.7 eV bandgap using points halfway along linear slopes at the edges of the conduction and valence bands. Using their data, a 3.1 eV bandgap can be deduced by taking the intersection of the band edges and the noise floor. This is directly compared to the I-V data presented in Figure 4.13d. A recent paper reports that the a second layer of polyanthrylene has a larger bandgap due to a decreased screening interaction, and by applying the same analysis to their data, a 3.5 eV bandgap is determined for PA sitting on top of graphene nanoribbons.[24] The initial arrangement of the species in the close-packed zigzag structure is described by a 1.6 nm x 2.9 nm unit cell has a surface density of ˜0.84 bianthracene units / nm^2. The observed PA structure can be described by a 2.4 nm x 0.77 nm unit cell that contains 1.5 bianthracene units per unit cell at a surface density of ˜0.81 bianthracene units / nm^2. Because of the close match in surface density, the underlying molecules provide enough monomers to form the two-layer PA islands. The results suggest that tip-induced formation of PA is carried out via tip-induced C-Br bond cleavage which is followed by exothermic aryl coupling. The released energy can form additional reactive monomers, and rearrange the

nearby molecules to enable polymerization. Polymerization may terminate when the growing chains reach the end of the DBBA island (Figure 4.13), however in many cases the entire island is not consumed. Possible termination mechanisms include stray H atoms binding to the reactive ends of the chains[36] and full dissipation of energy to the substrate before the reactive monomers can orient themselves into favorable positions for aryl coupling to take place.

4.7 Conclusion

The molecule DBBA forms monolayers on Au(111) of different structures depending on the temperature during and after dosing. The results suggest that the self-assembly process is governed by kinetic barriers that can prevent self-assembled molecules from ordering into structures that minimize their free energy, however the surface coverage may also influence the conformation of the adsorbates. Significantly, we demonstrate the tip-induced polymerization of DBBA into polyanthrylene with nanoscale control. This is the first demonstration of electron mediated polyanthrylene synthesis, as well as the first example of tip-induced Ullmann coupling at room temperature. The dehydrogenation of the polyanthrylene chains into GNRs is currently being investigated as a method to control the top-down direct-write of graphene nanostructures.

4.8 Figures

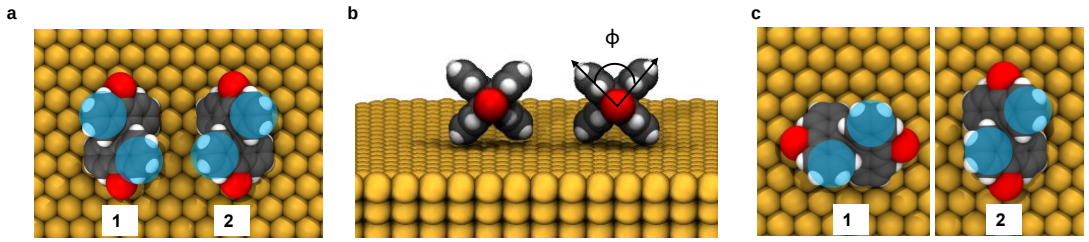

Figure 4.1: (a) Model of DBBA on Au(111). Gray spheres indicate carbon, white spheres indicate hydrogen, and red spheres indicate bromine. The overlaid blue circles indicate the uppermost portions of the DBBA molecules which are most readily imaged with STM due to the twisting of the anthracene units. Upon adsorption onto a surface, DBBA forms one of two enantiomers, both of which are drawn above. (b) The dihedral angle, ϕ, is indicated. Larger dihedral angles indicate strong substrate-molecule interactions.(c) The positions of the two uppermost protrusions are same for DBBA and its enantiomer rotated by 90° leading to some ambiguity in the interpretation of STM topographs.

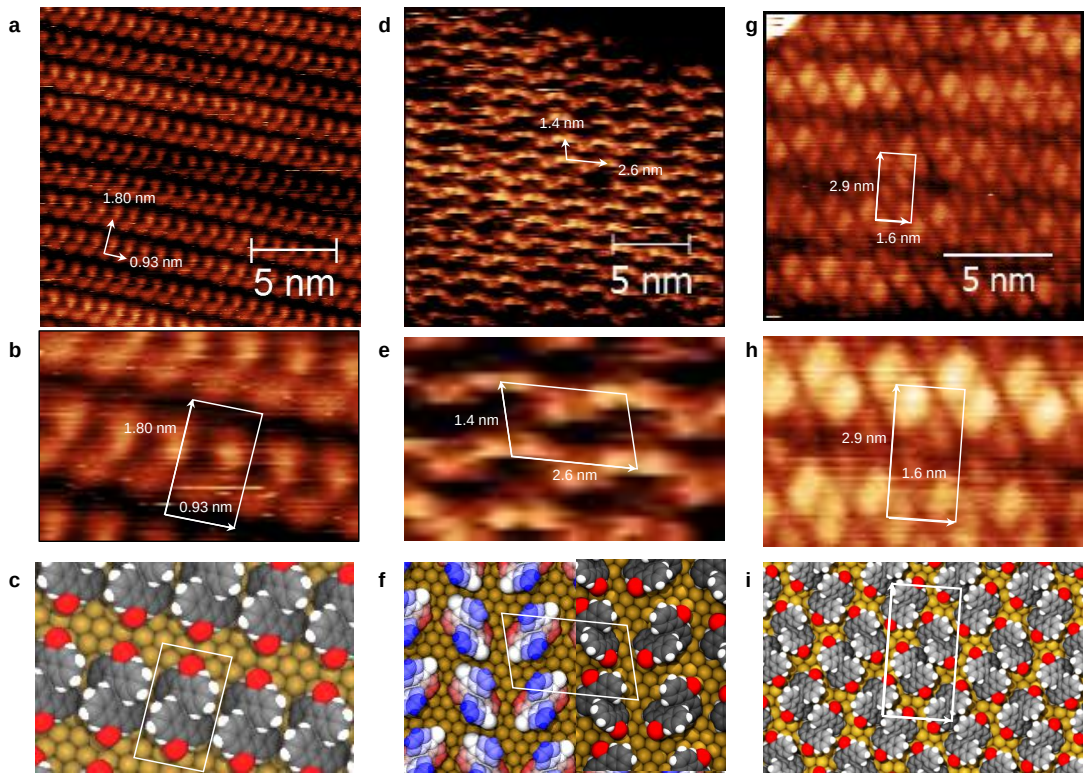

Figure 4.2: (a) DBBA deposited on Au(111) at room temperature assembles into a columnar zigzag structure. (d) DBBA deposited on Au(111) at 40-80 °C forms an armchair structure. (g) A close-packed zigzag structure is observed after annealing the columnar zigzag structure at 100 °C for 20 minutes. (b,e,h) Close-ups of the DBBA molecules in images (a-c) showing the unit cells. (c,f,i) Proposed structural models for the DBBA conformations observed in STM images a-c. The left half of f uses a height-based colormap, with blue being the tallest portion of the DBBA molecule and red being the lowest. The blue protrusions trace out the armchair structure visible in the STM images in d,e. All STM images taken at a sample bias of -2 V and a tunneling current of 10 pA.

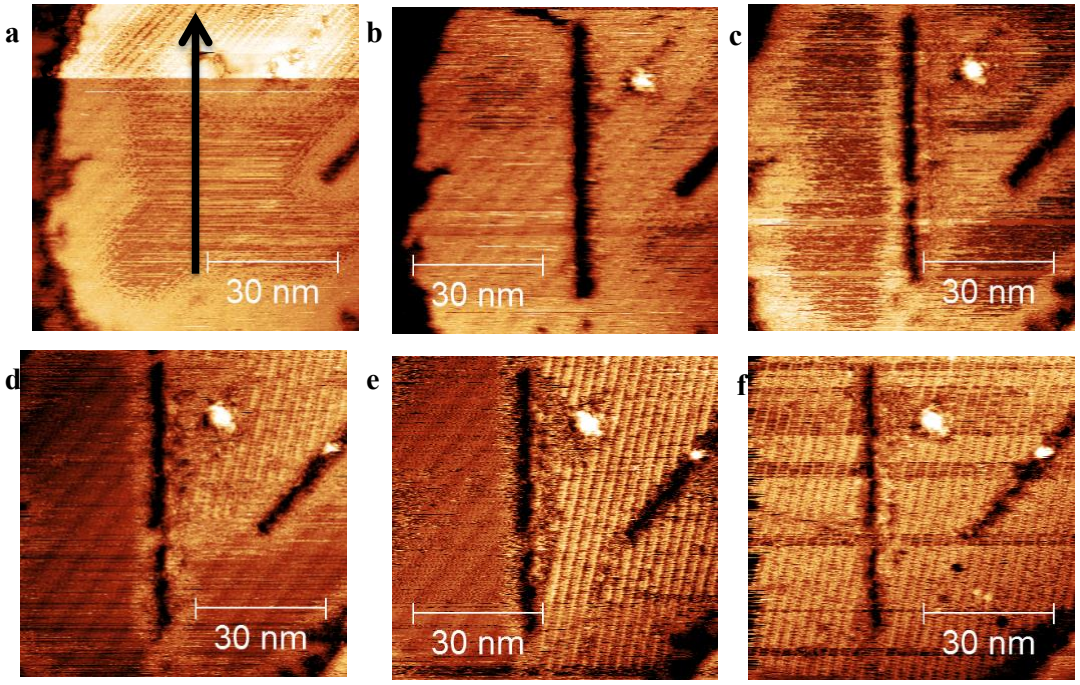

Figure 4.3: Sequence of scanning tunneling microscopy images of "columnar zig-zag" DBBA island (a) before and (b) after tip-induced manipulation. The tip was moved at 100 Å/s while being lowered 35 Å relative to its equilibrium position resulting in a 3 Å deep trench carved into the surface. All STM images acquired at -2V 10 pA. c-f, After manipulation the self-assembled molecules are disturbed exposing the clean gold surface which shows atomic resolution of the herringbone reconstruction (d-f). The molecules re-assemble with a new orientation in (d-f) highlighting the mobility of DBBA on Au(111) at room temperature.

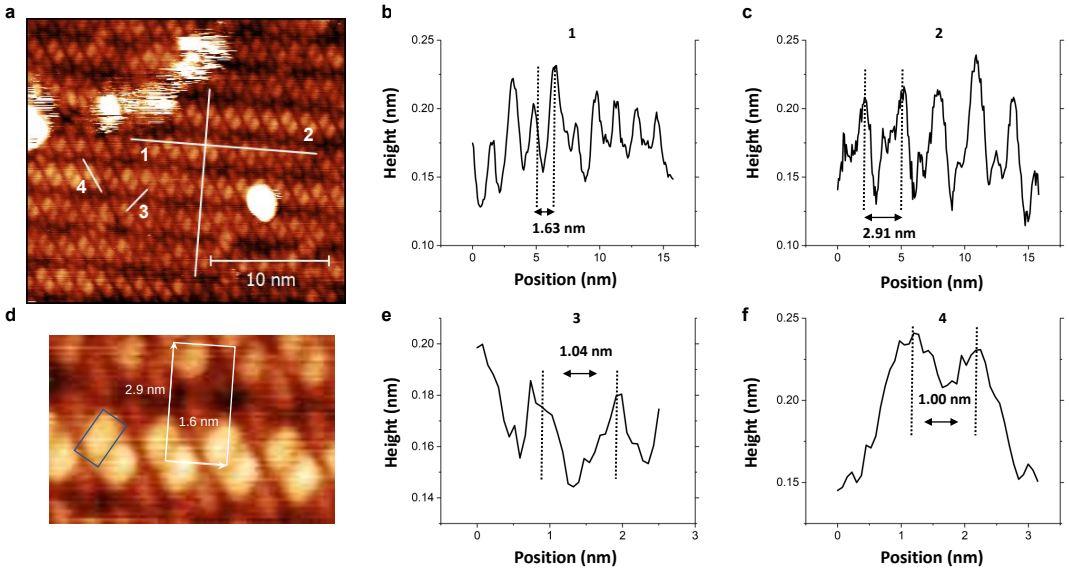

Figure 4.4: (a) STM topograph showing a close-up of the close-packed zigzag structure. sample bias: -2V tunneling current: 10 pA (b) Height profile collected along line 1 in (a) indicating a 1.63 nm intermolecular spacing along the row direction. (c) Height profile collected along line 2 in (a) showing a 2.91 nm spacing along the inter-row direction. (d) magnified view of a portion of (a) showing the closed packed zigzag unit cell (white rectangle). The blue rectangle indicates a single DBBA molecule. (e-f) Height profiles along lines 3 and 4 showing a ˜1 nm peak-to-peak distance between the adjacent DBBA molecules.

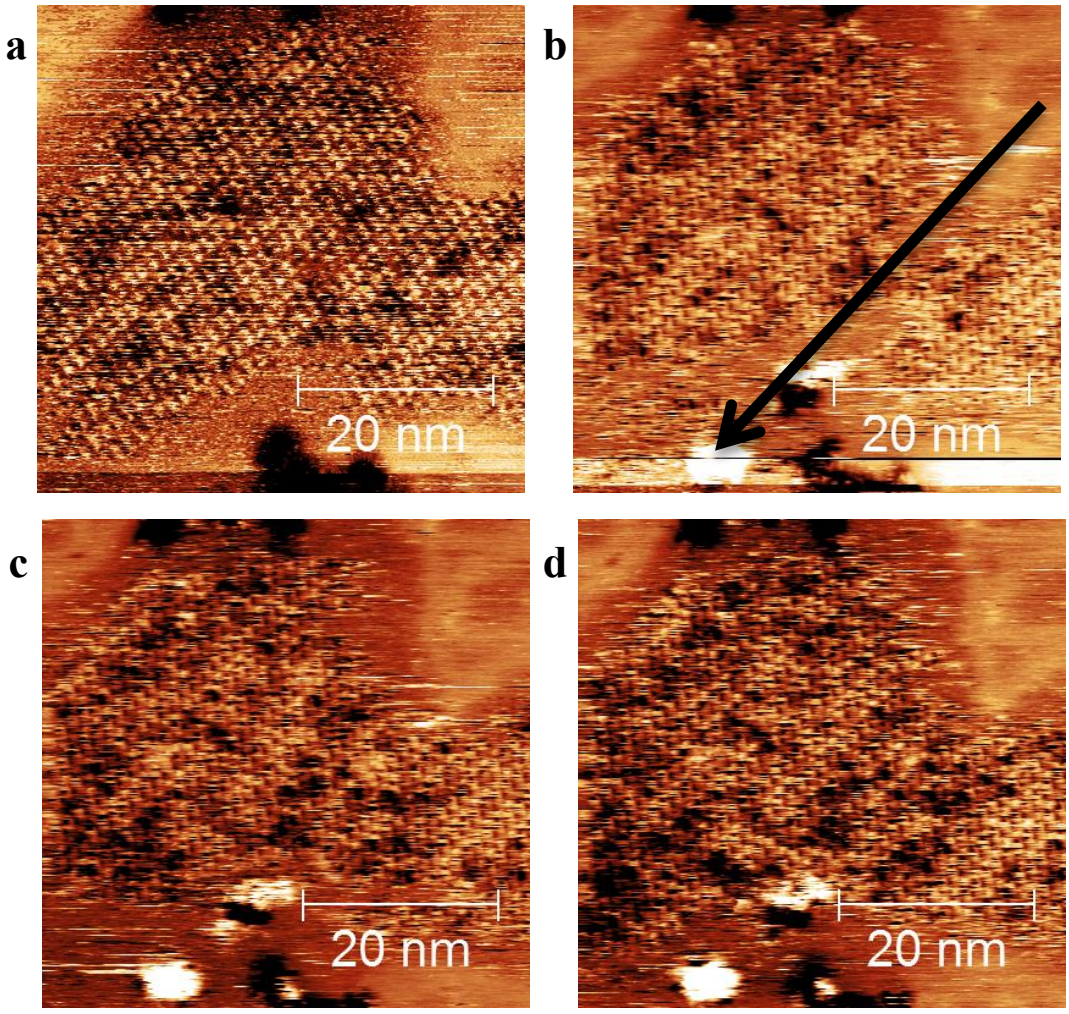

Figure 4.5: Sequence of scanning tunneling microscopy images of an "armchair" DBBA island (a) before and (b-d) after tip-induced manipulation. The tip was moved at 100 Å/s along the arrow shown in (b) while being lowered 12 Å relative to its equilibrium position. All STM images acquired at -2V 10 pA. b-d, After manipulation the self-assembled molecules are pushed away from the path of the tip. The molecules fill in the empty space, as the edges of the DBBA island continue to fluctuate.

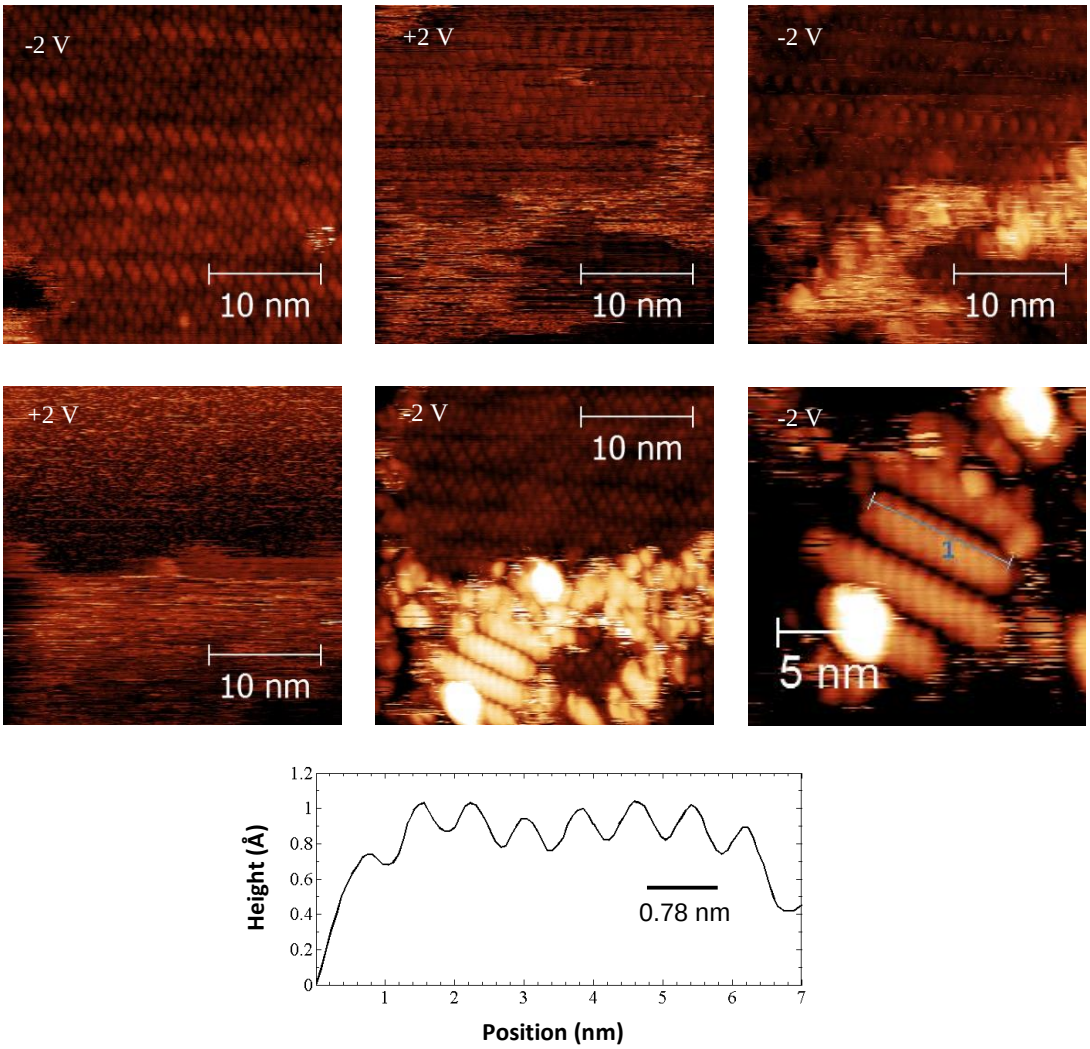

Figure 4.6: (a) Self-assembled DBBA deposited on Au(111) at room temperature and annealed at 100 °C for 20 minutes. Sample bias: -2V tunneling current 10 pA. (b-f) The same area over time, scanned at a sample bias of +2V (b, d), or -2V (c, e, f) and a tunneling current of 10 pA. Several polyanthrylene chains have formed in (e). (f) Higher resolution image of the polyanthrylene chains in (e). (h) Height cross-section along the line indicated in (f) showing a period of 0.78 nm.

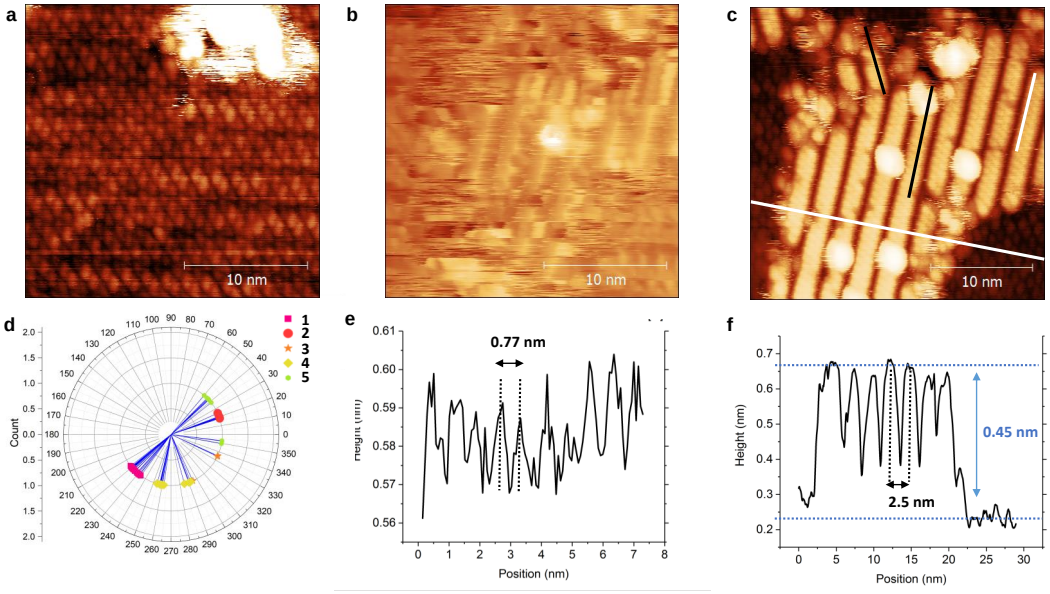

Figure 4.7: (a) STM image of an area before tip-induced manipulation. sample bias: -2 V tunneling current: 10 pA (b) Region from (a) during tip-induced manipulation. sample bias: +2 V tunneling current: 10 pA (c) Image taken over the same region at -2.0 V showing the formation of multiple chains. The black lines indicate lines used to determine the orientation of the chains relative to the arrangement of the close-packed zigzag structure. (d) Angles between close-packed zigzag row direction and the longitudinal axis of chains formed by tip-induced manipulation. The angles were determined from a series of manipulation attempts. Only the chains in the second layer are counted. (e) Height profile collected along chain formed by tip-induced manipulation, indicated by a solid white line in (c) showing a 0.77 nm period along the chain. (g) Height profile across an island of chains formed showing a 2.5 nm inter-chain spacing.

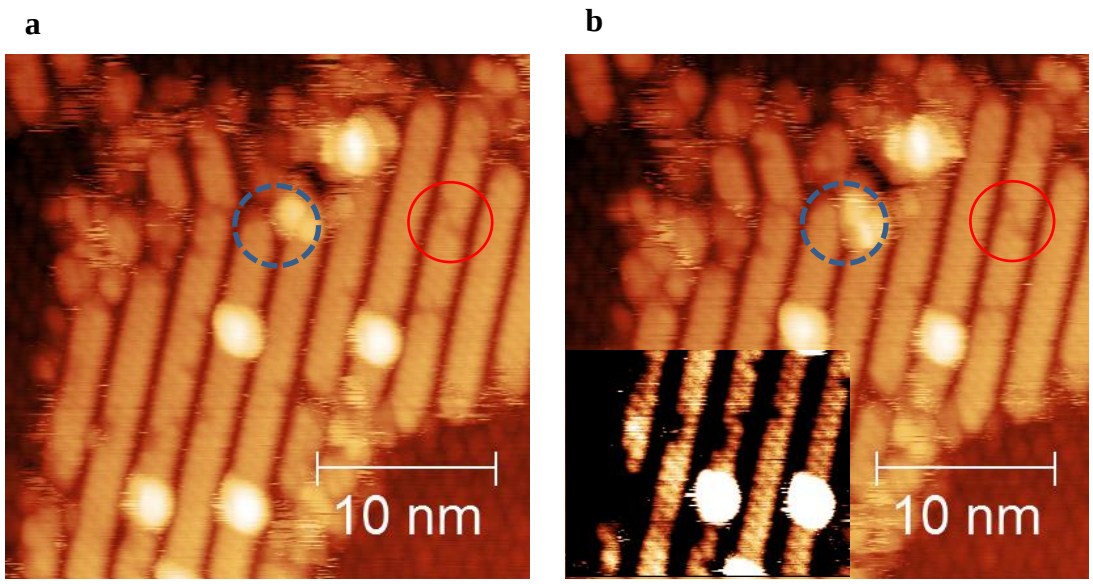

Figure 4.8: (a) STM image of polyanthrylene island formed via electron mediated assembly. Imaging at -2 V 10 pA. (b) Subsequent scan shows an increase in the length of polyanthrylene chains in the area shown by the blue circle. Two additional bumps correspond to the addition of one monomer. The red circle indicates a defect where growing chains do not fuse due to steric hindrance. The lower portion of the image is color fit to highlight the polyanthrylene structure.

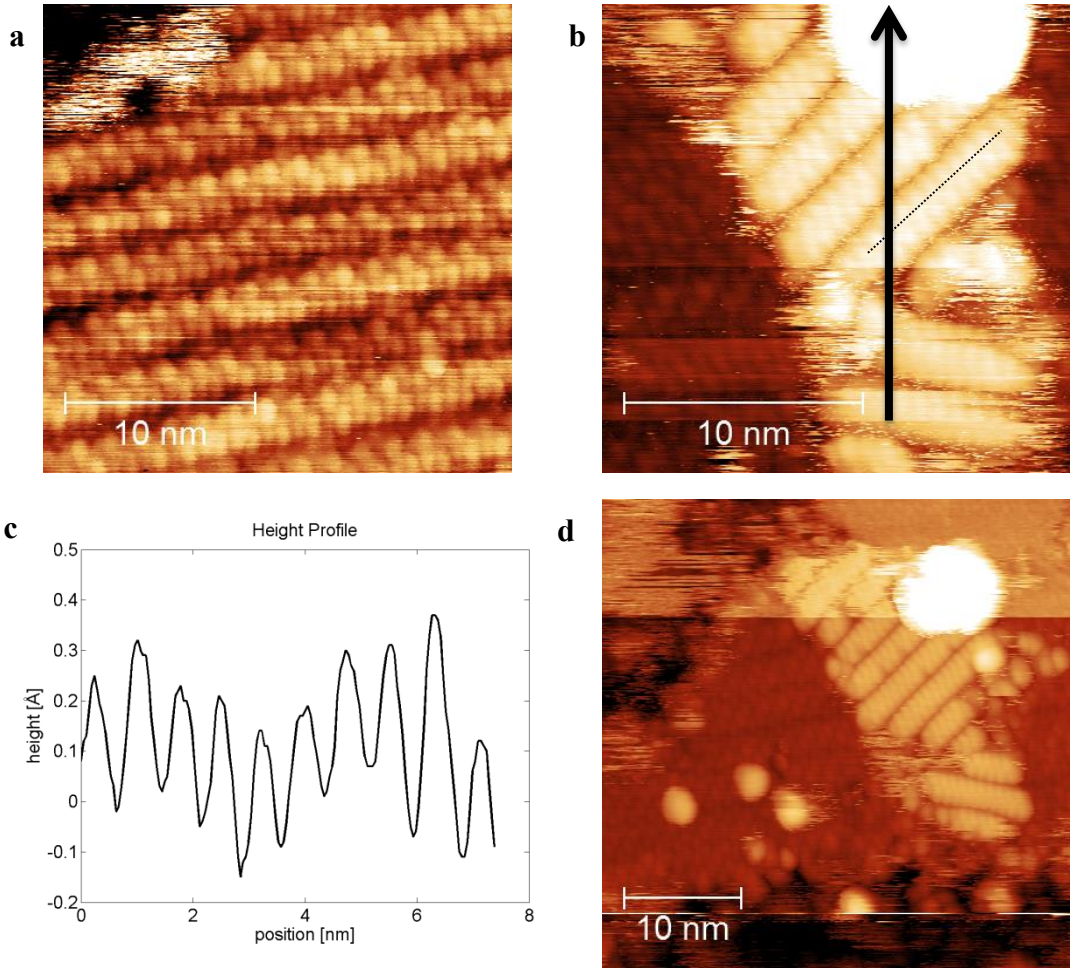

Figure 4.9: (a) Self-assembled DBBA deposited on Au(111) at room temperature and then annealed at 100 °C for 20 min. Imaged at -2 V 10 pA. (b) The tip was moved in a vertical line over the surface at +3 V, 50 pA, and a dose of 3 x 10^{-4} C/cm tracing the path indicated by the arrow in (b,d). Polyanthrylene chains formed along the path of the tip. (c) Profile along polyanthrylene chain showing a period of 0.78 nm. (d) Large scan showing that polymerization continued away from the path of the tip.

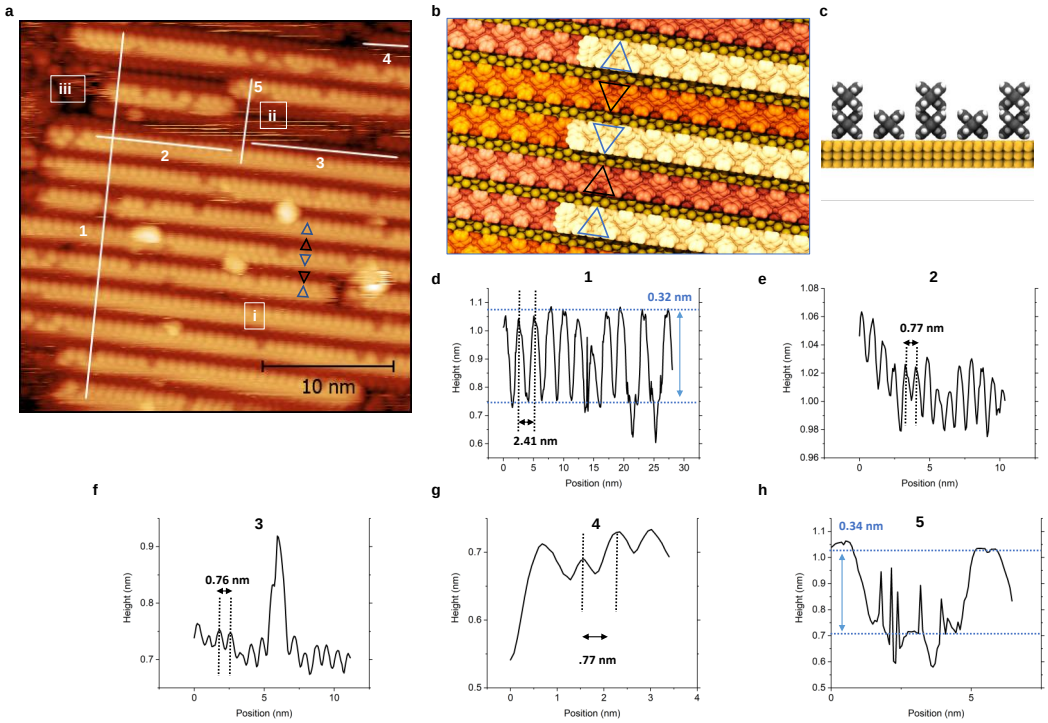

Figure 4.10: (a) Close-up of a polyanthrylene island showing a double-layer structure. Gaps visible in the upper polyanthrylene layer are caused by chirality mismatches between neighboring polyanthrylene segments. Region i shows the structure of the polyanthrylene island which consists of a lower layer with a row separation of 1.2 nm and an upper layer with a 2.4 nm row separation. Region ii near the top of the image there is a phase boundary, and the upper polyanthrylene chain changes its alignment relative to the lower layer. In region iii several monomers unattached to polyanthrylene chains are visible. Sample bias -2 V tunneling current 10 pA (b) Top down view of showing the structural model of the polyanthrylene island. The lower layer consists of parallel polyanthrylene chains separated by 1.2 nm. The rows are grouped into pairs that have the same chirality, which alternate between adjacent pairs. The upper layer consists of parallel chains with a 2.4 nm period and also alternates its chirality. (c) Side-view of the structural model indicating that the top layer of polyanthrylene sits directly on top of the row underneath. (d) Height profile measured along line 1 showing that the separation between the uppermost polyanthrylene chains is 2.41 nm, and the height difference between the top and lower PA layers is 0.32 nm. (e-g) Height profiles along lines 2-4 showing that he period of the polyanthrylene is about 0.77 nm for both the upper and lower layers. (h) Height profile over a single layer high region showing that the apparent height of the top PA layer is 0.34 nm higher than the lower PA layer.

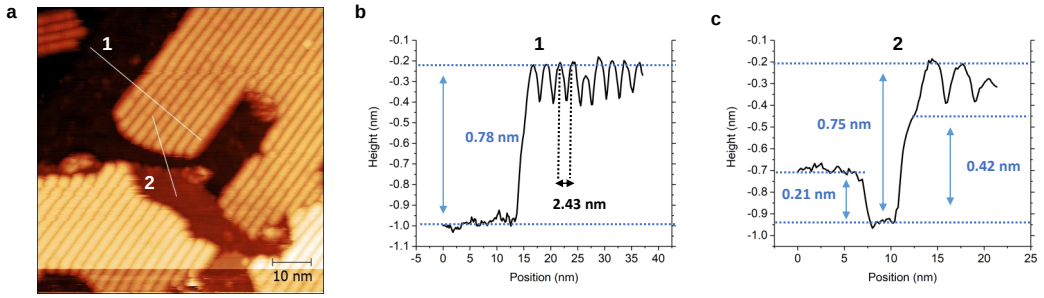

Figure 4.11: (a) STM topograph showing polyanthrylene islands surrounded by bare gold. Sample bias -2 V tunneling current 10 pA (b) Height profile taken along line 1 showing a 0.78 nm height for the polyanthrylene island and a 2.43 nm chain separation. (c) Height profile taken along line 2 showing a 0.21 nm height for the Au(111) step edge, a 0.75 nm height for the polyanthrylene island, and a 0.42 nm tall feature at the edge of the chain.

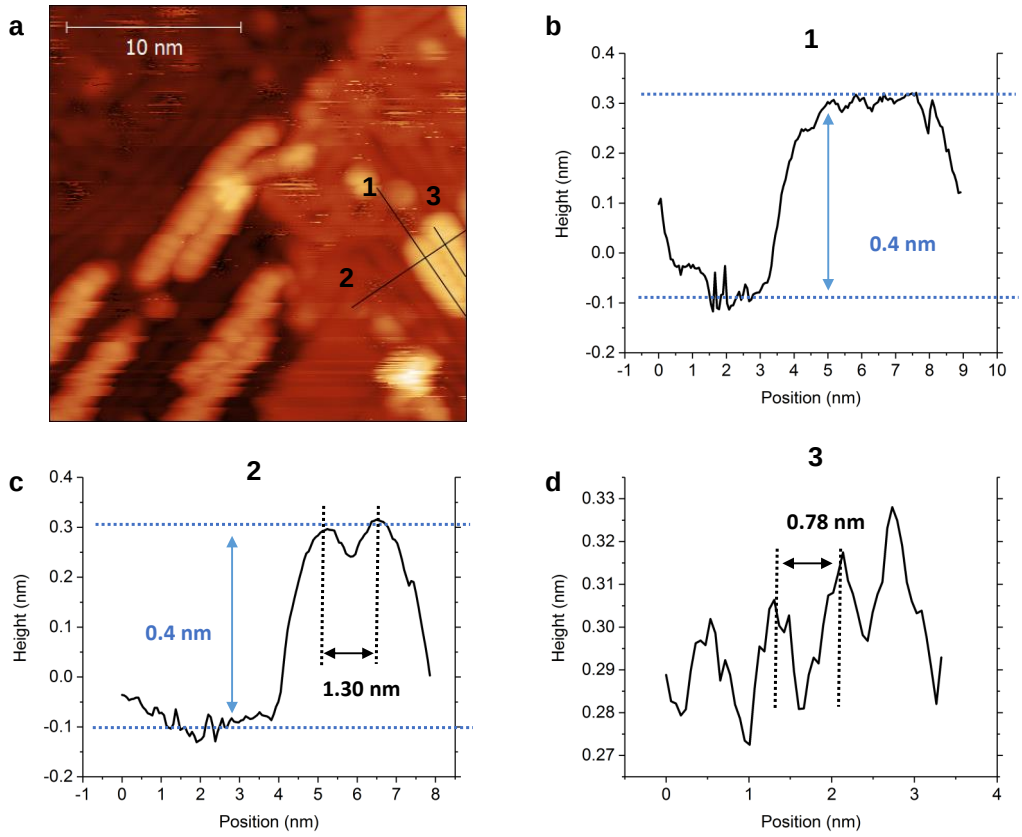

Figure 4.12: (a) STM topograph of graphene nanoribbons and polyanthrylene on Au(111) formed by annealing the armchair structure shown in Figure 4.2b. sample bias: -2 V tunneling current: 10 pA (b) Height profile taken along the line indicated by 1 showing a 0.4 nm height of the polyanthrylene chain relative to the graphene nanoribbons, indicating it is a layer above the graphene nanoribbons underneath.(c) Height profile taken along line 2 in (a) indicating a 1.3 nm distance between the two neighboring polyanthrylene chains. (d) 0.78 nm period measured along the length of the polyanthrylene chain.

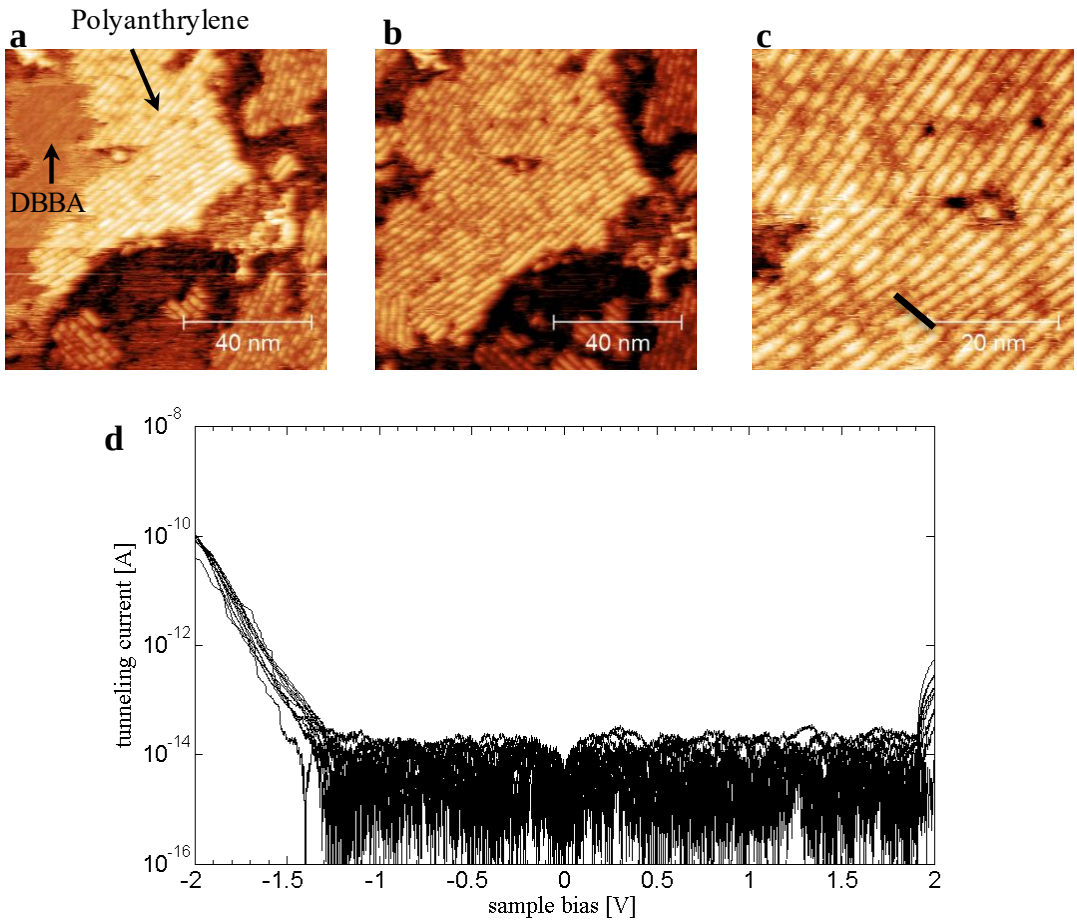

Figure 4.13: Scanning tunneling microscopy images illustrating tip-induced polymerization of 10,10'-dibromo-9,9'-bianthracene on Au(111). (a) Self-assembled DBBA deposited at room temperature and annealed at 80 °C for 20 minutes. Sample bias: -2 V tunneling current 10 pA. A polyanthrylene island forms next to non-covalently bonded DBBA molecules. (b) The polyanthrylene island grows away from the step edge, covering the area previously occupied by the DBBA molecules. (c) close-up indicating the region used for collecting scanning tunneling spectroscopy data (d) Constant spacing scanning tunneling spectra showing a bandgap of 3.25 eV.

4.9 References

[1] Nasiba Abdurakhmanova, Nadja Amsharov, Sebastian Stepanow, Martin Jansen, Klaus Kern, and Konstantin Amsharov. Synthesis of wide atomically precise graphene nanoribbons from para-oligophenylene based molecular precursor. *Carbon*, 77:1187–1190, 2014.

[2] Richard Balog, Bjarke Jorgensen, Louis Nilsson, Mie Andersen, Emile Rienks, Marco Bianchi, Mattia Fanetti, Erik Laegsgaard, Alessandro Baraldi, Silvano Lizzit, Zeljko Sljivancanin, Flemming Besenbacher, Bjork Hammer, Thomas G. Pedersen, Philip Hofmann, and Liv Hornekaer. Bandgap opening in graphene induced by patterned hydrogen adsorption. *Nat Mater*, 9(4):315–319, 2010.

[3] Andrea Basagni, Francesco Sedona, Carlo A. Pignedoli, Mattia Cattelan, Louis Nicolas, Maurizio Casarin, and Mauro Sambi. Molecules–oligomers–nanowires–graphene nanoribbons: A bottom-up stepwise on-surface covalent synthesis preserving long-range order. *Journal of the American Chemical Society*, 137(5):1802–1808, 2015.

[4] Arunabh Batra, Dean Cvetko, Gregor Kladnik, Olgun Adak, Claudia Cardoso, Andrea Ferretti, Deborah Prezzi, Elisa Molinari, Alberto Morgante, and Latha Venkataraman. Probing the mechanism for graphene nanoribbon formation on gold surfaces through x-ray spectroscopy. *Chem. Sci.*, 5(11):4419–4423, 2014.

[5] M. Bieri, M. Treier, J. Cai, K. Ait-Mansour, P. Ruffieux, O. Groning, P. Groning, M. Kastler, R. Rieger, X. Feng, K. Mullen, and R. Fasel. Porous graphenes: two-dimensional polymer synthesis with atomic precision. *Chem Commun (Camb)*, (45):6919–21, 2009.

[6] J. Bjork, F. Hanke, and S. Stafstrom. Mechanisms of halogen-based covalent self-assembly on metal surfaces. *J Am Chem Soc*, 135(15):5768–75, 2013.

[7] J. Bjork, F. Hanke, and S. Stafstrom. Mechanisms of halogen-based covalent self-assembly on metal surfaces. *J Am Chem Soc*, 135(15):5768–75, 2013.

[8] Stephan Blankenburg, Jinming Cai, Pascal Ruffieux, Rached Jaafar, Daniele Passerone, Xinliang Feng, Klaus Müllen, Roman Fasel, and Carlo A. Pignedoli. Intraribbon heterojunction formation in ultranarrow graphene nanoribbons. *ACS Nano*, 6(3):2020–2025, 2012.

[9] C. Bronner, M. Utecht, A. Haase, P. Saalfrank, T. Klamroth, and P. Tegeder. Electronic structure changes during the surface-assisted formation of a graphene nanoribbon. *J Chem Phys*, 140(2):024701, 2014.

[10] Christopher Bronner. *Photoinduced and Thermal Reactions of Functional Molecules at Surfaces*. Thesis, 2014.

[11] Christopher Bronner, Jonas Björk, and Petra Tegeder. Tracking and removing br during the on-surface synthesis of a graphene nanoribbon. *The Journal of Physical Chemistry C*, 119(1):486–493, 2015.

[12] Christopher Bronner, Jonas Björk, and Petra Tegeder. Tracking and removing br during the on-surface synthesis of a graphene nanoribbon. *The Journal of Physical Chemistry C*, 119(1):486–493, 2015.

[13] J. Cai, P. Ruffieux, R. Jaafar, M. Bieri, T. Braun, S. Blankenburg, M. Muoth, A. P. Seitsonen, M. Saleh, X. Feng, K. Mullen, and R. Fasel. Atomically precise bottom-up fabrication of graphene nanoribbons. *Nature*, 466(7305):470–3, 2010.

[14] J. Cai, P. Ruffieux, R. Jaafar, M. Bieri, T. Braun, S. Blankenburg, M. Muoth, A. P. Seitsonen, M. Saleh, X. Feng, K. Mullen, and R. Fasel. Atomically precise bottom-up fabrication of graphene nanoribbons. *Nature*, 466(7305):470–3, 2010.

[15] Tom Carpy. *A scanning tunnelling microscopy and spectroscopic study of bromine functionalised molecules on metal surfaces.* Thesis, 2015.

[16] Min Chen, Jie Xiao, Hans-Peter Steinrück, Shiyong Wang, Weihua Wang, Nian Lin, Wolfgang Hieringer, and J. Michael Gottfried. Combined photoemission and scanning tunneling microscopy study of the surface-assisted ullmann coupling reaction. *The Journal of Physical Chemistry C*, 118(13):6820–6830, 2014.

[17] Yen-Chia Chen, Ting Cao, Chen Chen, Zahra Pedramrazi, Danny Haberer, G. de OteyzaDimas, Felix R. Fischer, Steven G. Louie, and Michael F. Crommie. Molecular bandgap engineering of bottom-up synthesized graphene nanoribbon heterojunctions. *Nat Nano*, 10(2):156–160, 2015.

[18] R. Denk, M. Hohage, P. Zeppenfeld, J. Cai, C. A. Pignedoli, H. Sode, R. Fasel, X. Feng, K. Mullen, S. Wang, D. Prezzi, A. Ferretti, A. Ruini, E. Molinari, and P. Ruffieux. Exciton-dominated optical response of ultranarrow graphene nanoribbons. *Nat Commun*, 5:4253, 2014.

[19] Q. Fan, C. Wang, Y. Han, J. Zhu, W. Hieringer, J. Kuttner, G. Hilt, and J. M. Gottfried. Surface-assisted organic synthesis of hyperbenzene nanotroughs. *Angew Chem Int Ed Engl*, 52(17):4668–72, 2013.

[20] Patrick Han, Kazuto Akagi, Filippo Federici Canova, Hirotaka Mutoh, Susumu Shiraki, Katsuya Iwaya, Paul S Weiss, Naoki Asao, and Taro Hitosugi. Bottom-up graphene-nanoribbon fabrication reveals chiral edges and enantioselectivity. *ACS nano*, 2014.

[21] Saw-Wai Hla, Ludwig Bartels, Gerhard Meyer, and Karl-Heinz Rieder. Inducing all steps of a chemical reaction with the scanning tunneling microscope tip: towards single molecule engineering. *Physical review letters*, 85(13):2777, 2000.

[22] Md Zakir Hossain, James E. Johns, Kirk H. Bevan, Hunter J. Karmel, Yu Teng Liang, Shinya Yoshimoto, Kozo Mukai, Tatanori Koitaya, Jun Yoshinobu, Maki Kawai, Amanda M. Lear, Larry L. Kesmodel, Steven L. Tait, and Mark C. Hersam. Chemically homogeneous and thermally reversible oxidation of epitaxial graphene. *Nat Chem*, 4(4):305–309, 2012.

[23] William Humphrey, Andrew Dalke, and Klaus Schulten. VMD – Visual Molecular Dynamics. *Journal of Molecular Graphics*, 14:33–38, 1996.

[24] Keun Soo Kim, Yue Zhao, Houk Jang, Sang Yoon Lee, Jong Min Kim, Kwang S. Kim, Jong-Hyun Ahn, Philip Kim, Jae-Young Choi, and Byung Hee Hong. Large-scale pattern growth of graphene films for stretchable transparent electrodes. *Nature*, 457(7230):706–710, 2009.

[25] M. Koch, F. Ample, C. Joachim, and L. Grill. Voltage-dependent conductance of a single graphene nanoribbon. *Nat Nanotechnol*, 7(11):713–7, 2012.

[26] Xiaolin Li, Xinran Wang, Li Zhang, Sangwon Lee, and Hongjie Dai. Chemically derived, ultrasmooth graphene nanoribbon semiconductors. *Science*, 319(5867):1229–1232, 2008.

[27] Chuanxu Ma, Zhongcan Xiao, Honghai Zhang, Liangbo Liang, Jingsong Huang, Wenchang Lu, Bobby G Sumpter, Kunlun Hong, J Bernholc, and An-Ping Li. Controllable conversion of quasi-freestanding polymer chains to graphene nanoribbons. *Nature Communications*, 8:14815, 2017.

[28] D. G. Matei, N. E. Weber, S. Kurasch, S. Wundrack, M. Woszczyna, M. Grothe, T. Weimann, F. Ahlers, R. Stosch, U. Kaiser, and A. Turchanin. Functional single-layer graphene sheets from aromatic monolayers. *Adv Mater*, 25(30):4146–51, 2013.

[29] K. A. Ritter and J. W. Lyding. The influence of edge structure on the electronic properties of graphene quantum dots and nanoribbons. *Nat Mater*, 8(3):235–42, 2009.

[30] Jeremy T. Robinson, James S. Burgess, Chad E. Junkermeier, Stefan C. Badescu, Thomas L. Reinecke, F. Keith Perkins, Maxim K. Zalalutdniov, Jeffrey W. Baldwin, James C. Culbertson, Paul E. Sheehan, and Eric S. Snow. Properties of fluorinated graphene films. *Nano Letters*, 10(8):3001–3005, 2010.

[31] Y. Shen, G. Tian, H. Huang, Y. He, Q. Xie, F. Song, Y. Lu, P. Wang, and Y. Gao. Chiral self-assembly of nonplanar 10,10'-dibromo-9,9'-bianthryl molecules on ag(111). *Langmuir*, 33(12):2993–2999, 2017.

[32] Konstantin Simonov. *Effect of Substrate on Bottom-Up Fabrication and Electronic Properties of Graphene Nanoribbons.* Thesis, 2016.

[33] Konstantin A. Simonov, Nikolay A. Vinogradov, Alexander S. Vinogradov, Alexander V. Generalov, Elena M. Zagrebina, Nils Martensson, Attilio A. Cafolla, Tomas Carpy, John P. Cunniffe, and Alexei B. Preobrajenski. Effect of substrate chemistry on the bottom-up fabrication of graphene nanoribbons: Combined core-level spectroscopy and stm study. *The Journal of Physical Chemistry C*, 118(23):12532–12540, 2014.

[34] BC Stipe, MA Rezaei, W Ho, S Gao, M Persson, and BI Lundqvist. Single-molecule dissociation by tunneling electrons. *Physical review letters*, 78(23):4410, 1997.

[35] John Stone. *An Efficient Library for Parallel Ray Tracing and Animation.* Master's thesis, Computer Science Department, University of Missouri-Rolla, April 1998.

[36] L. Talirz, H. Sode, J. Cai, P. Ruffieux, S. Blankenburg, R. Jafaar, R. Berger, X. Feng, K. Mullen, D. Passerone, R. Fasel, and C. A. Pignedoli. Termini of bottom-up fabricated graphene nanoribbons. *J Am Chem Soc*, 135(6):2060–3, 2013.

[37] J. van der Lit, M. P. Boneschanscher, D. Vanmaekelbergh, M. Ijas, A. Uppstu, M. Ervasti, A. Harju, P. Liljeroth, and I. Swart. Suppression of electron-vibron coupling in graphene nanoribbons contacted via a single atom. *Nat Commun*, 4:2023, 2013.

[38] Xinran Wang, Yijian Ouyang, Xiaolin Li, Hailiang Wang, Jing Guo, and Hongjie Dai. Room-temperature all-semiconducting sub-10-nm graphene nanoribbon field-effect transistors. *Physical review letters*, 100(20):206803, 2008.

[39] Y. Zhang, T. T. Tang, C. Girit, Z. Hao, M. C. Martin, A. Zettl, M. F. Crommie, Y. R. Shen, and F. Wang. Direct observation of a widely tunable bandgap in bilayer graphene. *Nature*, 459(7248):820–3, 2009.

CHAPTER 5

SUMMARY AND FUTURE WORK

5.1 Summary

Chapter 1 motivates the study of atomically precise graphene nanoribbons. Due to their high mobility and high thermal conductivity, graphene nanoribbons may prove to be a suitable material for next-generation transistors. A literature review summarizes the progress in understanding and controlling the synthesis of GNRs, highlighting the importance of atomic precision. The significant challenges that arise – cleanly placing GNRs onto device-relevant substrates, a lack of detailed electronic characterization due to the interference of metal surface states, and the need to control the orientation and positions of GNRs were explored in this thesis.

Chapter 2 established that the dry contact transfer method is suitable for characterization of solution-synthesized atomically precise graphene nanoribbons. By cleanly placing chevron graphene nanoribbons (GNRs) onto H:Si(100), detailed electronic characterization was achieved allowing for the determination of a 2.8 eV bandgap,[21] approaching expected theoretical values.[3, 27] Due to the atomically thin nature of graphene nanoribbons, the substrate could be imaged underneath the GNRs due to a semitransparency effect.[11] Tunneling to the substrate had a significant influence on STS measurements and comparisons between CITS data and first principles computational modeling were instrumental in distinguishing the electronic states of the GNR from those of the H:Si(100) substrate. The bandgap of cGNRs on H:Si(100)[21] is larger than the bandgap of cGNRs on Au(111)[26] indicating a reduced substrate screening effect. When a cGNR was placed in direct contact with Si(100) via hydrogen depassivation lithography, metallic be-

havior was observed. Alongside changes in the apparent height and width of the GNR in the STM topographs, the modified electronic structure of the cGNR provides strong evidence of silicon-carbon bond formation. GNR junctions formed by overlapping graphene nanoribbons did not show any significant changes in their bandgaps.

STM and STS of two additional GNR geometries, the extended chevron GNR (eGNR) and the hybrid GNR (hGNR) elucidated how structural modification alters the bandgap of GNRs. The increased lateral extension of the eGNR decreased the bandgap by ˜0.1 eV. When the chevron graphene nanoribbon geometry was modified by closing the inner elbows to form pores, there was a very significant decrease in the bandgap on the order of 1 eV. Further work is needed to fully characterize the spatial distribution of the observed electronic states. Overall DCT of GNRs offers a highly useful approach towards characterizing solution-synthesized graphene nanoribbons and obtaining STS measurements free from the influence of metallic surface states.

Chapter 4 outlined experiments investigating positional control over graphene nanoribbon synthesis via tip-induced polymerization of DBBA. The STM experiments suggest that DBBA molecules self-assemble into different conformations depending on the sample history. Both temperature and surface coverage are expected to influence the arrangement of the molecules. Structural models were proposed for the observed molecular arrangements and the close-packed zigzag structure was found to polymerize into polyanthrylene islands at a positive sample bias. The mechanism is believed to be tip-induced de-bromination which is followed by exothermic aryl coupling.[2] The energy released during polymerization may dissipate to the substrate as well as via the rearrangement of the underlying molecules into polyanthrylene islands which requires rotation and small displacements of the molecules which have activation barriers on the orders of tenths of an eV.[2] While the close-packed zigzag islands and the polyanthrylene islands have similar surface densities of ˜0.8 monomers per nm^2, the polyanthrylene islands do not align with respect to the arrangement of the intact molecules. There resulting

polyanthrylene chains do align parallel to each other, at orientations in intervals of 30 ° indicating registration to the underlying Au(111) lattice.

5.2 Future Work

The fabrication and characterization of a well-controlled single-GNR transistor is a significant remaining challenge. A systematic approach may focus on identifying a suitable substrate, evaluating GNR contacts, and optimizing the GNR structure. For substrate optimization, the work function and bandgap of the substrate are the key parameters to consider. Ideally, the bandgap of the substrate is larger than the bandgap of the GNR to minimize leakage current during transistor operation. Silicon nitride, silicon carbide, Ti(100),[16] or boron nitride[14, 15] may be suitable options. For CNTs, the work function of the substrate can lead to charge transfer that alters the doping level,[22] and similar behavior has yet to be investigated for GNRs. Studying intrinsic and nitrogen containing chevron GNRs on n-type and p-type Si(100) at a variety of substrate dopant concentrations could provide substantial experimental progress towards substrate optimization.

Demonstrating ohmic contacts to graphene nanoribbons is another interesting problem. The contact material can change whether graphene is n-type or p-type via work function doping,[8] and provides a way of overcoming stringent dopant density distribution requirements for atomic-scale devices. Graphene contacts may also be used to make GNR transistors.[5] A detailed investigation of GNR-graphene interfaces via STS under UHV would determine whether an ohmic contact is formed. CNT-GNR interfaces may also be worth investigating. One route towards forming such interfaces is edge-dehydrogenation of graphene nanoribbons at elevated temperatures. A similar approach was used to fuse porphyrin molecules to graphene on Ag(111).[12] In-situ transistor fabrication via STM nanolithography, analogous to the UHV-STM fabrication of a single atom transistor[7, 18, 19, 23] could be pursued to make GNR devices and assess their feasibility for commercial applications.

GNR transistor fabrication is greatly inhibited by a lack of control over alignment and positioning. For large-scale commercial applications, global alignment is highly desirable. One potential avenue for achieving large area alignment is the direct-growth of GNRs onto a silicon or germanium substrate. It should be noted that when using methane as a precursor, aligned GNRs can be grown on Ge(111), although without atomic precision or control over GNR width.[13] Aligned polymerization on Si(100) has been well-documented for polystyrene on Si(100),[1, 28] and there may be a molecule that can both align to the Si(100) surface and form graphene nanoribbons. Identifying a suitable GNR precursor for growth on silicon is challenging because silicon-carbon bond formation is favorable for many organic molecules in contact with Si(100).[6, 9, 10, 20, 24, 25]

Presently cove-type GNRs appear to promise the highest mobilities while maintaining significant bandgaps[4, 17] however other types of GNRs can be fine-tuned for specific applications. Continuing to characterize the growing number of solution-synthesized graphene nanoribbons can aid in the quest for optimizing the geometry and chemical modification of GNRs for transistor formation.

5.3 References

[1] R. Basu, C. R. Kinser, J. D. Tovar, and M. C. Hersam. Bromine functionalized molecular adlayers on hydrogen passivated silicon surfaces. *Chemical Physics*, 326(1):144–150, 2006.

[2] J. Bjork, F. Hanke, and S. Stafstrom. Mechanisms of halogen-based covalent self-assembly on metal surfaces. *J Am Chem Soc*, 135(15):5768–75, 2013.

[3] Christopher Bronner, Anton Haase, and Petra Tegeder. Image potential states at chevron-shaped graphene nanoribbons /au(111) interfaces. *Physical Review B*, 91(4), 2015.

[4] Liping Chen, Linjun Wang, and David Beljonne. Designing coved graphene nanoribbons with charge carrier mobility approaching that of graphene. *Carbon*, 77:868–879, 2014.

[5] Zongping Chen, Wen Zhang, Carlos-Andres Palma, Alberto Lodi Rizzini, Bilu Liu, Ahmad Abbas, Nils Richter, Leonardo Martini, Xiao-Ye Wang,

Nicola Cavani, Hao Lu, Neeraj Mishra, Camilla Coletti, Reinhard Berger, Florian Klappenberger, Mathias Kläui, Andrea Candini, Marco Affronte, Chongwu Zhou, Valentina De Renzi, Umberto del Pennino, Johannes V. Barth, Hans Joachim Räder, Akimitsu Narita, Xinliang Feng, and Klaus Müllen. Synthesis of graphene nanoribbons by ambient-pressure chemical vapor deposition and device integration. *Journal of the American Chemical Society*, 138(47):15488–15496, 2016.

[6] Michael A. Filler and Stacey F. Bent. The surface as molecular reagent: organic chemistry at the semiconductor interface. *Progress in Surface Science*, 73(1-3):1–56, 2003.

[7] Martin Fuechsle, Jill A. Miwa, Suddhasatta Mahapatra, Hoon Ryu, Sunhee Lee, Oliver Warschkow, Lloyd C. L. Hollenberg, Gerhard Klimeck, and Michelle Y. Simmons. A single-atom transistor. *Nat Nano*, 7(4):242–246, 2012.

[8] G. Giovannetti, P. A. Khomyakov, G. Brocks, V. M. Karpan, J. van den Brink, and P. J. Kelly. Doping graphene with metal contacts. *Physical Review Letters*, 101(2):026803, 2008.

[9] K. R. Harikumar, T. Lim, I. R. McNab, J. C. Polanyi, L. Zotti, S. Ayissi, and W. A. Hofer. Dipole-directed assembly of lines of 1,5-dichloropentane on silicon substrates by displacement of surface charge. *Nat Nanotechnol*, 3(4):222–8, 2008.

[10] K. R. Harikumar, I. R. McNab, J. C. Polanyi, A. Zabet-Khosousi, C. Panosetti, and W. A. Hofer. Stereo-isomerism controls surface reactivity: 1-chloropentane-pairs on si(100)-2x1. *Chem Commun (Camb)*, 47(44):12101–3, 2011.

[11] Kevin T. He, Justin C. Koepke, Salvador Barraza-Lopez, and Joseph W. Lyding. Separation-dependent electronic transparency of monolayer graphene membranes on iiiv semiconductor substrates. *Nano Lett*, 10(9):3446–3452, 2010.

[12] Yuanqin He, Manuela Garnica, Felix Bischoff, Jacob Ducke, Marie-Laure Bocquet, Matthias Batzill, Willi Auwärter, and Johannes V. Barth. Fusing tetrapyrroles to graphene edges by surface-assisted covalent coupling. *Nat Chem*, 9(1):33–38, 2017.

[13] R. M. Jacobberger, B. Kiraly, M. Fortin-Deschenes, P. L. Levesque, K. M. McElhinny, G. J. Brady, R. Rojas Delgado, S. Singha Roy, A. Mannix, M. G. Lagally, P. G. Evans, P. Desjardins, R. Martel, M. C. Hersam, N. P. Guisinger, and M. S. Arnold. Direct oriented growth of armchair graphene nanoribbons on germanium. *Nat Commun*, 6:8006, 2015.

[14] P. Jarvinen, S. K. Hamalainen, K. Banerjee, P. Hakkinen, M. Ijas, A. Harju, and P. Liljeroth. Molecular self-assembly on graphene on sio2 and h-bn substrates. *Nano Lett*, 13(7):3199–204, 2013.

[15] S. Joshi, D. Ecija, R. Koitz, M. Iannuzzi, A. P. Seitsonen, J. Hutter, H. Sachdev, S. Vijayaraghavan, F. Bischoff, K. Seufert, J. V. Barth, and W. Auwarter. Boron nitride on cu(111): an electronically corrugated monolayer. *Nano Lett*, 12(11):5821–8, 2012.

[16] Marek Kolmer, Amir A Ahmad Zebari, Jakub S PrauznerBechcicki, Witold Piskorz, Filip Zasada, Szymon Godlewski, Bartosz Such, Zbigniew Sojka, and Marek Szymonski. Polymerization of polyanthrylene on a titanium dioxide (011)(2 1) surface. *Angewandte Chemie International Edition*, 52(39):10300–10303, 2013.

[17] Junzhi Liu, Bo-Wei Li, Yuan-Zhi Tan, Angelos Giannakopoulos, Carlos Sanchez-Sanchez, David Beljonne, Pascal Ruffieux, Roman Fasel, Xinliang Feng, and Klaus Müllen. Toward cove-edged low band gap graphene nanoribbons. *Journal of the American Chemical Society*, 137(18):6097–6103, 2015.

[18] S. Mahapatra, H. Buch, and M. Y. Simmons. Charge sensing of precisely positioned p donors in si. *Nano Lett*, 11(10):4376–81, 2011.

[19] S. R. McKibbin, G. Scappucci, W. Pok, and M. Y. Simmons. Epitaxial top-gated atomic-scale silicon wire in a three-dimensional architecture. *Nanotechnology*, 24(4):045303, 2013.

[20] Fedor Y. Naumkin, John C. Polanyi, Duncan Rogers, Werner Hofer, and Andrew Fisher. Electron-induced attachment of chlorinated benzenes to si(100)21. *Surface Science*, 547(3):324–334, 2003.

[21] A. Radocea, T. Sun, T. H. Vo, A. Sinitskii, N. R. Aluru, and J. W. Lyding. Solution-synthesized chevron graphene nanoribbons exfoliated onto h:si(100). *Nano Lett*, 17(1):170–178, 2017.

[22] Laura B. Ruppalt and Joseph W. Lyding. Charge transfer between semiconducting carbon nanotubes and their doped gaas(110) and inas(110) substrates detected by scanning tunnelling spectroscopy. *Nanotechnology*, 18(21):215202, 2007.

[23] G. Scappucci, G. Capellini, B. Johnston, W. M. Klesse, J. A. Miwa, and M. Y. Simmons. A complete fabrication route for atomic-scale, donor-based devices in single-crystal germanium. *Nano Lett*, 11(6):2272–9, 2011.

[24] P. A. Sloan and R. E. Palmer. Manipulation of polyatomic molecules with the scanning tunnelling microscope at room temperature: chlorobenzene adsorption and desorption from si(111)-(7 7). *Journal of Physics: Condensed Matter*, 18(33):S1873–S1885, 2006.

[25] P. A. Sloan, S. Sakulsermsuk, and R. E. Palmer. Nonlocal desorption of chlorobenzene molecules from the si(111)-(7x7) surface by charge injection from the tip of a scanning tunneling microscope: remote control of atomic manipulation. *Phys Rev Lett*, 105(4):048301, 2010.

[26] Timothy H. Vo, U. Gayani E. Perera, Mikhail Shekhirev, Mohammad Mehdi Pour, Donna A. Kunkel, Haidong Lu, Alexei Gruverman, Eli Sutter, Mircea Cotlet, Dmytro Nykypanchuk, Percy Zahl, Axel Enders, Alexander Sinitskii, and Peter Sutter. Nitrogen-doping induced self-assembly of graphene nanoribbon-based two-dimensional and three-dimensional metamaterials. *Nano Letters*, 15(9):5770–5777, 2015.

[27] Shudong Wang and Jinlan Wang. Quasiparticle energies and optical excitations in chevron-type graphene nanoribbon. *The Journal of Physical Chemistry C*, 116(18):10193–10197, 2012.

[28] J. Zikovsky, S. A. Dogel, M. H. Salomons, J. L. Pitters, G. A. DiLabio, and R. A. Wolkow. Indications of field-directing and self-templating effects on the formation of organic lines on silicon. *J Chem Phys*, 134(11):114707, 2011.